1248.

INVESTIGATION OF THE OPTICAL CHARACTERISTICS OF THE CONE-AND-COLUMN DOUBLE REFLECTOR SOLAR CONCENTRATOR

FINAL REPORT

NOVEMBER 1963

[2]

(NASA Contract NAS[illegible]1-3140)

National Aeronautics and Space Administration
Langley Research Center
Langley Station, Hampton, Virginia

GOODYEAR AEROSPACE
CORPORATION
Akron, Ohio

CODE IDENT NO. 25500

GOODYEAR AEROSPACE

CORPORATION

AKRON 15 OHIO

INVESTIGATION OF THE OPTICAL CHARACTERISTICS OF THE CONE-AND-COLUMN DOUBLE REFLECTOR SOLAR CONCENTRATOR

GER 11292 Contract NAS 1-3140

By J. W. Haylett

Final Report

November 1963

National Aeronautics and Space Administration
Langley Research Center
Langley Station, Hampton, Virginia

ABSTRACT

14904

The feasibility of using the Cone-and-Column, double-reflector, solar concentrator for space applications is documented in this final report of the work performed under Contract NAS 1-3140. Testing of the cone, concentrator testing, and a computer analysis of the system optics are described. The optical study and model construction were performed under a program for Langley Research Center, National Aeronautics and Space Administration by Goodyear Aerospace Corporation.

Author

TABLE OF CONTENTS

LIST OF ILLUSTRATIONS

LIST OF TABLES

SECTION I. INTRODUCTION

A. GENERAL

Under Contract NAS-1-3140 for NASA Langley Research Center, Goodyear Aerospace Corporation has performed a five-month investigation of Cone-and-Column, double-reflector, solar concentrators.

This final report describes the effort and accomplishments of the testing of the cone and concentrator and the computer analysis of the new concept for the concentration of solar power in space.

B. PROGRAM OBJECTIVE

The objective of the program was to determine the optical characteristics of the Cone-and-Column configuration and to fabricate a five-foot model to verify the findings.

C. DESCRIPTION

The fabrication, folding, and unfolding of large paraboloidal reflectors within strict weight and dimensional limitations present many problems.

Although several methods of folding paraboloidal reflectors have been investigated in detail, little attention has been given to the possibility of optically folding them. Optical folding is a technique commonly used to place conveniently parts of an optical system such as objects, images, components, and the eye. It is accomplished by placing a plane mirror in the path of the light and relocating the shadowed parts so that their images in the mirror coincide with their original positions; that is, the parts are interchanged with their images in a plane mirror (see Figure 1).

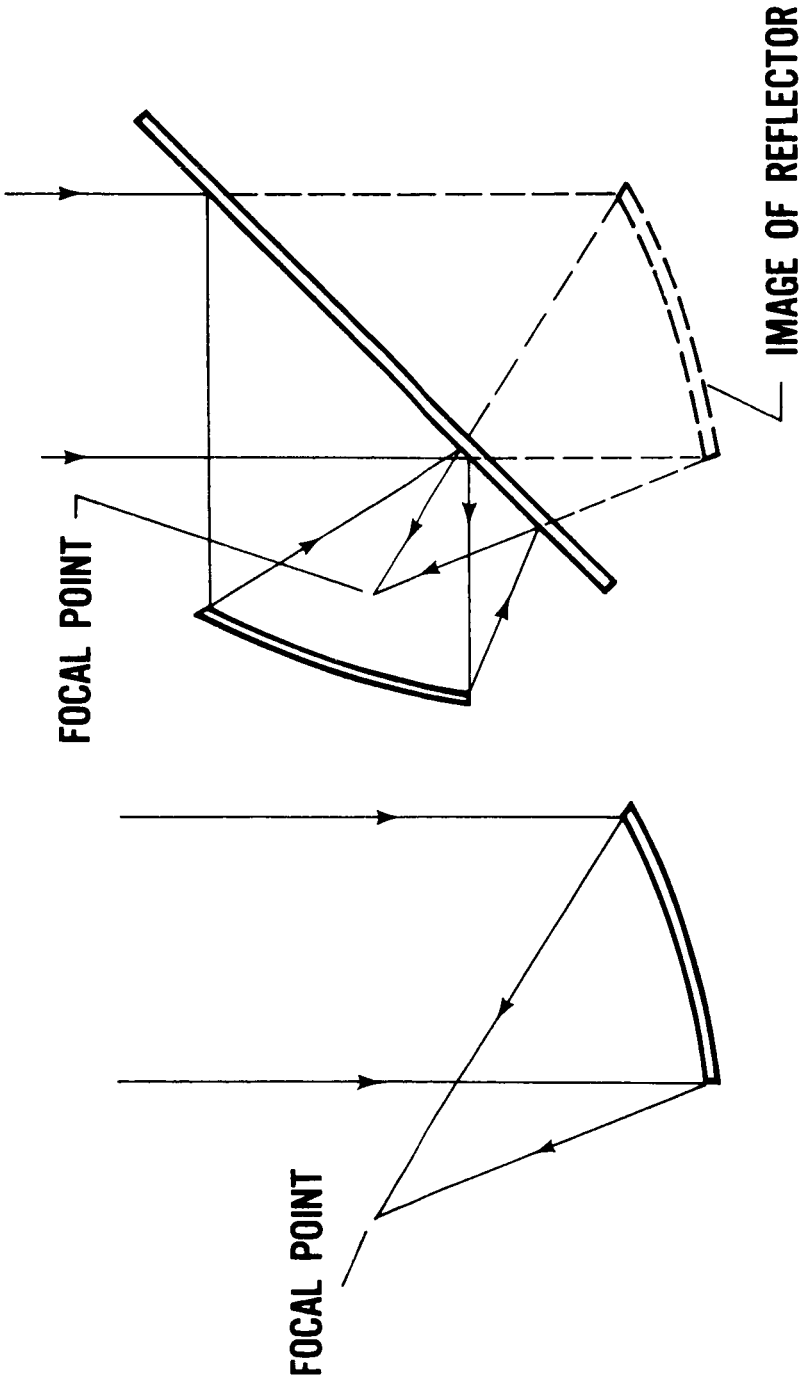

Figure 1. Optically Equivalent Systems

The principle of optical folding is extended to folding with curved mirrors with proper account taken of the magnification of curved mirrors. When a suitable conical mirror is placed in front of a paraboloidal reflector (see Figure 2), the image of the reflector is made to lie near the reflector axis. The paraboloidal reflector is interchanged with its image.

The new reflector (column reflector), combining with the conical mirror, is the optical equivalent of the paraboloidal reflector. The focal points and apertures of the two systems are identical. The column reflector is a parabola of revolution with its axis of revolution lying on the convex side of the parabola.

When a paraboloidal solar concentrator is optically folded, the area of the parabolic surface required is reduced greatly. For the primary interception of solar energy, the conical reflector is substituted for the paraboloidal reflector. Solar energy incident on the cone is reflected to the column reflector. Energy reflected from this column is focused to a point on the axis after having been reflected from the cone a second time.

The two modes of concentration of the paraboloidal reflector have been preserved. The first mode, in which rays are reflected to an axis, is due to the paraboloid being a surface of revolution. This mode is preserved by using only surfaces of revolution in the new system. The second mode, in which rays are reflected to a single point on the axis, is due to the parabolic cross section of the paraboloid. This mode is preserved by retaining the parabolic cross section in the column reflector.

Further steps can be taken to minimize the surface area of the column. From Figure 2, it is seen that the column flares at the top and at the bottom. This flaring should be minimized, not only to reduce weight and volume, but also to prevent the top of the column from intercepting rays approaching the focal point. The flaring can be alleviated by shallowing the basic paraboloid, but this operation

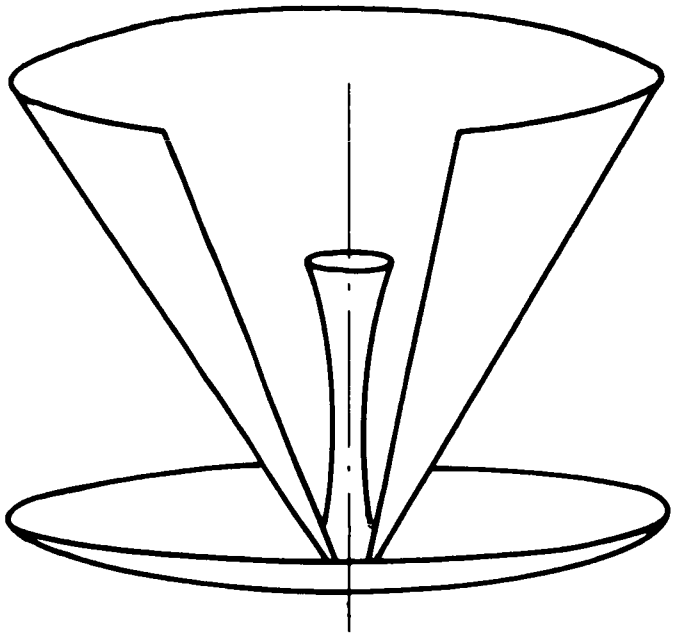

Figure 2. Optical Folding of Paraboloidal Reflector

undesirably increases the focal length. A better method is to step the surface of the basic paraboloid so that the steps lie in a straight line. The steps, then, will be segments of confocal paraboloids, and the resulting configuration will be as shown in Figure 3. To avoid the ray blockage, which is typical of Fresnel reflectors, the steps should rise as they move out from the axis on the basic paraboloids; that is, the focal lengths should decrease for succeedingly larger diameter segments. Proper stepping is accomplished by proper selection of the apex angle of the cone.

This program consisted of analytical and experimental investigations, model fabrication, testing of the assembled concentrator, and evaluation.

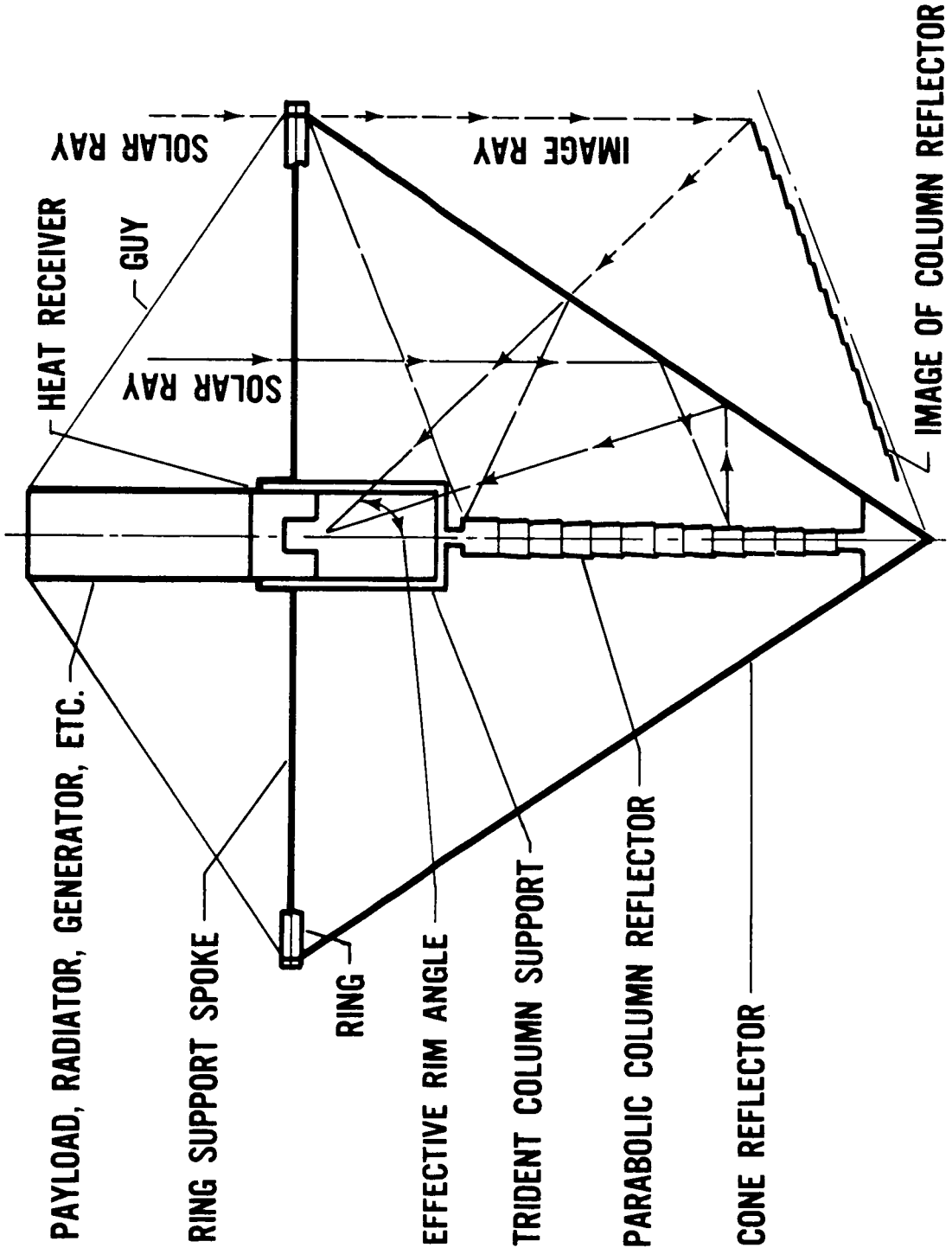

Figure 3. Cone-and-Column Reflector

SECTION II. OBJECTIVES OF INVESTIGATIONS

The analytical and experimental investigations of the program were performed to determine performance characteristics of the Cone-and-Column concentrator.

The analytical investigation determined the effects of various geometric parameters, material properties, and operating conditions on concentrator performance.

The experimental investigation determined the optical characteristics of a typical concentrator configuration. Fabrication of the model for the experimental investigation helped to define the problem areas associated with the development of this type of concentrator and assisted in the evaluation of the concept.

SECTION III. TECHNICAL APPROACH

A. EXPERIMENTAL INVESTIGATION

A five-foot diameter, conical reflector was fabricated for use in the concentrator assembly. The reflector was made by laying up aluminized Mylar on a male master. Resin and Fiberglas layers were applied to the Mylar for rigidization, and mounting flanges were added to each end of the reflector.

The use of aluminized Mylar as the reflecting surface made the model most representative of the end item.

The elements of the column reflector were individually machined and polished. The elements were vacuum-aluminized and assembled to a shaft to form the column reflector. This reflector was then assembled to the cone reflector to complete the concentrator.

The distribution of slope errors in the surface of the cone was obtained by scanning the surface with a beam and comparing the actual angle of reflectance with the ideal angle of reflectance. The difference can be resolved to the radial and tangential components of the slope errors. Examining a sufficient number of points on the cone provides the desired distribution.

The assembled concentrator was tested using collimated light. An integrating sphere collector with a phototube sensor was mounted at the focus of the concentrator behind an iris diaphragm. Size of the aperture was varied to indicate ray deviation. A collimator was directed toward the concentrator, parallel to the axis, and rotated at varying radii, to completely test all sectors of the concentrator.

Tests were also made on the concentrator with the collimator misaligned by a

preset angle. The results permitted the evaluation of the effects of concentrator misalignment.

B. OPTICAL ANALYSIS

The flux profile in the focal plane of a Cone-and-Column, solar concentrator is a function of six two-dimensional variables as follows:

(1) The intensity distribution in the solar disk.
(2) The concentrator orientation (in two axes).
(3) The surface intercepting the solar flux.
(4) The slope error distribution at the point of first reflection (radial and tangential).
(5) The slope error distribution at the point of second reflection (radial and tangential).
(6) The slope error distribution at the point of third reflection (radial and tangential).

An exact solution of the focal-plane flux profile requires a twelve-fold integration. This approach is not feasible because of the mathematical complexity.

A solution of the focal-plane flux profile, which approaches the exact solution, can be obtained by solving a number of optical rays for their points of incidence on the focal plane. This method requires that the variables governing the path of the ray be sampled in a random manner and that a sufficient number of rays be solved to obtain reasonable accuracy.

The approach taken to determine the effect of the various errors on the focal-plane image radius is to determine their effect taken one at a time. The effect of the errors in combination is then postulated and verified for several sample cases.

SECTION IV. CONE TEST

A. TEST ITEM

The initial step in the fabrication of the cone test item was the construction of a close tolerance plastic mold to the dimensions of the inside cone surface. The flange at the large end of the cone was included.

Metalized, one-mil, Mylar film with vapor deposit aluminum 400 angstroms thick was cut to size using templates. The material was seamed and then pulled over the mold so that it was as wrinkle free as possible. The metalized surface was against the mold. The material was heat-shrunk on the mold to remove all wrinkles. During this procedure the mold and material surfaces were as lint free as possible.

A spray coating of epoxy resin approximately 0.020 inch thick was applied to the film. Three plies of Type 116 glass cloth impregnated with polyester resin catalyzed for a room temperature cure were then added.

Over the Type 116 glass cloth, two stages (one of three plies and one of two plies) of Type 181 glass cloth impregnated with polyester resin catalyzed for a room temperature cure were applied.

The five plies were turned over to form the first five plies of the flange buildup. Five additional plies were then added to the flange and extended 2-1/2 inches up the cone.

The completed unit was put on the boring mill, and the small end was turned to the desired inside diameter.

When the cone was removed from the mold, a metal cap was set in place and

leveled. The cap was bonded in place by the application of reinforced plies.

The completed cone narrows from a 60-inch diameter to a 6-inch diameter. The apex half-angle equals $33^{o}45'$.

B. CONE TEST SETUP

The test setup, shown in Figure 4, included the test item, adjustable mirror mount, first surface mirror, a collimator, and a wall chart.

The first surface mirror could be rotated to the left and right and could be moved forward and backward to check cone surface errors.

A polar grid, marked on the chart, located points where the rays should strike. The wall chart was located 53 inches from the 60-inch ring on the cone. The points on the chart were compared with the actual light spots obtained by positioning of the first surface mirror.

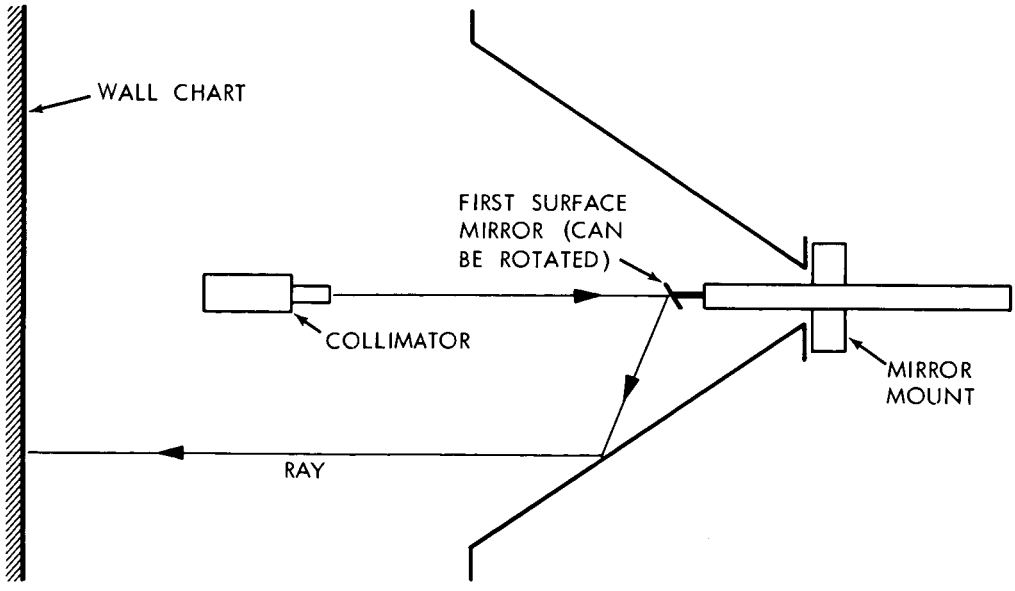

Figure 4. Cone Test Setup

C. CONE TEST DATA

The radial and tangential components of the spot displacement were measured and tabulated, as shown in Table I.

Readings were taken along rings on the cone designated A, B, C, E, G, I, K, M, N, and O having the radii shown at the top of the table. Readings were taken on azimuth lines spaced every 11-1/4 degrees and designated 1, 3, 5, 7, through 63 starting with the six o'clock position on the chart and moving counterclockwise. Outward and clockwise displacements are marked +; opposite are marked -. The readings are in inches.

D. CONE TEST RESULTS

The pattern of the spots on the wall chart indicated a persistent error due to misalignment between the projection system and the cone.

The data was therefore analyzed to determine the nature and magnitude of this misalignment. When radial spot displacement was plotted against azimuth angle for each ring on the cone, the data points fell near a vertically displaced sine wave.

Analysis of the effects of misalignment of the cone with respect to the projection system showed the following:

(1) Axial translation of the cone will cause a vertical shift of the data points for radial spot displacement.
(2) An error in the angular setting of the projection mirror will cause a vertical shift of the data points for radial spot displacement.
(3) A radial translation of the cone will generate a sine wave in both the radial and tangential spot displacement curves.
(4) Rotation of the cone will generate a sine wave in both the radial and tangential spot displacement curves.

It was further noted that an odd number of sine waves cannot be generated by a

Table I. Cone Test Spot Displacement

AZIMUTH NO.	RING DESIGNATIONS AND RADII (inches)									
	A (3.63)	B (5.48)	C (7.33)	E (11.02)	G (14.72)	I (18.41)	K (22.11)	M (25.81)	N (27.65)	O (29.50)
1 (r)	Missing	0	-0.2	+0.1	-0.1	-0.3	-0.1	-0.3	-0.2	-0.3
1 (t)		0	-0.4	-0.3	-0.1	-0.1	-0.3	-0.5	-0.2	-0.4
3 (r)						-0.1	+0.1	-0.2	-0.2	+0.4
3 (t)						+0.2	+0.1	+0.3	-0.2	-0.2
5 (r)			-0.1	0.0	0.0	-0.1	+0.1	+0.1	-0.3	+1.8
5 (t)			-0.5	-0.2	-0.3	-0.3	-0.3	-0.2	-0.2	-0.2
7 (r)						-0.1	+0.2	+0.4	+0.2	+1.3
7 (t)						-0.5	-0.5	-0.2	-0.4	-0.4
9 (r)	Missing	+0.5	+0.5	+0.7	+0.2	+0.2	+0.3	+0.4	+0.1	-0.1
9 (t)		-0.5	-0.4	-0.9	-0.5	-0.4	-0.4	-0.3	-0.4	-0.2
11 (r)						+0.4	+0.9	+0.3	+0.2	+0.9
11 (t)						-0.3	+0.2	+0.1	-0.1	-0.2
13 (r)			+0.5	+0.1	+0.5	+0.3	+0.7	+0.4	+0.6	+1.6
13 (t)			-0.4	-0.2	-0.1	0.0	-0.2	-0.1	-0.1	-0.1
15 (r)						+0.5	+0.6	+0.5	+0.6	+1.0
15 (t)						-0.1	-0.1	-0.1	0.0	-0.2
17 (r)	+1.2	+1.0	+0.7	+0.8	+0.4	+0.6	+0.7	+0.6	+0.5	+0.8
17 (t)	-0.9	-0.5	-0.4	-0.3	-0.1	0.0	-0.1	0.0	+0.1	-0.1
19 (r)						+0.6	+0.7	+0.7	+0.9	+1.5
19 (t)						-0.3	-0.1	-0.3	+0.1	-0.2
21 (r)			+0.5	+0.8	+0.7	+0.7	+0.5	+0.8	+0.7	+2.6
21 (t)			-0.2	+0.1	-0.1	-0.1	0.0	+0.1	-0.1	+0.1
23 (r)						+0.6	+0.8	+0.8	+1.1	+1.6
23 (t)						-0.2	0.0	+0.2	+0.2	-0.2
25 (r)	+1.7	+0.9	+0.6	+0.6	+0.6	+0.6	+0.9	+0.7	+0.5	+3.6
25 (t)	-0.4	-0.2	-0.2	+0.1	+0.1	+0.1	+0.1	0.0	-0.3	-0.3
27 (r)						+0.8	+0.6	+0.7	+1.2	+3.4
27 (t)						0.0	+0.1	+0.3	+0.1	-0.5
29 (r)			+0.7	+0.7	+0.6	+0.7	+0.8	+0.9	+0.8	+1.8
29 (t)			+0.1	+0.1	-0.1	-0.1	-0.1	-0.1	0.0	-0.2
31 (r)						+0.7	+0.7	+1.0	+0.9	+2.7
31 (t)						0.0	+0.2	+0.1	+0.1	+0.2

NOTES: r = Radial component, + = outward, - = inward, inches.
t = Tangential component, + = clockwise, - = counterclockwise, inches.

Table I. Cone Test Spot Displacement (Continued)

AZIMUTH NO.	RING DESIGNATIONS AND RADII (inches)									
	A (3.63)	B (5.48)	C (7.33)	E (11.02)	G (14.72)	I (18.41)	K (22.11)	M (25.81)	N (27.65)	O (29.50)
33 (r)	+0.9	+0.8	+0.6	+0.6	+0.8	+0.7	+0.9	+0.9	+0.7	+2.6
33 (t)	0.0	+0.1	-0.1	-0.3	0.0	-0.1	-0.3	-0.2	+0.1	0.0
35 (r)						+0.7	+0.7	+1.2	-0.5	+4.1
35 (t)						+0.1	+0.5	+0.6	+0.1	+0.4
37 (r)			+0.5	+0.4	+0.4	+0.6	+0.6	+0.7	+1.0	+3.4
37 (t)			0.0	+0.1	+0.1	+0.2	+0.3	+0.2	+0.1	+0.3
39 (r)						+0.6	+0.8	+0.6	0.0	+2.2
39 (t)						0.0	+0.3	+0.1	+0.1	+0.3
41 (r)	+0.7	+0.7	+0.4	+0.2	+0.3	+0.5	+0.9	+0.6	+0.5	+3.4
41 (t)	-0.4	-0.1	+0.1	+0.1	+0.1	+0.2	+0.1	+0.1	0.0	-0.1
43 (r)						+0.5	+0.6	+0.6	-0.2	+2.3
43 (t)						+0.1	+0.4	+0.3	+0.1	+0.4
45 (r)			-0.1	+0.3	+0.4	+0.4	+0.4	+0.6	+1.1	+2.1
45 (t)			0.0	+0.1	0.0	+0.4	+0.3	+0.2	+0.1	+0.3
47 (r)						+0.3	+0.3	+0.4	-0.9	+2.0
47 (t)						+0.4	+0.3	+0.5	+0.4	+0.4
49 (r)	+0.4	+0.3	-0.1	+0.2	+0.2	+0.2	+0.3	+0.1	-0.2	+0.3
49 (t)	-1.3	-0.8	-0.4	-0.2	+0.3	+0.2	+0.3	+0.4	+0.4	+0.3
51 (r)					0.0	0.0	0.0	+0.2	+0.3	+0.3
51 (t)					+0.6	+0.4	+0.3	+0.4	+0.4	+0.4
53 (r)			-0.3	0.0	-0.3	0.0	-0.1	-0.3	-0.2	+0.3
53 (t)			-0.6	+0.2	+0.6	+0.7	+0.5	+0.4	+0.2	+0.5
55 (r)						-0.3	0.0	-0.2	+0.1	+0.3
55 (t)						+0.4	+0.4	+0.3	+0.7	+0.6
57 (r)	-0.2	-0.4	-0.5	-0.3	-0.4	-0.4	-0.2	-0.2	0.0	-0.5
57 (t)	-0.6	-2.0	+1.0	0.0	+0.3	+0.3	+0.3	+0.4	+0.5	+0.1
59 (r)						-0.4	-0.6	-0.6	-0.3	-0.4
59 (t)						+0.2	+0.2	+0.2	+0.1	+0.5
61 (r)			-0.4	-0.4	-0.3	-0.5	-0.3	-0.7	-0.2	0.0
61 (t)			-0.4	-0.6	-0.2	-0.1	-0.2	0.0	+0.1	+0.1
63 (r)						-0.3	-0.2	-0.4	+0.1	+0.3
63 (t)						-0.3	+0.1	+0.1	-0.1	-0.2

NOTES: r = Radial component, + = outward, - = inward, inches.
t = Tangential component, + = clockwise, - = counterclockwise, inches.

general distortion of the cone. A vertical shift in the radial displacement curve can be caused by an error in the cone apex angle, but this possibility was ruled out by a dimensional check of this angle.

In view of these considerations, it was concluded that there was a persistent error in the data due to optical misalignment and that it was appropriate to separate this error to evaluate the cone properly.

The five components of misalignment (with reference to the apex of the cone) are the three orthogonal translation vectors, the degree of rotation, and the orientation of the rotational axis. These components were determined from the five observations: phase angle and amplitude of the sine curves for the radial spot displacement data and for the tangential spot displacement data, and the vertical shift of the radial spot displacement data. There was some variance in the results between rings on the cone, and a weighted average was taken to determine the most probable misalignment. As shown in Figure 5, the values obtained were as follows:

(1) Axis of rotation = 53 degrees with vertical.
(2) Degree of rotation = 7.3 minutes.
(3) Translation along axis of rotation = 0.00 inch.
(4) Translation perpendicular to axis of rotation = 0.15 inch.
(5) Translation along optical axis = 0.35 inch.

The data displacement curves associated with this misalignment were plotted on the data plots. The deviation of the data points from these curves is then indicative of the surface slope inaccuracies of the cone. This deviation for the various rings is presented in Figures 6 through 15.

The rms surface slope error for each ring is tabulated in Table II. The weighted rms average is 6.4 minutes tangential, 16.2 minutes radial or, if the outermost ring is excluded, 5.7 minutes tangential, 6.4 minutes radial.

Table II. RMS Surface Slope Error

RING	RADIUS	ROOT MEAN SQUARE SLOPE ERROR-MIN.		WEIGHT
		RADIAL	TANGENTIAL	
A	3.63	8.26	4.68	.21
B	5.47	4.46	4.66	.37
C	7.32	4.44	4.13	.75
E	11.02	4.92	3.66	1.51
G	14.71	3.92	3.79	2.02
I	18.41	3.91	3.72	2.52
K	22.10	5.76	4.78	3.03
M	25.80	6.04	8.16	2.66
N	27.65	11.95	8.13	1.88
O	29.50	49.10	10.99	1.53
TOTAL	-	16.16	6.39	16.48

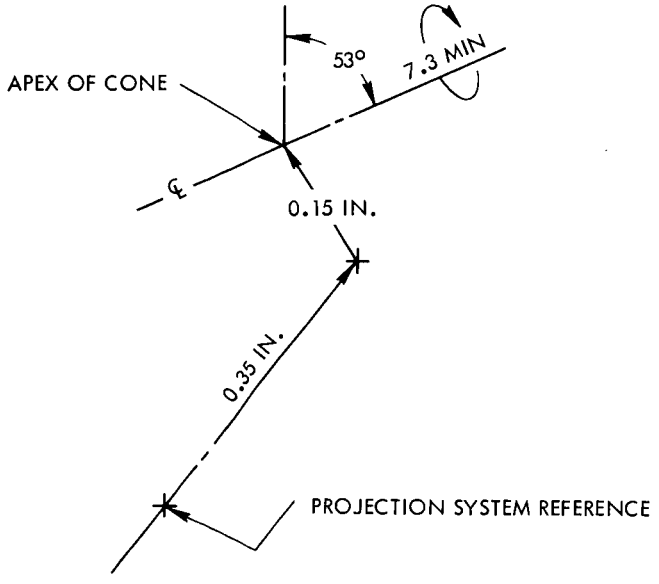

Figure 5. View into Cone Showing Calculated Misalignment of Cone with Projection System

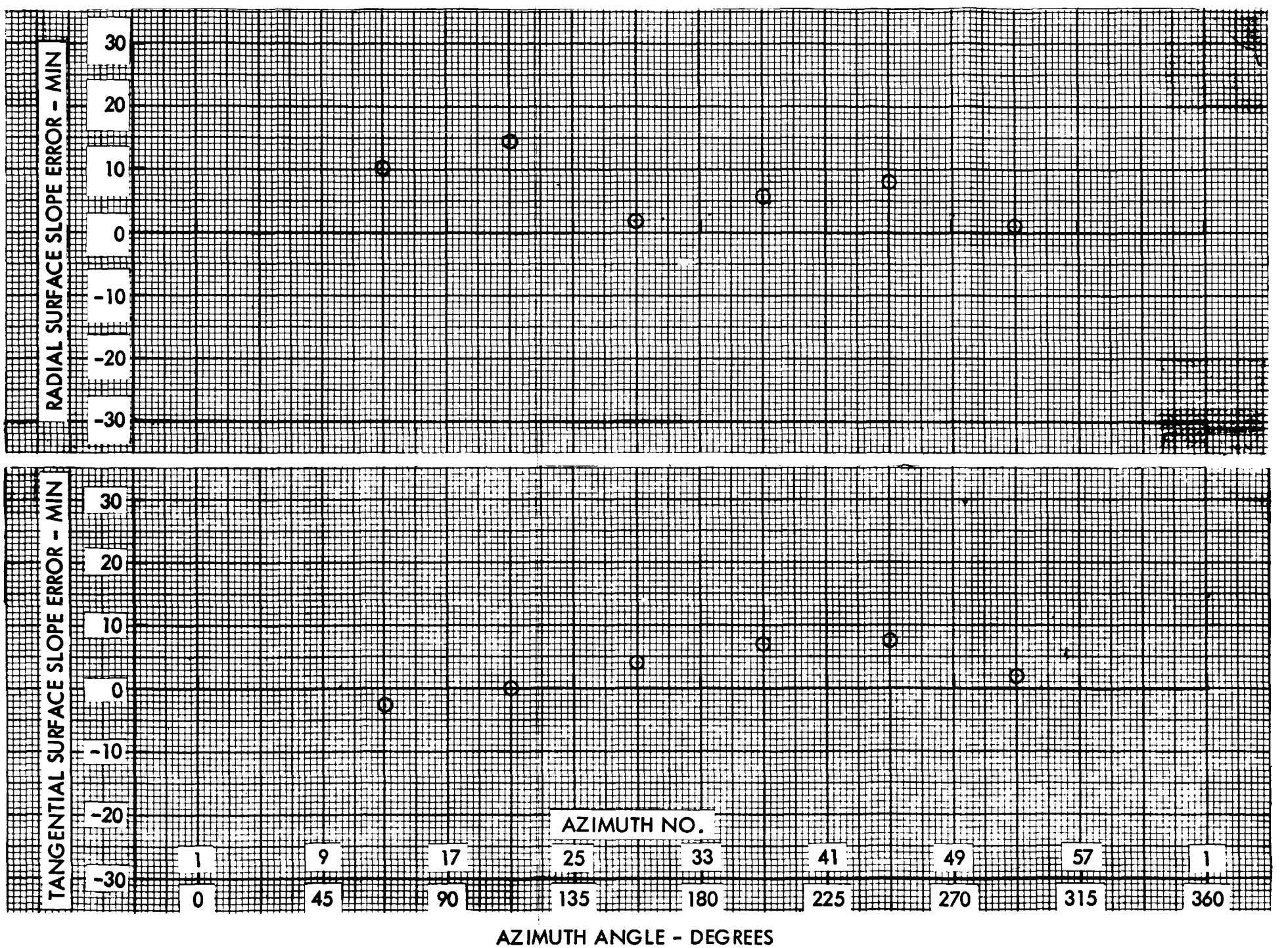

Figure 6. Cone Surface Slope Error at Radius of 3.63 Inches

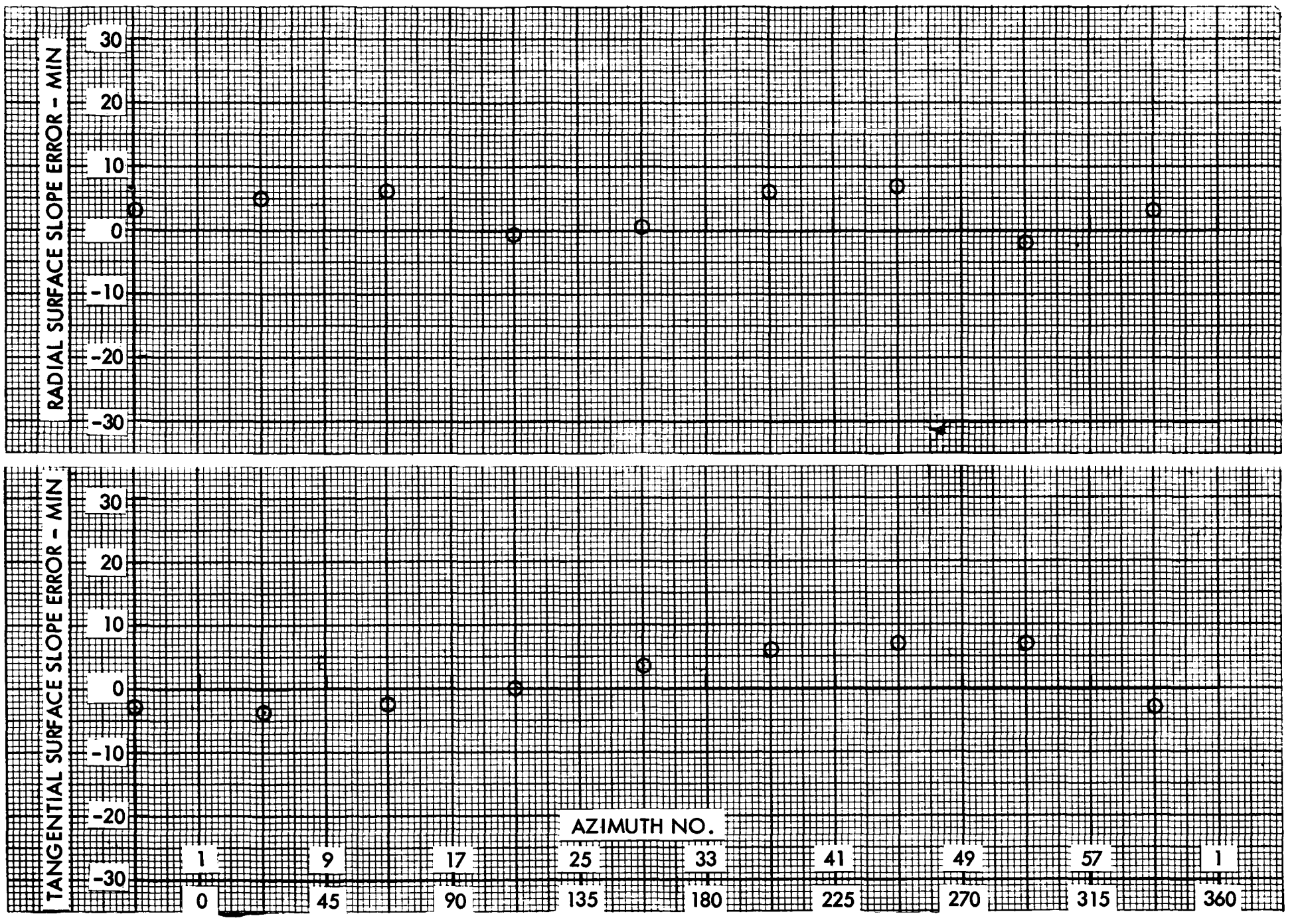

Figure 7. Cone Surface Slope Error at Radius of 5.48 Inches

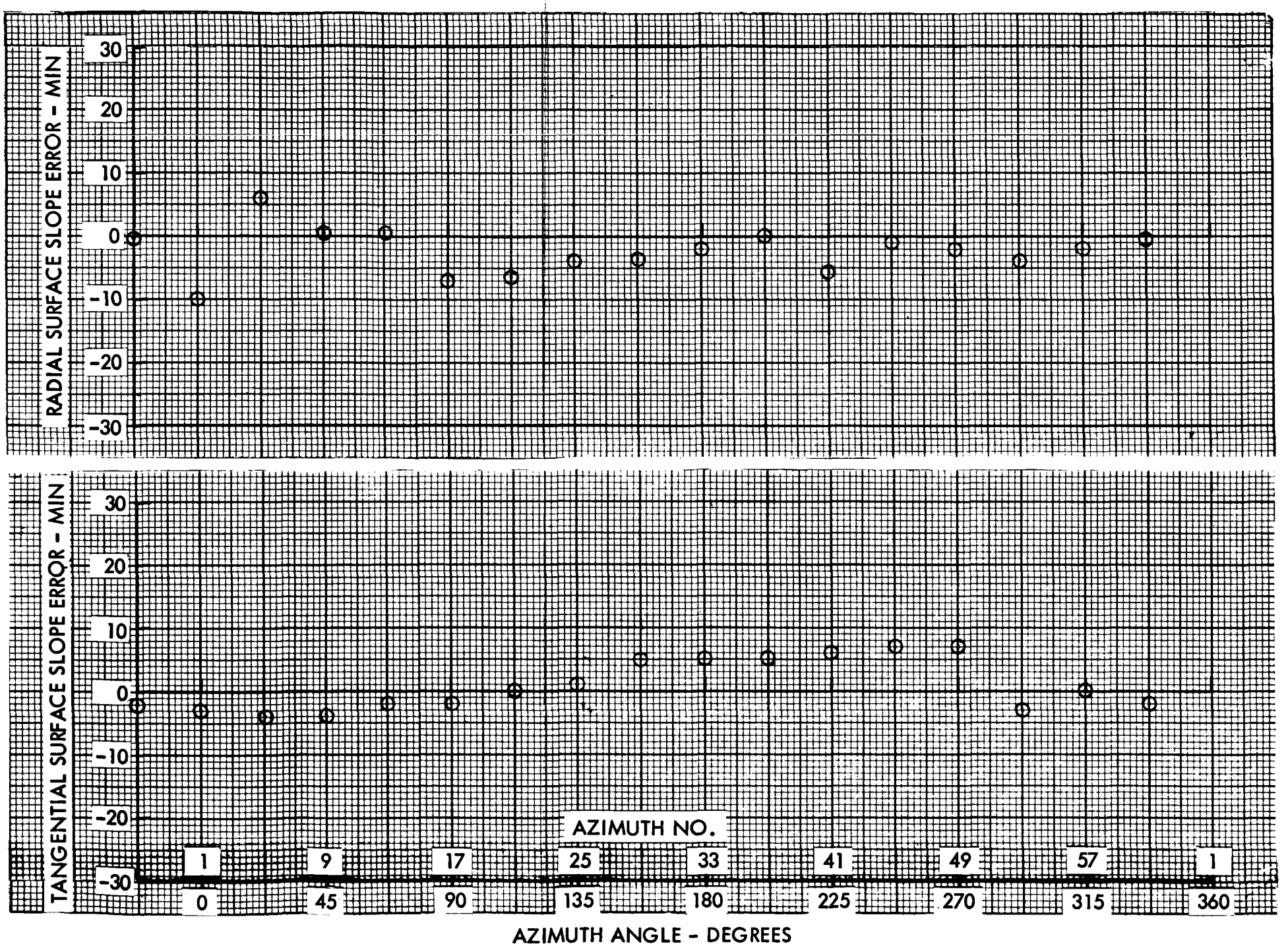

Figure 8. Cone Surface Slope Error at Radius of 7.33 Inches

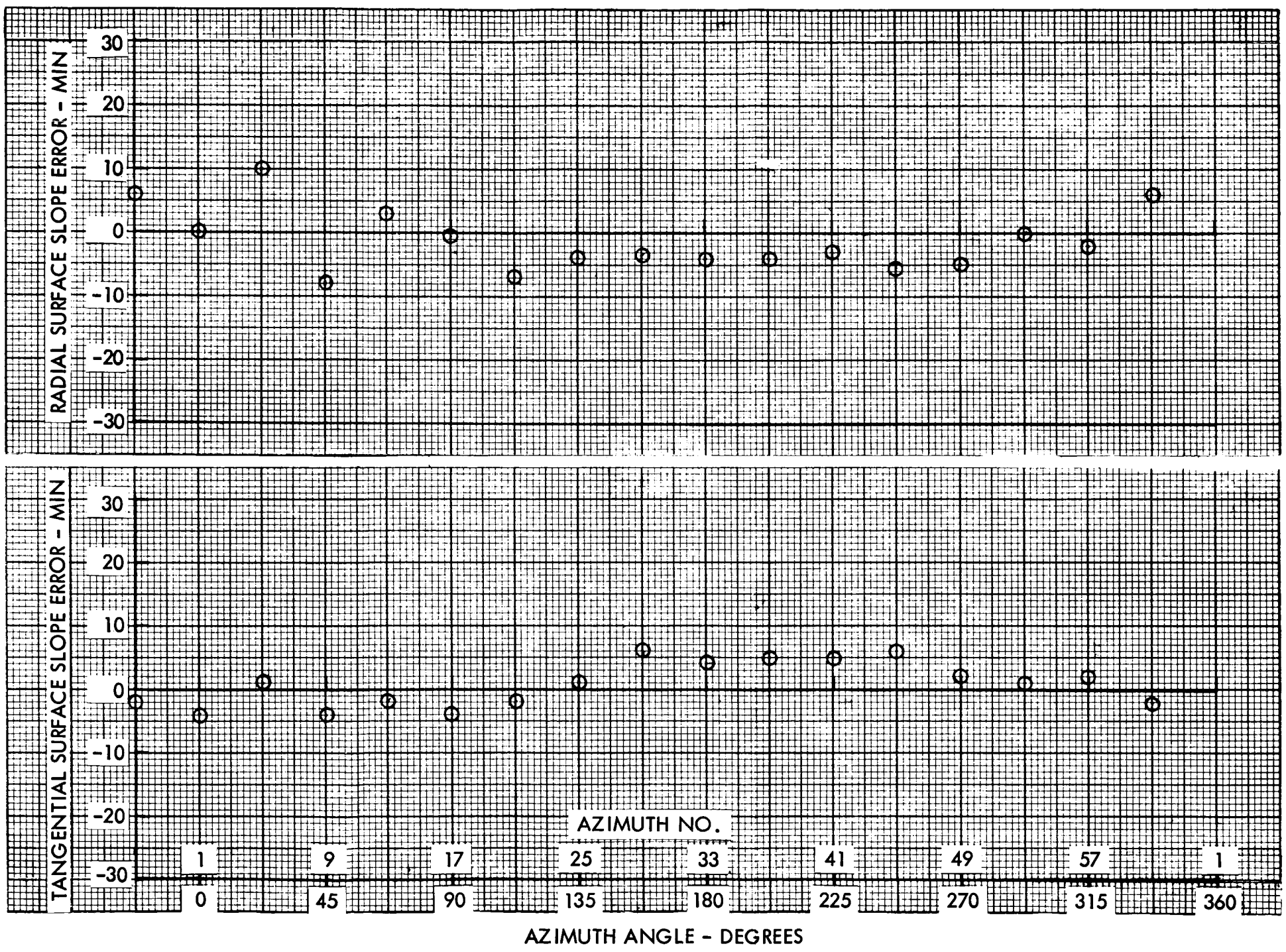

Figure 9. Cone Surface Slope Error at Radius of 11.02 Inches

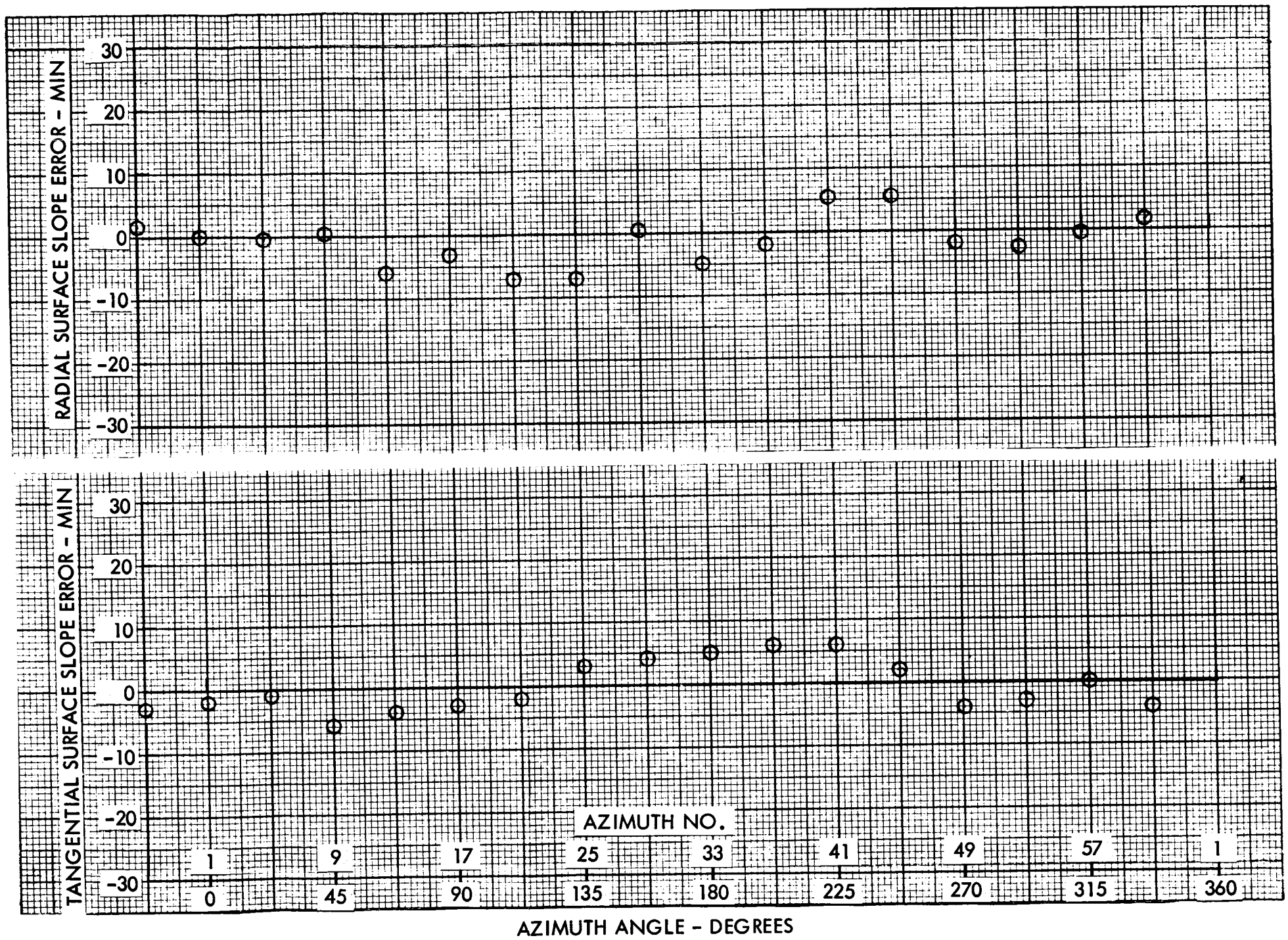

Figure 10. Cone Surface Slope Error at Radius of 14.72 Inches

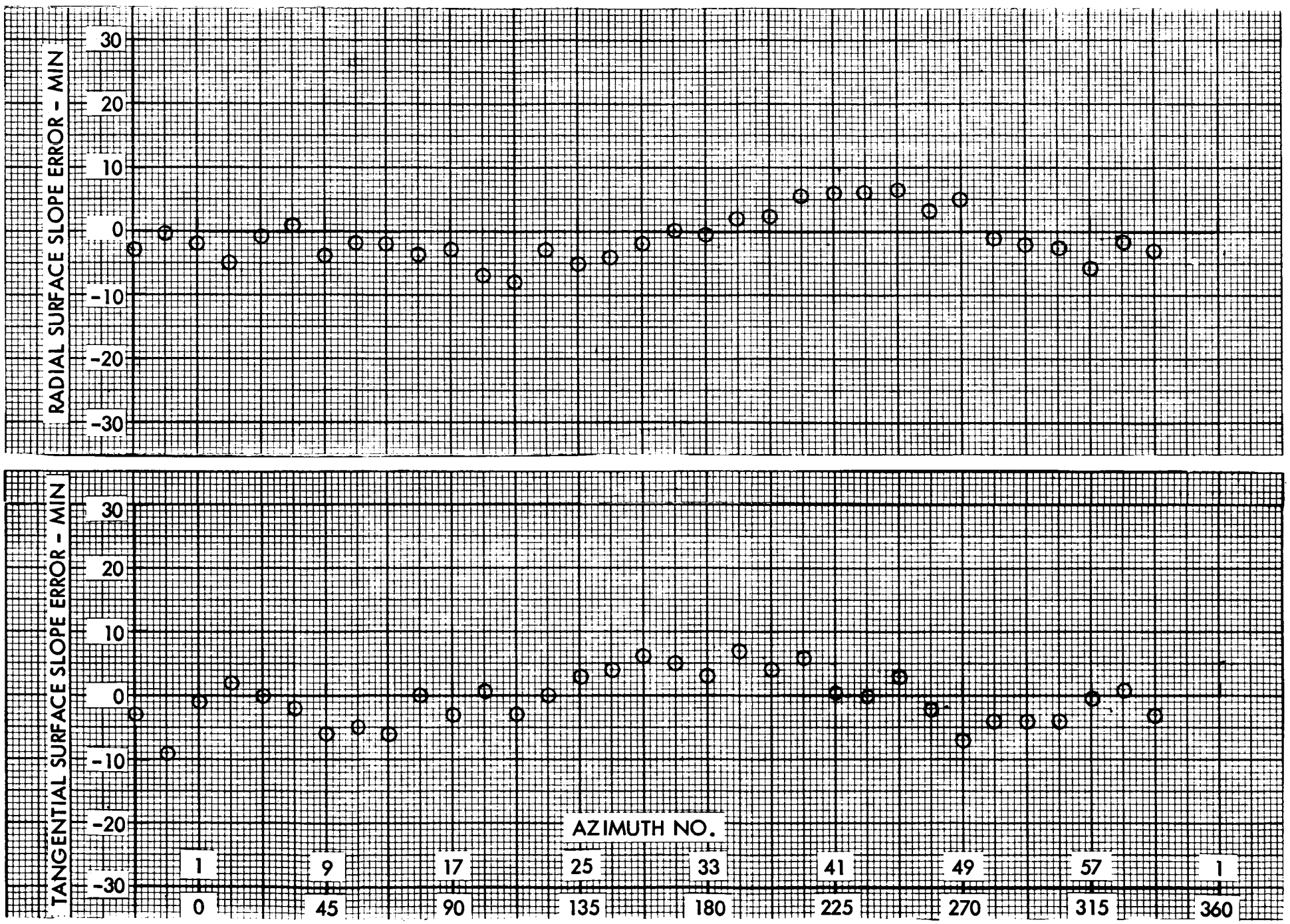

Figure 11. Cone Surface Slope Error at Radius of 18.41 Inches

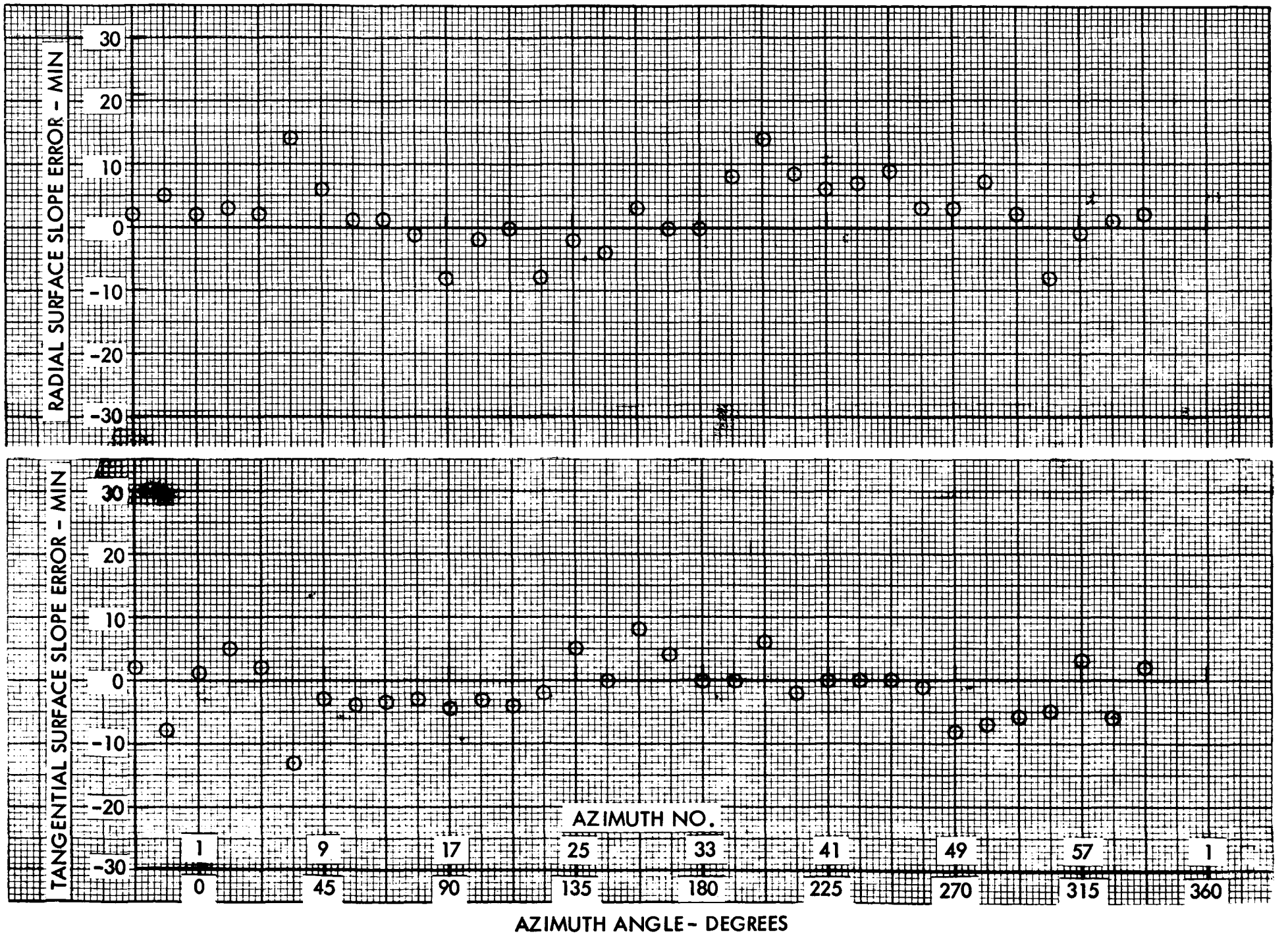

Figure 12. Cone Surface Slope Error at Radius of 22.11 Inches

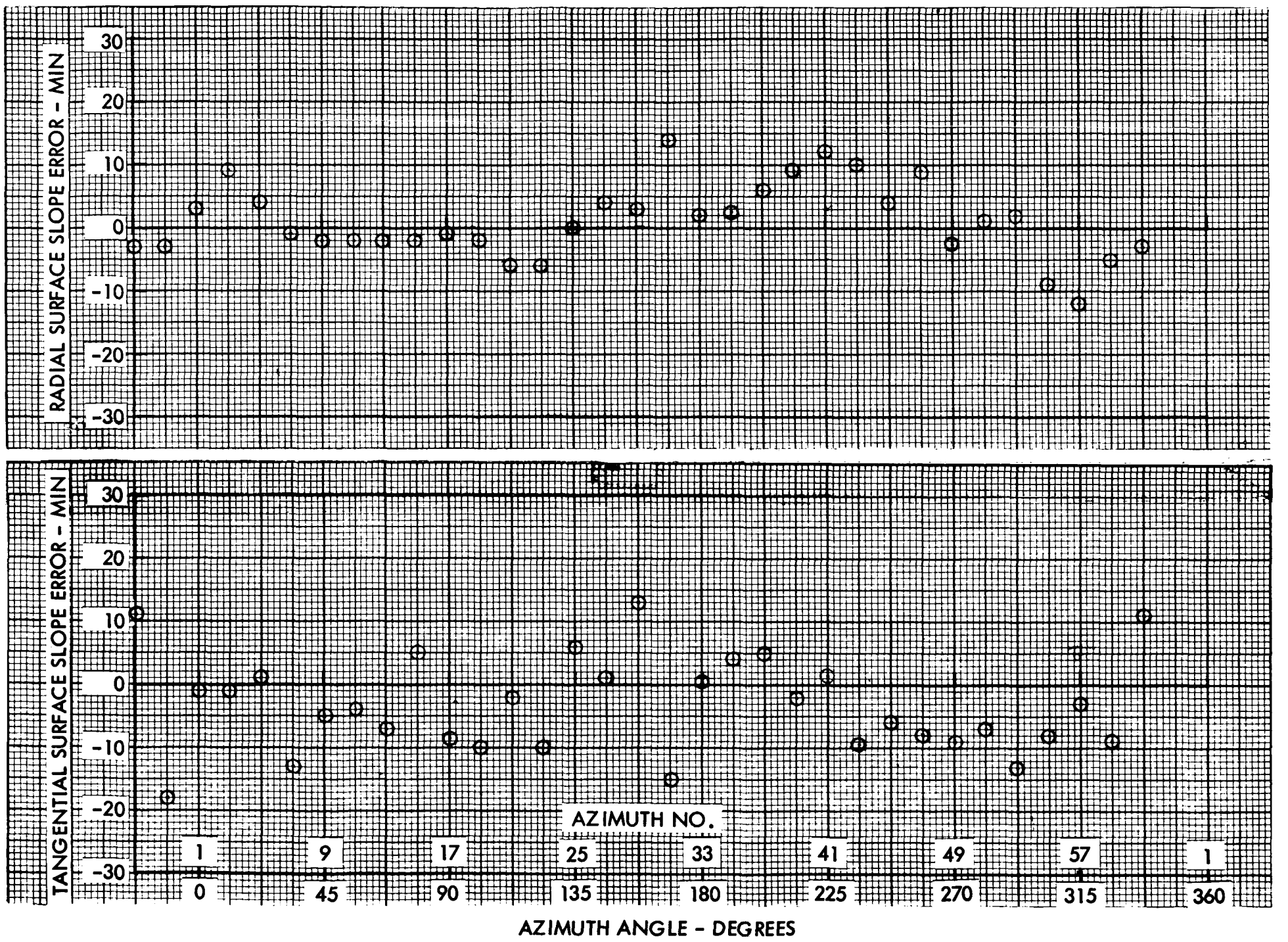

Figure 13. Cone Surface Slope Error at Radius of 25.81 Inches

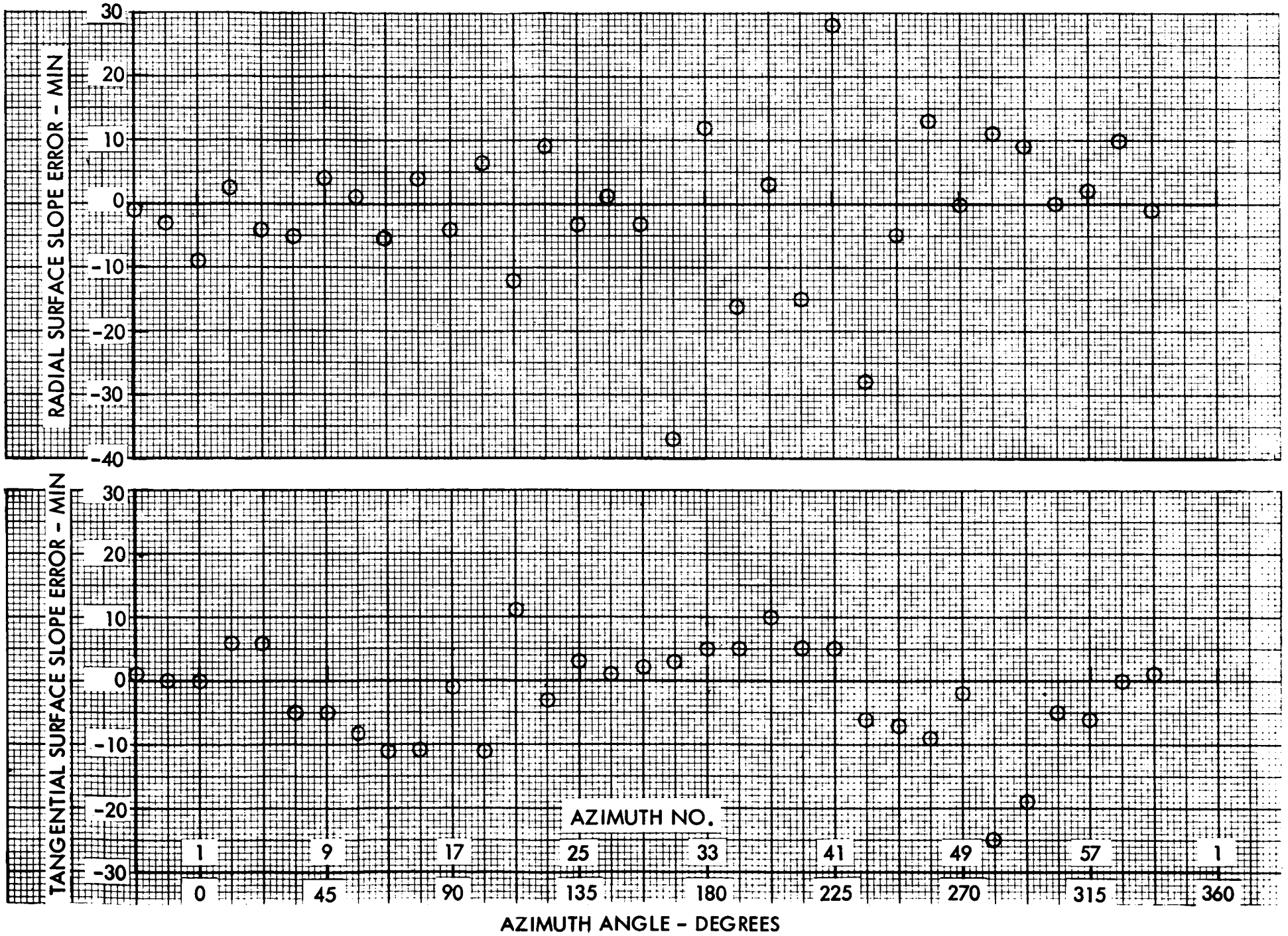

Figure 14. Cone Surface Slope Error at Radius of 27.65 Inches

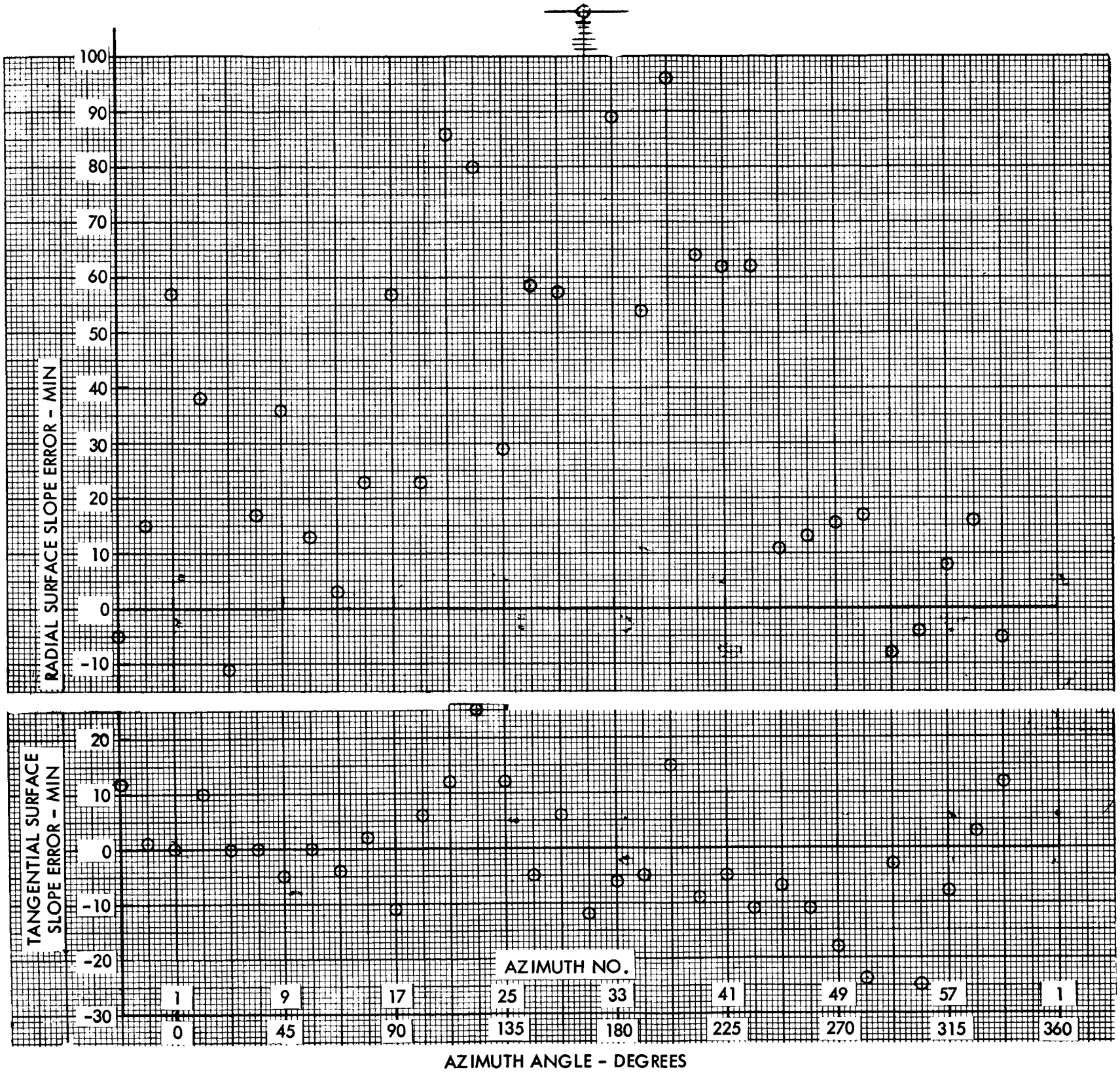

Figure 15. Cone Surface Slope Error at Radius of 29.50 Inches

SECTION V. CONCENTRATOR TEST

A. TEST ITEM

1. Test Concentrator Design

The test concentrator was designed to demonstrate and verify the principles of operation of the Cone-and-Column concentrator configuration. Features of the test concentrator which are similar to a flight model are as follows:

(1) The optical principles are identical.

(2) The column is of a configuration which can be folded to one-third of its length.

(3) The inside diameter of the cone is one-tenth of the outside diameter.

(4) The reflecting surface of the cone is an aluminized film.

(5) The reflecting surface of the column is vapor deposited aluminum with a nickel substrate and a silicon oxide overcoating.

Features of the test concentrator which are not similar to a flight model are as follows:

(1) The structure is rigid and is not foldable.

(2) No attempt has been made to minimize weight.

(3) The sixty-inch diameter is much smaller than the anticipated diameter of flight models.

(4) The reflectance of the mirror surfaces is less than that expected for flight models.

The geometry of the test concentrator is described by the following dimensions:

(1) Outside diameter of cone reflecting surface = 60 in.
(2) Inside diameter of cone reflecting surface = 6 in.
(3) Apex half-angle of cone = 33.75 degrees.
(4) Distance of focal point from aperture plane = 0.710 in. (inside).
(5) Distance of top of column from aperture plane = 11.753 in.
(6) Number of column sections = 3.
(7) Minimum radii of top, middle, and bottom column sections = 1.630, 1.111, and 0.679 in.

A more detailed description of the geometry may be obtained by referring to Figure 16. This concentrator geometry provides an effective rim angle of 45 degrees; i.e., the maximum angle made by rays through the focal point with the optical axis is 45 degrees.

2. Concentrator Fabrication

The fabrication of the cone reflector is described in Section II. The column reflector was made in three sections which were assembled onto a one-inch-diameter rod. The rod was welded to a flange which matched the flange on the small end of the cone. The following sequence of operations was employed to obtain the reflecting surface of the column:

(1) The parabolic contours were calculated and transferred to templates.
(2) The column sections were machined from 4340 steel on a tracer lathe using the parabolic templates.
(3) The reflecting surfaces were polished to a surface finish of three to four microinches rms.
(4) The sections were plated with 0.0002 to 0.0005 inch of copper and 0.0004 to 0.0010 inch of nickel using the Harshaw Nubrite process.

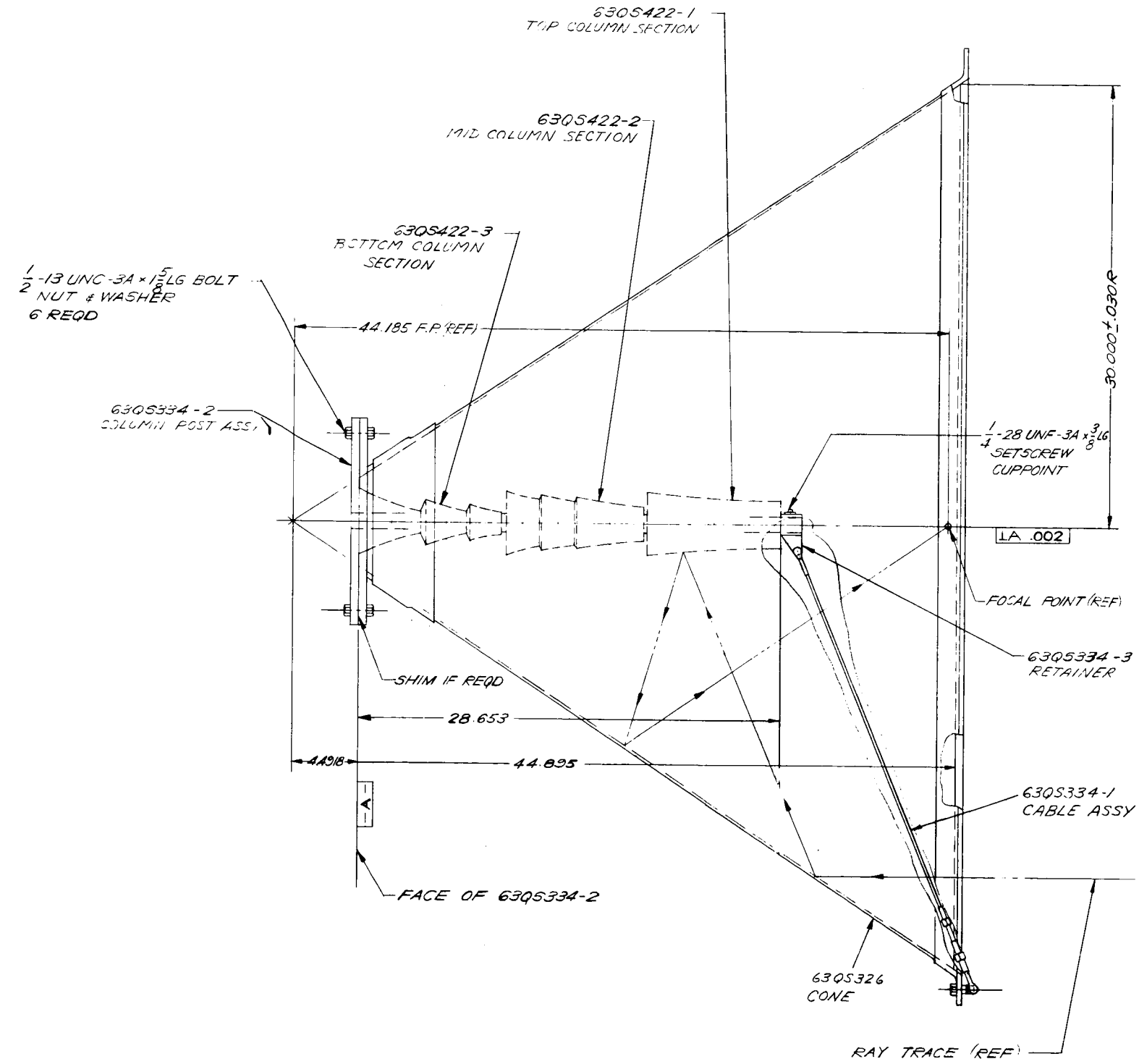

Figure 16. Test Concentrator Geometry

(5) The sections were vacuum-vapor coated with 400 to 2000 angstroms of aluminum and approximately one micron of silicon oxide.

The process used was one which has not been developed to its fullest potential. Each step in the process could be improved, but the attendant development efforts were not warranted in view of the objectives of this model.

B. CONCENTRATOR TEST SETUP

1. Description

The test setup, as shown in Figures 17 and 18, included the test item, an integrating sphere with a variable aperture, a collimator mounted on an adjustable, rotating arm, and a wall reference chart.

The integrating sphere reflectometer was located in the focal plane of the concentrator. Iris diaphragm openings of from four inches (full open) to one inch were possible. A 1P21 photomultiplier provided the pickup in the optical sensor.

A 300-watt projection bulb was the collimator light source with the illuminated aperture at the objective lens focus point. The diameter of the beam coming out was approximately 1 inch.

2. Test Procedure

The cone was previously aligned to the Cone-and-Column axis, and the reference chart was aligned to the same axis.

The position of the collimator was referenced on the chart through a back spot projector which was a part of the collimator assembly.

The collimator was adjusted to a maximum collimation error of 9.5 minutes and was aligned parallel to the optic axis of the concentrator.

The concentrator efficiency at various locations was determined using collimated light and an integrating sphere with a variable aperture.

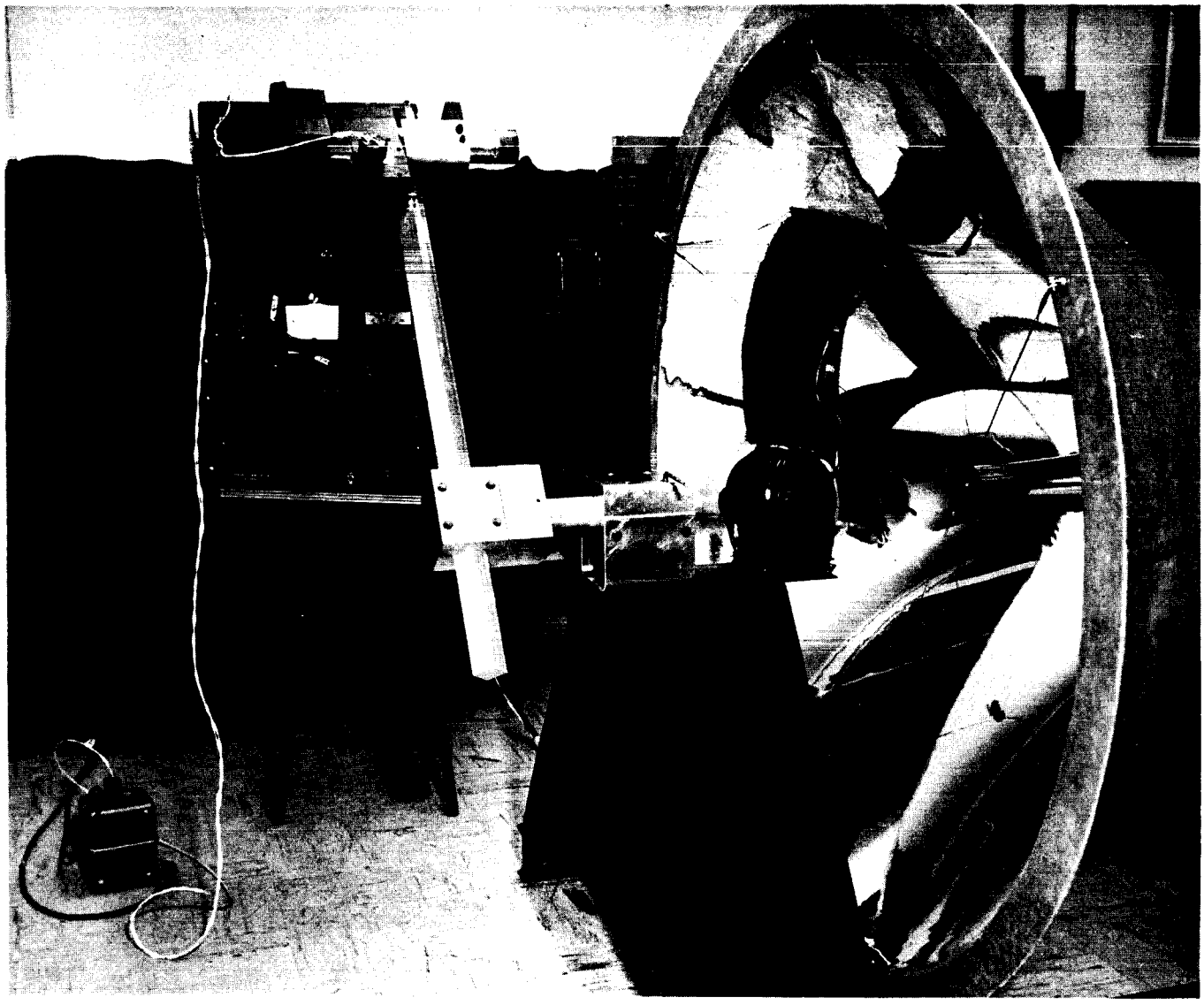

Figure 17. Concentrator Test Setup Showing Cone and Column

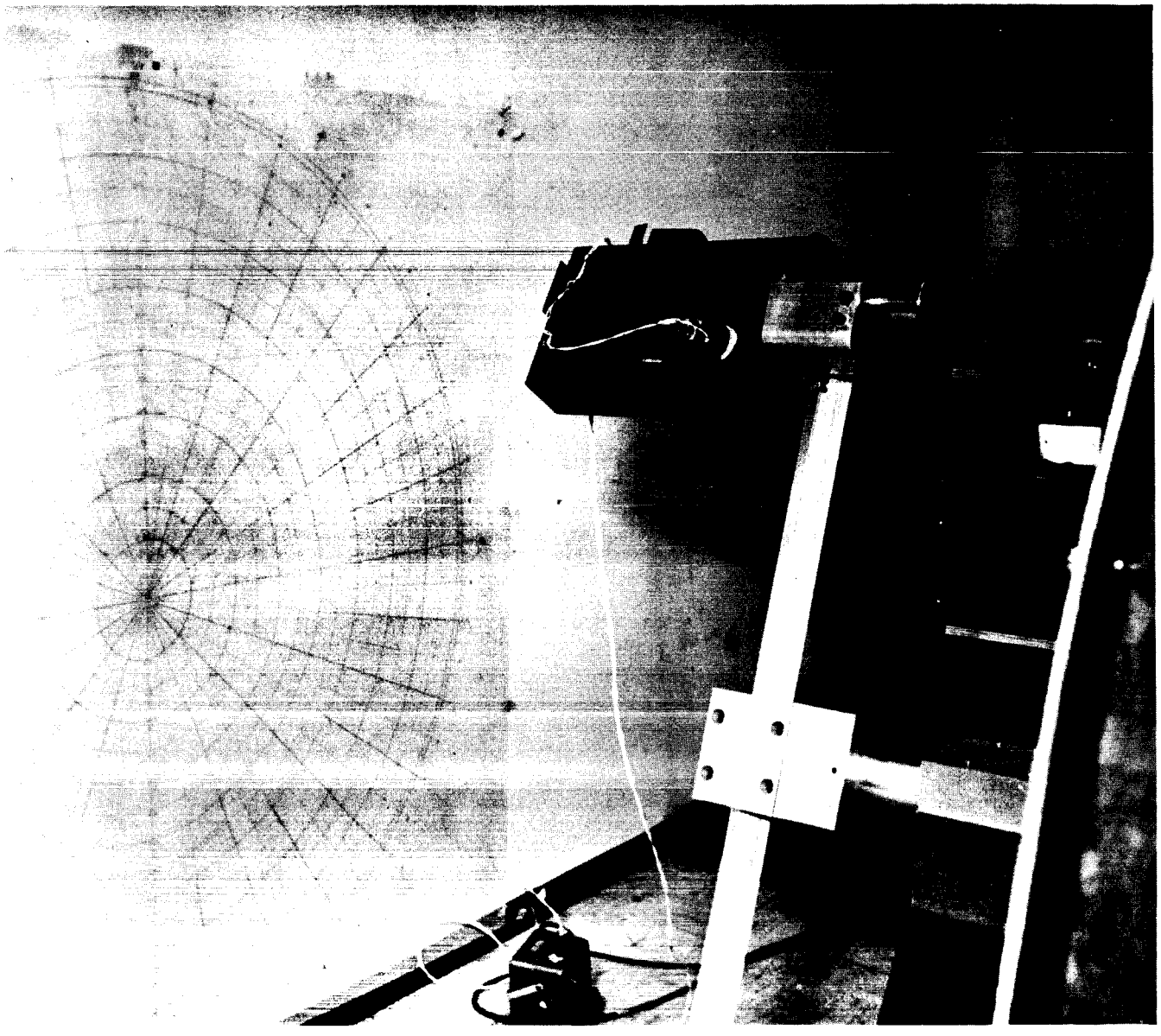

Figure 18. Concentrator Test Setup Showing Chart

Readings of the integrating sphere output were taken at three axial locations on each of the three column sections, at six azimuth angles, and at four aperture sizes on the integrating sphere.

A reading was also taken with the collimated beam projected in the integrating sphere in order to determine the over-all reflectance of the concentrator.

The reflectance of the cone was determined by placing the integrating sphere in the path of the beam after one reflection.

Readings were also taken of the ambient light level to determine that contribution to integrating sphere output.

C. CONCENTRATOR TEST DATA

The readings obtained from the concentrator tests are tabulated in Tables III through VI. Where the collimated light beam was blocked by support structure, the reading was taken on an adjacent azimuth as indicated by the figure in parentheses. With the beam projected directly into the integrating sphere the output reading was 246. The average ambient reading was 6.

Tests were made with the collimator misaligned with the concentrator axis. Readings of the integrating sphere output were made at six azimuths with the point of second reflection on the middle step of the middle column section. The corresponding radius at the first reflection was between 15 and 16 inches. Readings were taken with aperture diameters of 1, 2, 3, and 4 inches with misalignment angles of 0, 0.5, and 1.0 degrees in both tangential directions and both radial directions. The data obtained is given in Tables VII through X. Alignment errors were taken as positive when the collimated beam moved outward or counterclockwise when viewed from behind the collimator.

Table III. Integrating Sphere Output - Four-Inch Aperture

RING		BB+.56	CC+.50	DD+1.50	FF+.12	GG+.50	HH+.75	JJ	LL	NN	TOTAL
RADIUS		6.04	7.82	10.68	13.00	15.22	17.32	20.26	23.96	27.66	-
AZIMUTH	6	100	106	105	101	104	105	100	96	98	915
	17	104	102	105	95	106	108	95	96	95	906
	28	83(29)	85	83	87	90	95	85	86	87	781
	38	74(37)	57	80	83	82	90	64	90	89	709
	49	83	87	94	100	99	103	90	98	98	852
	60	95	102	101	100	103	105	95	100	97	898
SUM		539	539	568	566	584	606	529	566	564	5061
EFF. Δ		.341	.341	.360	.359	.371	.386	.334	.359	.368	-
WT		.0434	.0417	.0607	.0654	.0729	.0982	.1509	.1970	.2598	1.0000*
WT. EFF.		.0147	.0142	.0198	.0234	.0270	.0379	.0504	.0707	.0956	.3537

* INCLUDES .0100 WT AT 0 RADIUS
Δ REDUCED BY AVERAGE AMBIENT OF 6

Table IV. Integrating Sphere Output - Three-Inch Aperture

RING		BB+.56	CC+.50	DD+1.50	FF+.12	GG+.50	HH+.75	JJ	LL	NN	TOTAL
RADIUS		6.04	7.82	10.68	13.00	15.22	17.32	20.26	23.96	27.66	-
AZIMUTH	6	12	61	36	51	90	72	49	38	8	417
	17	8	11	7	16	30	13	29	25	26	165
	28	9(29)	34(29)	13	34	34	24	41	47	29	265
	38	14(37)	20(37)	9	28	16	13	10	33	11	154
	49	10	22	9	43	39	20	11	24	16	194
	60	35	63	38	72	91	89	59	30	69	546
SUM		88	211	112	244	300	231	199	197	159	1741
EFF. Δ		.035	.118	.051	.141	.179	.132	.111	.111	.083	-
WT.		.0434	.0417	.0607	.0654	.0729	.0982	.1509	.1970	.2598	1.0000*
WT. EFF.		.0015	.0049	.0031	.0092	.0130	.0129	.0167	.0218	.0215	.1046

* INCLUDES .0100 WT AT 0 RADIUS
Δ REDUCED BY AMBIENT AVERAGE OF 6

Table V. Integrating Sphere Output - Two-Inch Aperture

RING		BB+.56	CC+.50	DD+1.50	FF+.12	GG+.50	HH+.75	JJ	LL	NN	TOTAL
RADIUS		6.04	7.82	10.68	13.00	15.22	17.32	20.26	23.96	27.66	-
AZIMUTH	6	43	102	104	84	108	105	91	90	8	735
	17	34	71	58	73	105	88	86	91	64	670
	28	35(29)	74(29)	72	77	86	88	75	82	61	650
	38	49(37)	54(37)	51	66	56	56	30	85	39	486
	49	35	54	57	93	98	85	51	90	69	632
	60	72	99	98	97	107	102	85	90	91	841
SUM		268	454	440	490	560	524	418	528	332	4014
EFF. Δ		.163	.284	.274	.307	.355	.331	.259	.333	.200	-
WT.		.0434	.0417	.0607	.0654	.0729	.0982	.1509	.1970	.2598	1.0000*
WT. EFF.		.0070	.0118	.0166	.0200	.0258	.0325	.0390	.0656	.0519	.2702

* INCLUDES .0100 WT AT 0 RADIUS
Δ REDUCED BY AVERAGE AMBIENT OF 6

Table VI. Integrating Sphere Output - One-Inch Aperture

RING		BB+.56	CC+.50	DD+1.50	FF+.12	GG+.50	HH+.75	JJ	LL	NN	TOTAL
RADIUS		6.04	7.82	10.68	13.00	15.22	17.32	20.26	23.96	27.66	-
AZIMUTH	6	101	109	108	98	110	109	101	97	90	923
	17	89	107	110	93	111	109	95	98	90	902
	28	72(29)	90(29)	86	89	94	97	85	87	79	779
	38	65(37)	81(37)	82	82	81	87	52	90	72	692
	49	70	99	97	102	103	105	75	99	92	842
	60	96	105	103	102	110	106	90	100	96	908
SUM		493	591	586	566	609	613	498	571	519	5046
EFF. Δ		.310	.376	.373	.359	.388	.391	.313	.362	.327	-
WT.		.0434	.0417	.0607	.0654	.0729	.0982	.1509	.1970	.2598	1.0000*
WT. EFF.		.0134	.0156	.0226	.0234	.0282	.0383	.0472	.0713	.0849	.3449

* INCLUDES .0100 WT AT 0 RADIUS
Δ REDUCED BY AVERAGE AMBIENT OF 6

Table VII. Integrating Sphere Output with Collimator Misaligned - Four-Inch Aperture

RADIAL ERROR-DEG.	0	0	0	0	0	+0.5	-0.5	+1.0	-1.0
TANGENTIAL ERROR-DEG.	0	+0.5	-0.5	+1.0	-1.0	0	0	0	0
AZIMUTH NUMBER									
6	96	96	100	93	94	105	99	104	93
17	101	103	102	98	95	109	101	111	96
28	94	102	88	102	85	101	98	101	94
38	90	95	93	98	92	89	97	92	97
49	98	101	107	102	102	97	108	96	108
60	100	101	112	91	109	106	108	102	104
AVERAGE	579	598	602	584	577	607	611	606	592
AVERAGE (+AND-)	96.5	100		96.75		101.5		99.83	
AVERAGE LESS AMBIENT	88.5	92		88.75		93.5		91.83	

Table VIII. Integrating Sphere Output with Collimator Misaligned - Three-Inch Aperture

RADIAL ERROR-DEG.	0	0	0	0	0	+0.5	-0.5	+1.0	-1.0
TANGENTIAL ERROR-DEG.	0	+0.5	-0.5	+1.0	-1.0	0	0	0	0
AZIMUTH NUMBER									
6	93	93	97	91	88	102	97	101	90
17	98	100	99	95	91	106	98	102	92
28	92	98	84	97	82	97	95	93	92
38	87	92	88	95	86	82	93	82	90
49	94	97	103	95	97	97	104	92	104
60	97	97	108	87	97	103	103	98	84
AVERAGE	561	577	579	560	541	587	590	568	552
AVERAGE (+AND-)	93.5	96.33		91.75		98.08		93.33	
AVERAGE LESS AMBIENT	85.5	88.33		83.75		90.08		85.33	

Table IX. Integrating Sphere Output with Collimator Misaligned - Two-Inch Aperture

RADIAL ERROR-DEG.	0	0	0	0	0	+0.5	-0.5	+1.0	-1.0
TANGENTIAL ERROR-DEG.	0	+0.5	-0.5	+1.0	-1.0	0	0	0	0
AZIMUTH NUMBER									
6	88	88	77	82	32	98	85	88	69
17	91	97	92	92	80	83	94	43	83
28	88	92	78	64	76	72	92	42	84
38	80	88	71	87	65	49	87	43	74
49	89	49	99	53	90	74	95	58	91
60	92	56	101	62	44	98	86	95	28
AVERAGE	528	470	518	440	387	474	539	369	429
AVERAGE (+AND-)	88.0	82.33		68.91		84.41		66.5	
AVERAGE LESS AMBIENT	80.0	74.33		60.91		76.41		58.5	

Table X. Integrating Sphere Output with Collimator Misaligned - One-Inch Aperture

RADIAL ERROR-DEG.	0	0	0	0	0	+0.5	-0.5	+1.0	-1.0
TANGENTIAL ERROR-DEG.	0	+0.5	-0.5	+1.0	-1.0	0	0	0	0
AZIMUTH NUMBER									
6	70	44	28	13	10	76	32	33	18
17	47	78	15	78	12	27	67	11	37
28	71	36	37	15	17	39	62	11	29
38	38	65	12	40	13	22	38	12	22
49	74	11	91	10	53	33	23	15	29
60	68	17	53	17	12	68	27	44	12
AVERAGE	368	251	236	173	117	265	249	126	147
AVERAGE (+AND-)	61.3	40.58		24.16		42.83		22.75	
AVERAGE LESS AMBIENT	53.3	32.58		16.16		34.83		14.75	

D. CONCENTRATOR TEST RESULTS

The concentrator test data taken with the collimator aligned was reduced by summing the readings on the six azimuths, correcting for ambient light, and dividing by the reading of the unreflected beam. The result obtained was an overall efficiency of each ring at the various apertures. These figures are tabulated below the data in Tables III through VI. Each ring was then weighted according to the fraction of the cone area it represented. A weighted over-all efficiency was then obtained for each aperture, as tabulated in the data tables. Over-all efficiency was then divided into reflective efficiency by taking the geometric efficiency as 100 percent for the largest (four-inch) aperture. The reflective efficiency thus obtained was 35.4 percent. The geometric efficiencies calculated are shown in Table XI.

Geometric efficiency was plotted against normalized aperture area (the reciprocal of area concentration ratio). The slope of this curve gives the flux distribution normalized by the reflected incident flux, or flux concentration ratio with the reflectance factor omitted. The plot of geometric efficiency and the flux distribution are shown in Figure 19. Solar rays will cause the flux profile to spread only slightly as compared to the image size obtained with the collimator. The collimator has a deviation from parallel up to 9.5 minutes compared to 16 minutes for the sun.

Table XI. Geometric Efficiency

APERTURE	1	2	3	4
Normalized Area	0.000278	0.00111	0.00250	0.00444
Weighted Eff	0.1046	0.2702	0.3449	0.3537
Geometric Eff	0.2957	0.7639	0.9751	1.0000

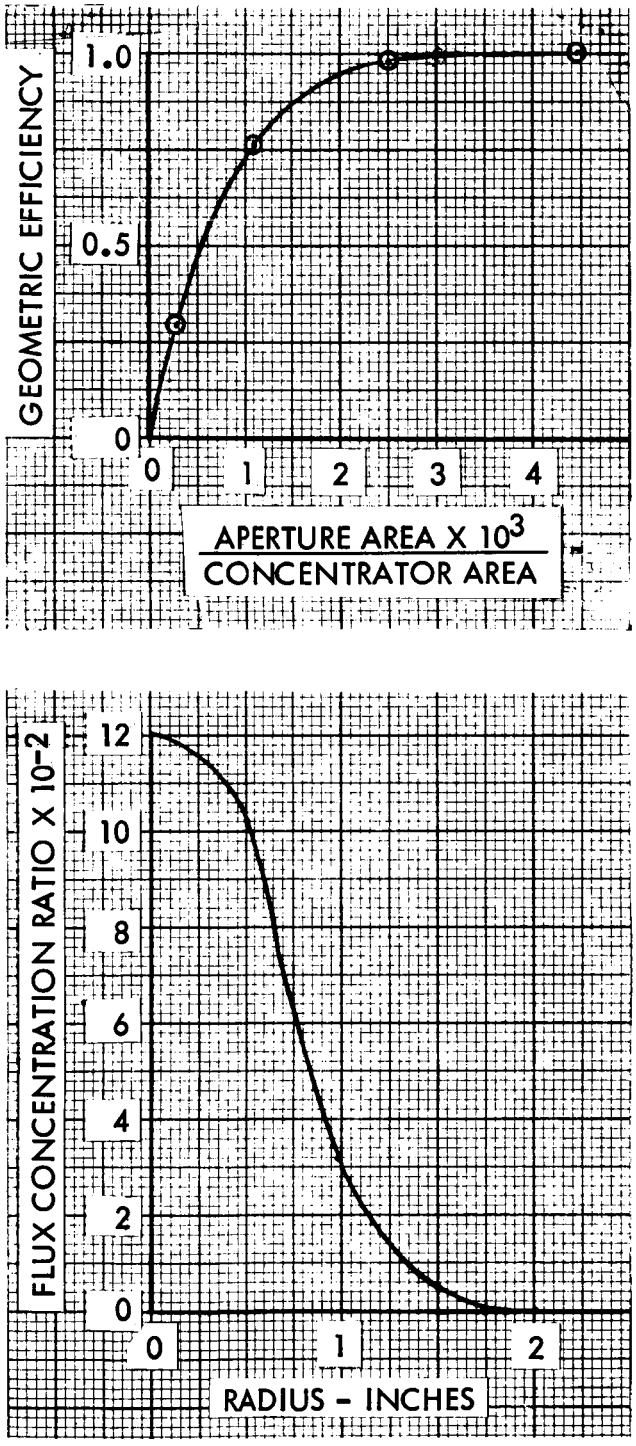

Figure 19. Test Concentrator Performance Using Collimated Light

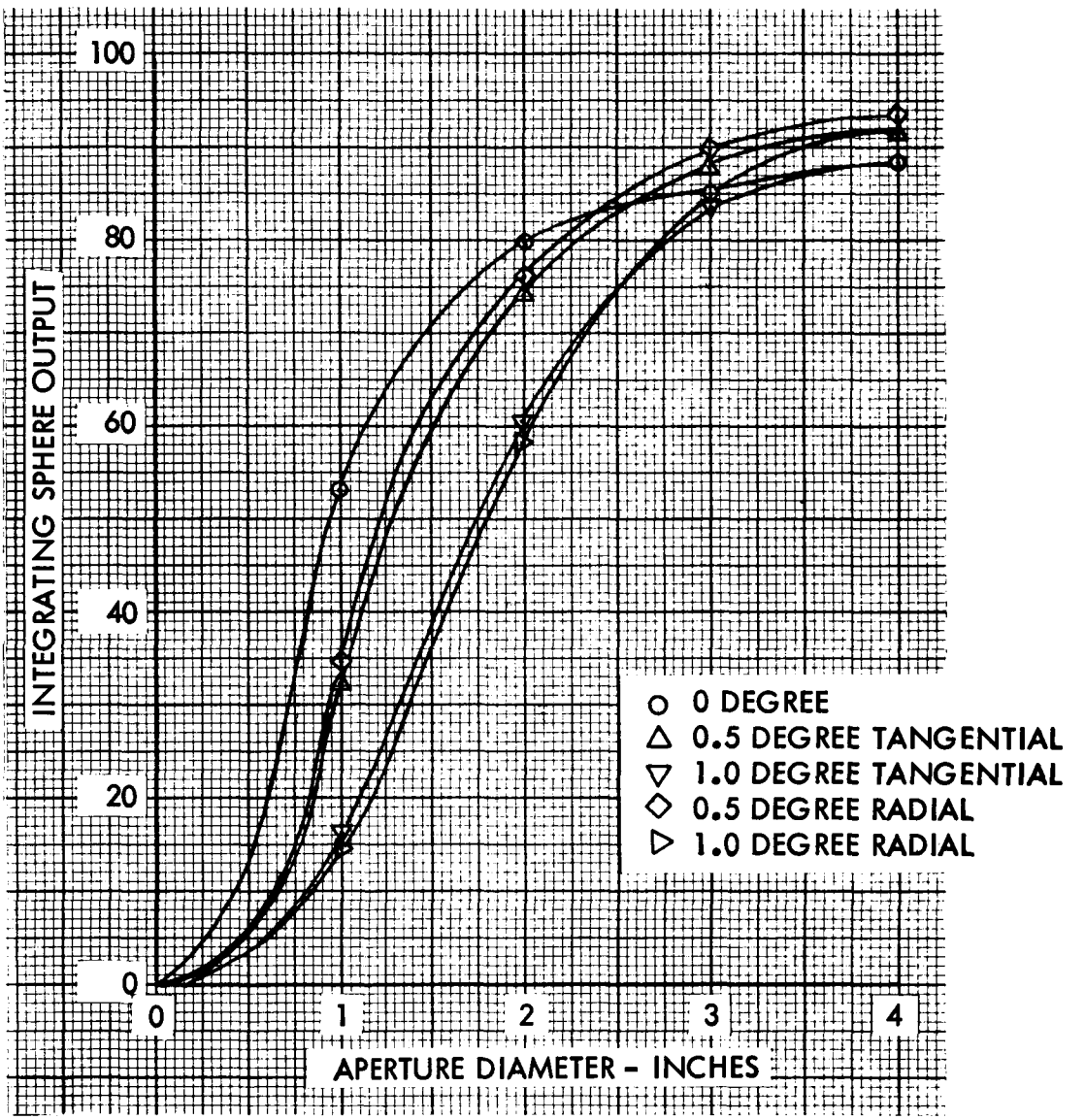

Figure 20. Integrating Sphere Output versus Aperture Diameter

In order to ascertain the effects of misorientation, integrating sphere output was plotted against aperture diameter as shown in Figure 20. These plots show that misorientation causes a uniform shift of the curves proportional to the orientation error. This uniformity of curve shift demonstrates that there is no adverse effect on performance due to the rays striking the column off-center.

SECTION VI. COMPUTER ANALYSIS

A. OPTICAL MODEL

For the computer analysis, a mathematical optical model of the concentrating system was required. The optical model consisted of the following:

(1) The sun at a distance of 1 A. U.
(2) A conical reflector with its axis common to the concentrator axis
(3) A column reflector with its axis common to the concentrator axis
(4) A focal plane

Equations are programmed on the computer to determine the path of any ray coming from the sun and striking the concentrator. The computer equations determine the coordinates of the point of intersection of the ray with the focal plane.

The sun is divided into 1000 equal sectors. Each sector is divided into 1000 segments of equal radiating power.

A two-axis orientation system is assumed. The limits of orientation error are input parameters. An equal probability is assigned to all possible values of the orientation error in each direction.

The cone is divided into 1000 sectors. Each sector is divided into 1000 segments of equal area.

The incident ray is defined as the line connecting the point of origin in the sun with the first point of incidence on the concentrator.

The point of origin is determined by first selecting at random the coordinates of the center of the sun with respect to the concentrator axis. A segment of the sun

is then selected at random. The coordinates of the center of this segment are then the coordinates of the point of origin of the ray.

The first point of incidence is taken as the center of a segment of the cone selected at random.

The surface of the cone is assumed to have slope errors that are normally distributed about a mean of zero. The ratio of the slope error to the standard deviation is obtained by selecting at random the cumulative probability that the slope error is less than a particular error and finding the corresponding particular error. This ratio is then multiplied by the cosine and sine of a random angle to obtain the tangential and radial components of the ratio. Multiplication by selected standard deviations then gives the tangential and radial components of the surface slope error.

The column is divided into sections of equal length, each of which may be assigned a nominal diameter. Along the length of the column are parabolic steps of a height that is negligible with respect to the column diameter. All the parabolic steps focus on the image of the concentrator focal point in the conical mirror.

The surface of the column, like the surface of the cone, is assumed to have slope errors that are normally distributed about a mean of zero. The radial and tangential components of the slope errors are determined by the same procedure used for the cone slope errors.

The focal plane is a plane that is perpendicular to the concentrator axis and that passes through the concentrator focal point.

B. COMPUTER PROGRAM

The computer program describes the optical model in mathematical terms. Each "run" on the computer is the trace of a ray from its origin, the sun, through the three reflections within the concentrator, to termination at the focal plane.

The equal power subdivisions of the solar disk are obtained from the known distribution of intensity in the solar disk (Reference 8).

The program allows the selection of the maximum orientation error along each of two orthogonal axes as well as a fixed orientation error.

The cone is described by its apex half-angle, θ, its outside radius, R_O, and the inside-to-outside radius ratio, C_R. The program permits the selection of the tangential and radial components of the standard deviation of cone surface slope error.

The program also permits the selection of the number of column sections to be used and the assignment of a nominal diameter to each section. The components of the standard deviation of column slope error are also inputs to the program.

The ray reflected from the column strikes the cone with its surface errors, and is finally reflected toward the focal plane. The focal plane is at a predetermined distance from the apex. The program allows the user to consider any plane at or near the focal plane through the use of the variable ΔS.

The outputs of the program are d, distance from the focal point to the point where the ray strikes the focal plane; d/R_O, a measure of concentrator performance; and Γ_4, the azimuth of the point from one of the orientation axes. Intermediate printouts, which include all angles derived during the course of the ray tracing, can be called for if desired.

Primarily, the equations define the optical principle of equal angles of incidence and reflection, and utilize the geometric and trigonometric functions necessary to obtain these angles at each reflective surface. The one place within the program in which other fields of mathematics are involved is in determining the second point of incidence, i.e., the point where the ray strikes the column. This is actually the solution of three simultaneous equations, and is achieved by an

iterative process. The number of iterations is limited. If this limit is reached, the program is stopped and the above mentioned intermediary print-outs can be called to determine the cause of the problem. Also, if the ray is determined to have missed the column entirely, the computer prints out this fact and the distance by which the ray missed, then goes on to the next ray.

C. COMPUTER EQUATIONS

1. Selection of Variables

The complexity of the equations and the large number of variables dictated the computer evaluation. Equations for the distribution of the individual variables were derived so that, through the use of random numbers, a statistical estimate of concentrator performance could be computed rapidly and economically.

The parameters that have a distribution of values and the methods of selection are defined by the equations in the following paragraphs. Refer to Section X for the list of symbols and definitions.

The azimuth (F) and zenith distance (H) of the origin of the ray in the solar disk are obtained from the following relations: $0^{o} \leqslant F < 360^{o}$, selected at random, and $H = 16r$ minutes of arc, where the variable r takes into account the distribution of solar energy across the solar disk and is defined by

$$r^2 = 1 - K_S\left(\frac{1.035 + 0.2552\sqrt{K_S}}{0.5246 + 0.7656\sqrt{K_S}}\right),$$

where

$0 \leqslant K_S \leqslant 1$, selected at random.

The azimuth of the first point of incidence, Γ_1, is obtained from

$0^{o} \leqslant \Gamma_1 < 360^{o}$, selected at random.

The azimuth, Γ_0, and zenith distance, Γ_S, of the center of the sun are obtained from

$$\Gamma_0 = \arctan \frac{Y}{X}$$

and

$$\Gamma_S = \sqrt{X^2 + Y^2},$$

where X and Y are determined from $X = C_x (X_{max}) + X_c$ and $Y = C_y (Y_{max})$, with $-1 < C_x < 1$ and $-1 < C_y < 1$ selected at random, X_{max} and Y_{max} to be specified, and X_c also specified (to provide for the possibility of a fixed orientation error).

The azimuth of the sun with respect to the azimuth of the first point of incidence is then $\Gamma_A = \Gamma_0 - \Gamma_1$.

The mirror surface errors were assumed to be normally distributed. A close approximation (Reference 1) of the normal probability integral was used, and the radial and tangential components of the slope angles were determined as follows (the value of σ to be given in each case):

At the first point of incidence,

$$\bar{\theta}_r = (X_{\bar{\theta}}) (\sigma_{\bar{\theta}_r}) (\cos \Upsilon_1)$$

and

$$\bar{\theta}_t = (X_{\bar{\theta}}) (\sigma_{\bar{\theta}_t}) (\sin \Upsilon_1),$$

where

$$0^o \leq \Upsilon_1 < 360^o, \text{ selected at random}$$

and

$$X_{\bar{\theta}} = G - \frac{2.515517 + 0.802853G + 0.10328G^2}{1 + 1.432788G + 0.189269G^2 + 0.001308G^3},$$

where $G = \sqrt{-2 \ln P_1}$ $(0 < P_1 < 1$, selected at random)*.

At the second point of incidence,

$$\bar{\alpha}_r = (X_{\bar{\alpha}})\ (\sigma_{\bar{\alpha}_r})\ (\cos \tau_2)$$

and

$$\bar{\alpha}_t = (X_{\bar{\alpha}})\ (\sigma_{\bar{\alpha}_t})\ (\sin\ \tau_2),$$

where

$$0^o \leqslant \tau_2 < 360^o, \text{ selected at random}$$

and

$$X_{\bar{\alpha}} = L - \frac{2.515517 + 0.802853L + 0.10328L^2}{1 + 1.432788L + 0.189269L^2 + 0.001308L^3},$$

where $L = \sqrt{-2 \ln P_2}$ $(0 < P_2 < 1$, selected at random)*.

At the third point of incidence,

$$\bar{\bar{\theta}}_r = (X_{\bar{\bar{\theta}}})\ (\sigma_{\bar{\bar{\theta}}_r})\ (\cos \tau_3)$$

and

$$\bar{\bar{\theta}}_t = (X_{\bar{\bar{\theta}}})\ (\sigma_{\bar{\bar{\theta}}_t})\ (\sin \tau_3),$$

where

$$0^o \leqslant \tau_3 < 360^o, \text{ selected at random}$$

and

$$X_{\bar{\bar{\theta}}} = U - \frac{2.515517 + 0.802853U + 0.10328U^2}{1 + 1.432788U + 0.189269U^2 + 0.001308U^3},$$

where $U = \sqrt{-2 \ln P_3}$ $(0 < P_3 < 1$, selected at random)*.

*Actually, $X_{\bar{\theta}} = f(P_1)$ for $0 \leqslant P_1 \leqslant 0.5$: for $0.5 < P_1 \leqslant 1$, $X_{\bar{\theta}} = -f(1-P_1)$. The same holds true for $X_{\bar{\alpha}}$ and $X_{\bar{\bar{\theta}}}$.

With inputs of C_R, R_o, j, and the ratios

$$\frac{p(1)}{R_o}, \frac{p(2)}{p(1)}, \frac{p(3)}{p(1)}, \ldots \frac{p(k)}{p(1)}, \ldots \frac{p(j)}{p(1)},$$ the concentrator radius, R_I, and column radius, p(k), associated with the ray being traced are selected as follows:

$$R_i = C_R R_o$$

$$(R_i)^2 \leqslant (R_I)^2 \leqslant (R_o)^2 ; \ (R_I)^2 \text{ selected at random, } R_I = \sqrt{(R_I)^2}$$

$$k = \left[1 + j \frac{R_o - R_I}{R_o - R_i}\right]_{\text{truncated}*} \ (k \geqslant 1; \ k_{max} = j).$$

2. Derivation of Equations

The initial reference point for the error equations was taken as the first point of incidence, with the error ray striking that point with incoming angular components of γ_r and γ_t. These angles are functions of the orientation errors (Γ_S, Γ_A) and the origin determinants (F and H). The ray is traced through the system with radial and tangential slope errors ($\bar{\theta}_r$, $\bar{\theta}_t$, $\bar{\alpha}_r$, $\bar{\alpha}_t$, $\bar{\bar{\theta}}_r$, and $\bar{\bar{\theta}}_t$) assumed at each of the three reflections. The optical analysis is based on the distribution of d, the distance from the focal point, and the intersection of the error ray with the focal plane. The symbols used in the analysis are defined in Section X (List of Symbols).

The purpose of the analysis was to compute the theoretical efficiency of the concentrator. By choosing appropriate variables for orientation errors and cone and column surface errors, a distribution of miss distances is obtained, and from this and the energy distribution of the sun's rays a concentration ratio is generated as an estimate of system efficiency.

The error ray deviates initially from the ideal ray because of misorientation and

*"Truncated" means that the quantity is rounded down to integer; i.e., any fraction is dropped.

is also dependent upon the position of its origin on the solar disk. The angular deviation γ, and its components γ_r and γ_t are derived as follows (see Figure 21):

$$\tan \Gamma_P = -\cos F \tan H$$

$$\tan \gamma_V = \sin F \tan H \cos \Gamma_P$$

$$\tan \Gamma_V = \tan \gamma_V \csc (\Gamma_S + \Gamma_P)$$

$$\tan \gamma = \sqrt{\tan^2 (\Gamma_S + \Gamma_P) \tan^2 \gamma_V + \tan^2 (\Gamma_S + \Gamma_P) + \tan^2 \gamma_V} \quad . \qquad (1)$$

$$\tan \gamma_r = -\cos (\Gamma_A + \Gamma_V) \tan \gamma \qquad (2)$$

$$\tan \gamma_t = -\sin (\Gamma_A + \Gamma_V) \tan \gamma \qquad (3)$$

This incident ray, striking the cone at a concentrator radius $R = R_I$ with an error of γ, is reflected towards the column with angular components, in the horizontal and vertical planes, of Δ and A_2, respectively. The angles (τ) of incidence and reflection are made by the ray with the normal to the cone. This normal deviates from the design normal by surface slope errors $\bar{\theta}_r$ and $\bar{\theta}_t$. Δ and A_2 are derived as follows (see Figure 22):

$$\tan \quad = \frac{\tan \bar{\theta}_t \sec \theta \cot (\theta + \bar{\theta}_r) + \tan \gamma_t}{\cot (\theta + \bar{\theta}_r) - \tan \gamma_r}$$

$$\tan \delta = \tan \bar{\theta}_t \sec \theta$$

$$\tan \phi = \sec \delta \cot (\theta + \bar{\theta}_r)$$

$$\tan \Omega = \sin (\lambda - \delta) \sec \lambda \tan \phi$$

$$\tan \upsilon = \tan \delta \cos (\theta + \bar{\theta}_r)$$

$$\cos \zeta = \frac{\cos^2 \delta \sec^2 \lambda + \csc^2 \phi - \cot^2 \phi \sec^2 \Omega}{2 \cos \delta \sec \lambda \csc \phi}$$

$$\eta = (\tan \phi \cos \delta - \tan \gamma_r) \sec \lambda$$

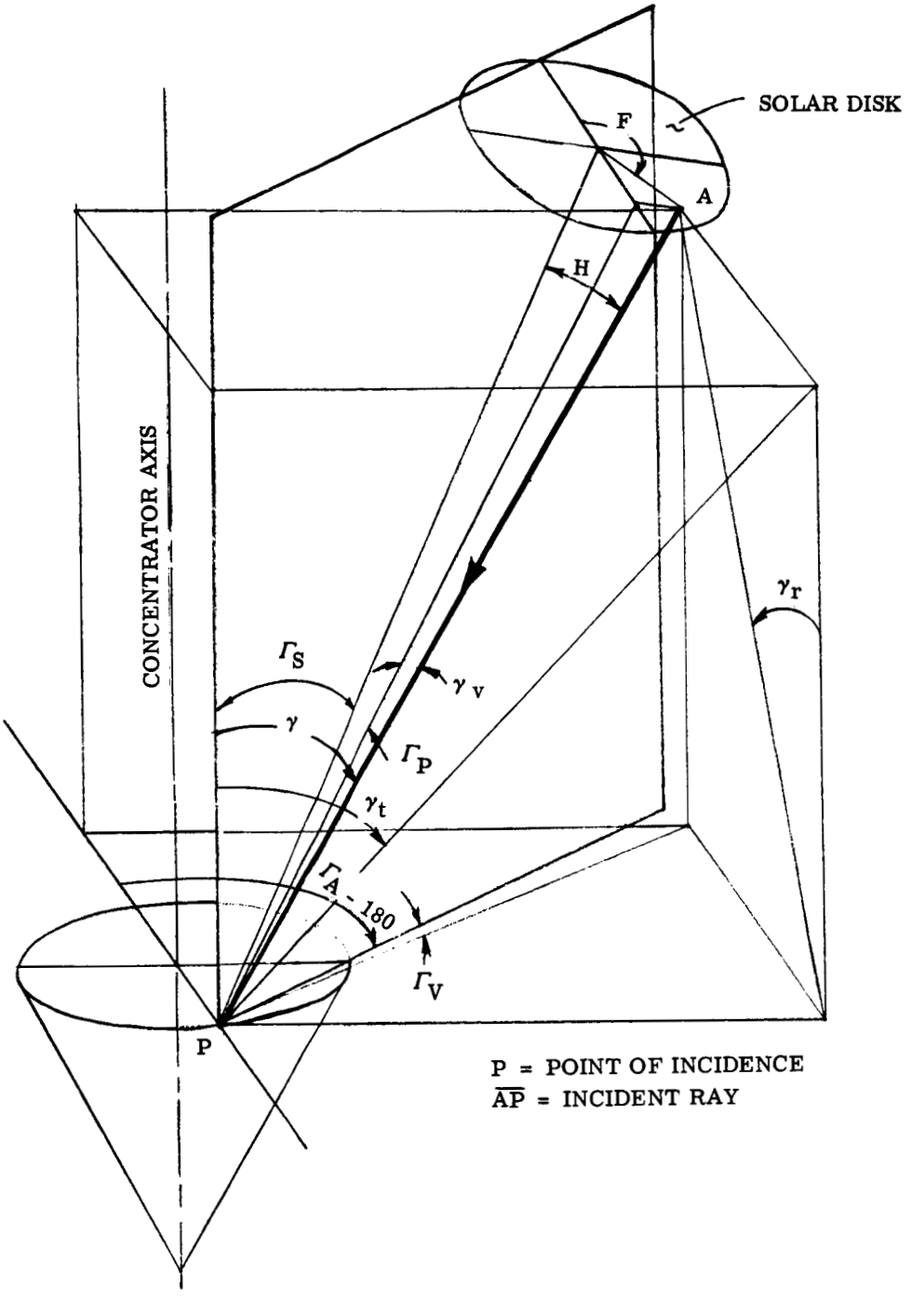

Figure 21. Incident Ray

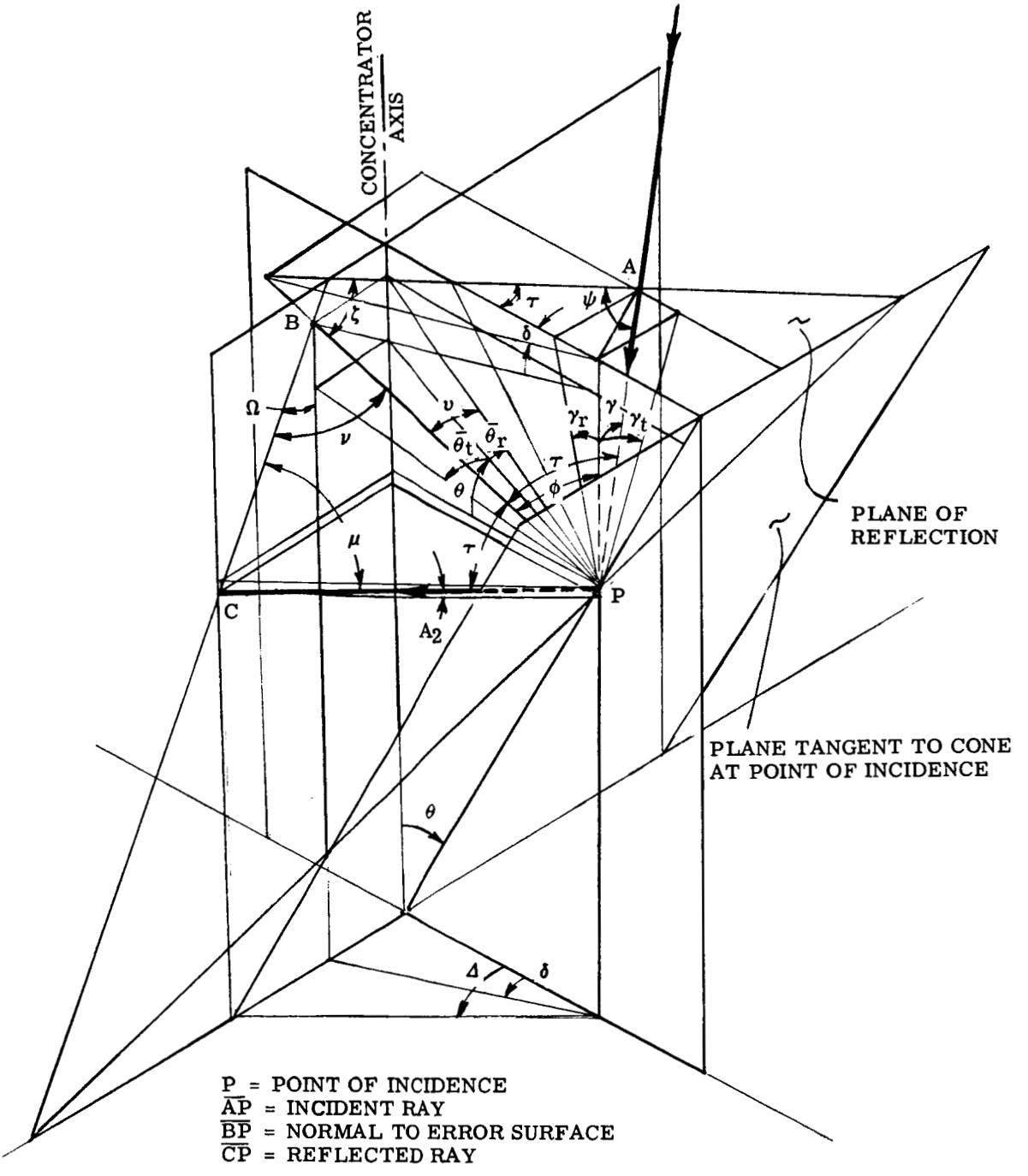

Figure 22. First Reflection

$$\cos \psi = \frac{\eta^2 + \sec^2 \gamma - \sec^2 \phi}{2 \eta \sec \gamma}$$

$$\tau = 180 - (\zeta + \psi)$$

$$\cos \nu = \frac{\csc^2 \phi + \cot^2 \phi \sec^2 \Omega - \cos^2 \delta \sec^2 \lambda}{2 \csc \phi \cot \phi \sec \Omega}$$

$$\mu = 180 - (\tau + \nu).$$

Hence

$$\Delta = \arctan \left[\sin \Omega \sec \upsilon \sec (\theta + \bar{\theta}_r) \sin \tau \csc \mu + \tan \delta \right], \quad (4)$$

and

$$A_2 = \arctan \left(\frac{\sec \phi \sin \tau \cos \Omega \csc \mu - 1}{\tan \phi \cos \delta \sec \Delta} \right). \quad (5)$$

The ray thus reflected toward the column strikes it at a point determined by three surfaces: (1) the column surface, which is a paraboloid; (2) the vertical plane through the reflected ray; and (3) the plane which is perpendicular to the vertical plane and which also contains the reflected ray (see Figure 23).

The equation of the vertical plane is

$$x + y \tan \Delta + R_I \tan \Delta = 0. \quad (6)$$

The equation of the inclined plane is determined from three conditions:

(1) The plane is perpendicular to the plane of Equation 6.

(2) The plane contains the point $(0, -R_I, R_I \cot \theta)$ of incidence on the cone.

(3) The plane makes an angle A_2 with the horizontal plane ($z = 0$).

Satisfying these three conditions simultaneously results in the equation:

$$x \tan \Delta - y - z \sec \Delta \cot A_2 - R_I (1 - \sec \Delta \cot A_2 \cot \theta) = 0. \quad (7)$$

The equation for the column surface is obtained by determining the equation of the

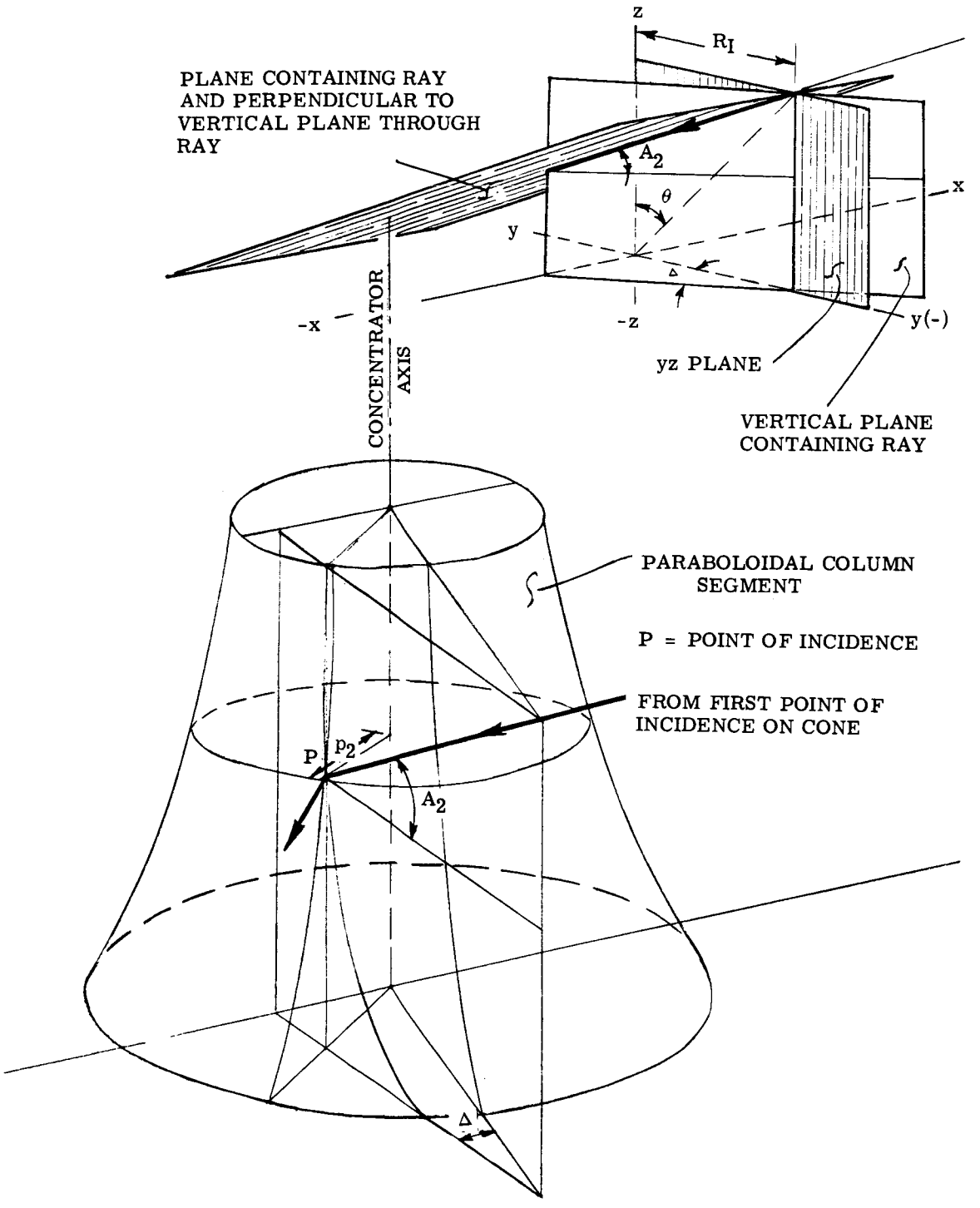

Figure 23. Second Point of Incidence

parabolic segment (see Figure 24) with respect to mirrored axes, rotating the axes, and finally revolving this curve about the concentrator axis.

Let the mirror image of the concentrator axis be the y^1 axis, and point on this axis V (o, ℓ) be the vertex for the parabola. The equation of the parabola is then

$$x'^2 = 4a\,(y' - \ell) \tag{8}$$

where $a = (S - \ell)$, S being the distance from the origin to the focus.

A known point, Q, on this curve has the coordinates

$$x'_Q = -R_I \text{ and } y'_Q = \frac{R_I \cos 2\theta + p(k)}{\sin 2\theta} .$$

Solving for ℓ and substituting values of Q (x'_Q, y'_Q), the value of ℓ is determined to be

$$\ell^* = \left\{S + R_I \cot 2\theta + p(k) \csc 2\theta - \sqrt{R_I^2 \csc^2 2\theta + [S - p(k) \csc 2\theta]\,[S - p(k) \csc 2\theta - 2R_I \cot 2\theta]}\right\} \div 2. \tag{9}$$

Rotating the axes through an angle 2θ by the equations

$$x' = x \cos 2\theta - z \sin 2\theta$$

$$y' = x \sin 2\theta + z \cos 2\theta,$$

and then revolving about the z axis so that $x = \sqrt{x^2 + y^2}$, Equation 8 becomes the equation of the paraboloid:

*Actually, there are two roots to the equation. However, the root involving the positive radical is incompatible with the design. Therefore, only the negative radical is valid.

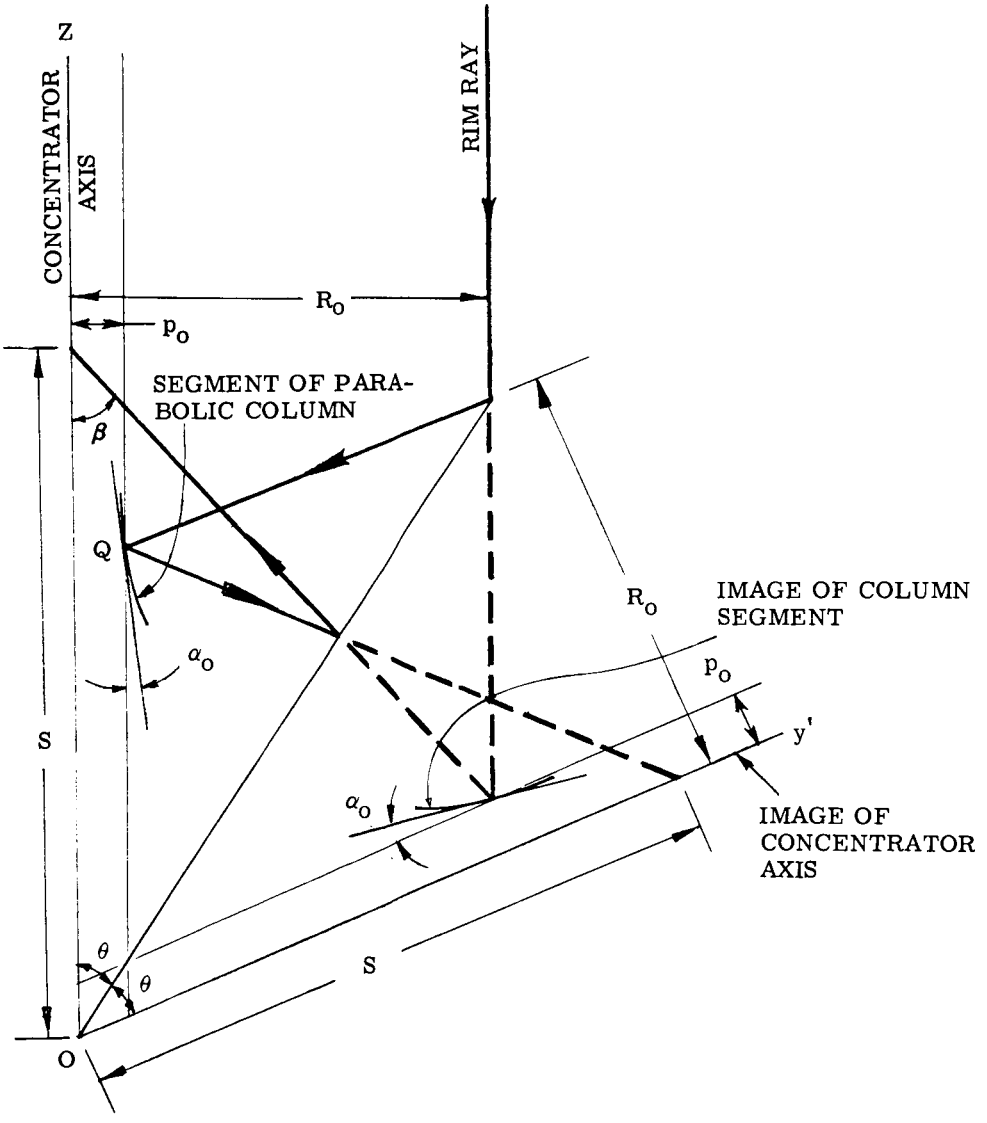

Figure 24. Cone-Column Geometry

$$\left[\left(\sqrt{x^2 + y^2}\right)\cos 2\theta - z \sin 2\theta\right]^2 - 4\left[S - \ell\right]$$

$$\left[\left(\sqrt{x^2 + y^2}\right)\sin 2\theta + z \cos 2\theta\right] + 4\ell\left[S - \ell\right] = 0. \qquad (10)$$

Simultaneous solution of Equations 6, 7, and 10 will give the coordinates of the point P_2 (x_2, y_2, z_2) of incidence upon the column. From these coordinates can be determined the column radius at that point,

$$p_2 = \sqrt{x_2^2 + y_2^2} \; . \qquad (11)$$

Having the coordinates of P_2, we can now derive the angles ξ, β, and α_2 (see Figure 25):

$$\xi = (\xi + \Delta) - \Delta, \text{ where } \xi + \Delta = \arcsin\left[\frac{R_I}{p_2}\sin\Delta\right] \qquad (12)$$

$$\beta = \arctan\left[\frac{z_2 \sin 2\theta - p_2 \cos 2\theta}{S - z_2 \cos 2\theta - p_2 \sin 2\theta}\right] \qquad (13)$$

$$\alpha_2 = 90 - 2\theta - \frac{\beta}{2} \; . \qquad (14)$$

The ray striking the column at point P_2 is reflected back toward the cone with angular components, in the horizontal and vertical planes, of K and C, respectively. The angles (χ) of incidence and reflection are made by the ray and the normal to the column. This normal deviates from the design normal by surface slope errors $\bar{\alpha}_r$ and $\bar{\alpha}_t$. K and C are derived as follows (see Figure 26).

$$\tan\chi = \tan\bar{\alpha}_t \sec\bar{\alpha}_2$$

$$\tan m = \frac{\tan A_2 \sec(\xi + \Delta) - \tan(\alpha_2 + \bar{\alpha}_r)}{\tan(\xi + \Delta) - \tan\chi}$$

$$\tan\omega = \tan\bar{\alpha}_t \sec\alpha_2 \cos(\alpha_2 + \bar{\alpha}_r)$$

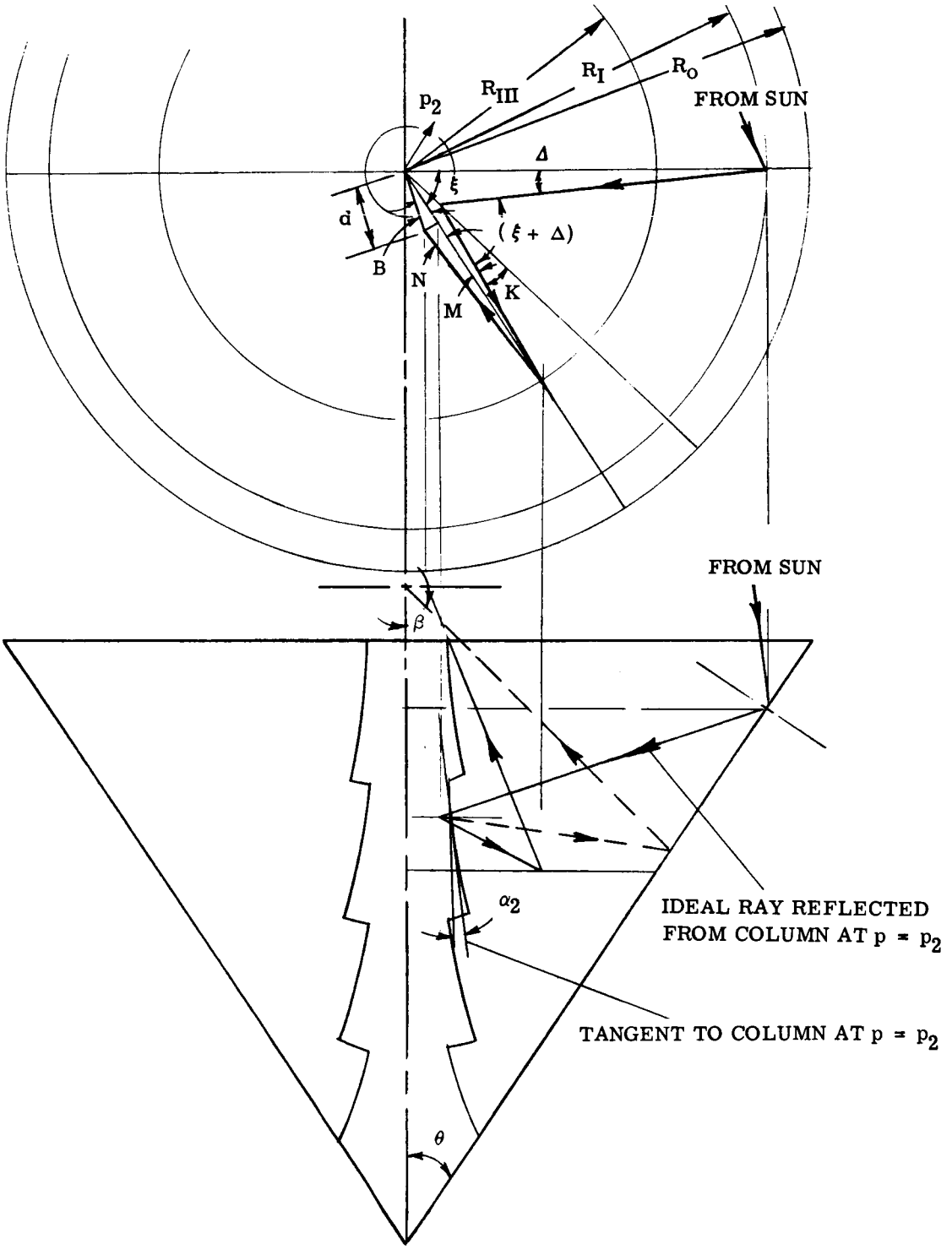

Figure 25. Plan Views

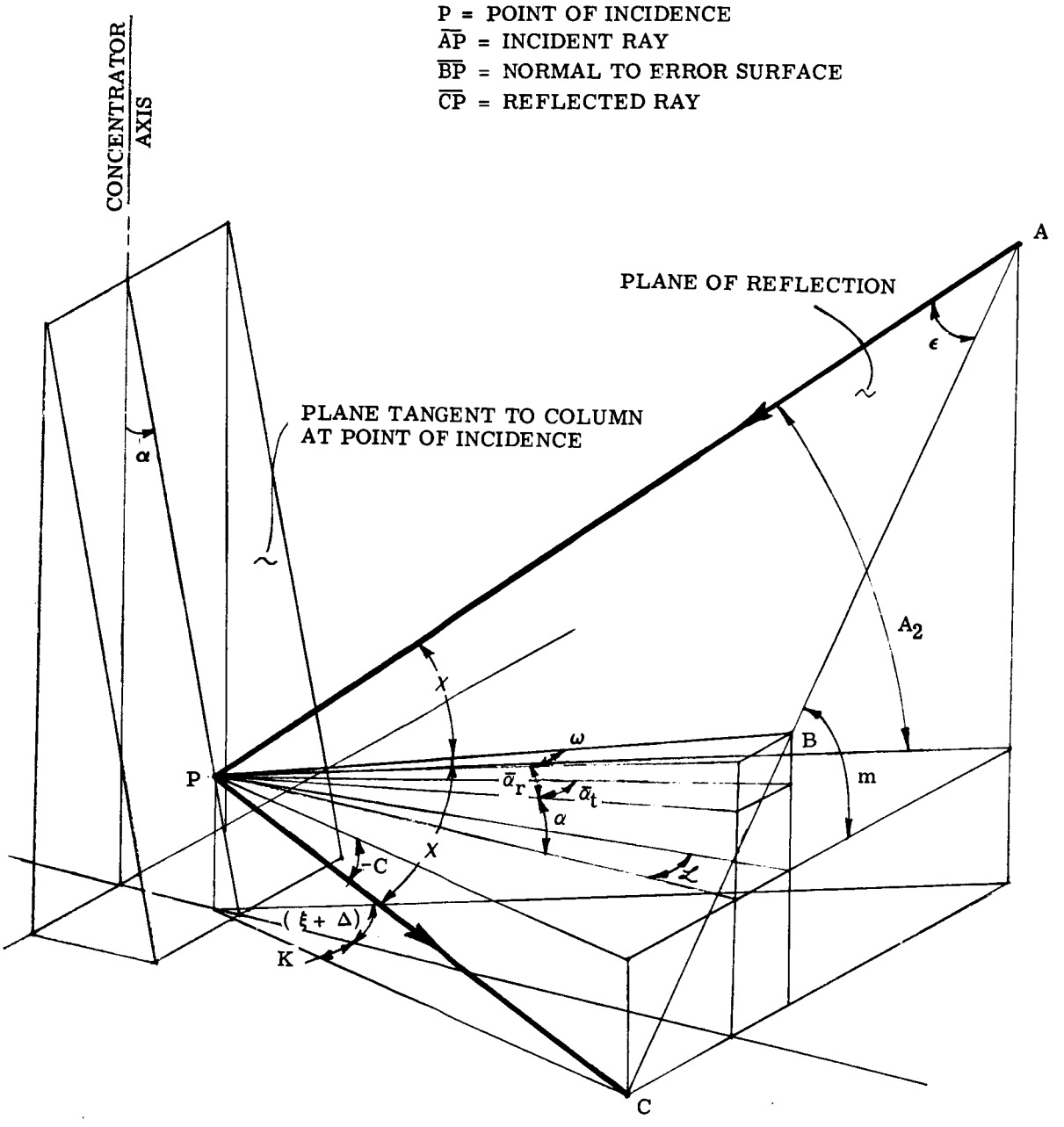

Figure 26. Second Reflection

$$\cos\chi = \{\sec^2 A_2 \sec^2(\xi + \Delta) + \sec^2\omega \sec^2(\alpha_2 + \bar{\alpha}_r) - [\tan(\xi + \Delta) - \tan\mathcal{L}]^2 \sec^2 m\} \div \{2 \sec A_2 \sec(\xi + \Delta) \sec\omega \sec(\alpha_2 + \bar{\alpha}_r)\}$$

$$\sin\epsilon = \frac{\sec\omega \sec(\alpha_2 + \bar{\alpha}_r) \sin\chi \cos m}{\tan(\xi + \Delta) - \tan\mathcal{L}}$$

$$K = \arctan\left[\frac{\cos m \sec A_2 \sin 2\chi \sec(\xi + \Delta)}{\sin(2\chi + \epsilon)} - \tan(\xi + \Delta)\right] \quad (15)$$

$$C = \arctan\left[\frac{\tan A_2 \sec(\xi + \Delta) - \tan m\{\tan(\xi + \Delta) + \tan K\}}{\sec K}\right]. \quad (16)$$

The ray ρ_{II} thus reflected back toward the cone, strikes it at a point P_3 (x_3, y_3, z_3). A vertical plane through ρ_{II} intersects the cone in a hyperbola. Simultaneous equations of the hyperbola and ρ_{II} will yield the coordinates x_3, z_3.

The equation of the hyperbola is determined from the equations of the cone and the vertical plane through ρ_{II} (see Figure 27):

$$\begin{aligned} &\text{(Cone)} && x^2 + y^2 = z^2 \tan^2\theta \\ &\text{(Plane)} && y = p_2 \sin K \\ &\text{(Hyperbola)} && x^2 + {p_2}^2 \sin^2 K = z^2 \tan^2\theta. \end{aligned} \quad (17)$$

The equation of ρ_{II} is derived from points R (x_R, z_R) and T (x_T, z_T):

$$x = z \cot C + x_R$$

$$x_R = -z_T \cot C + x_T,$$

where $z_T = R_I \cot\theta - \tan A_2 \sec\Delta (R_I - p_2 \cos\xi)$ and $x_T = p_2 \cos K$,

$$x = z \cot C - K_1 \cot C + p_2 \cos K \quad (18)$$

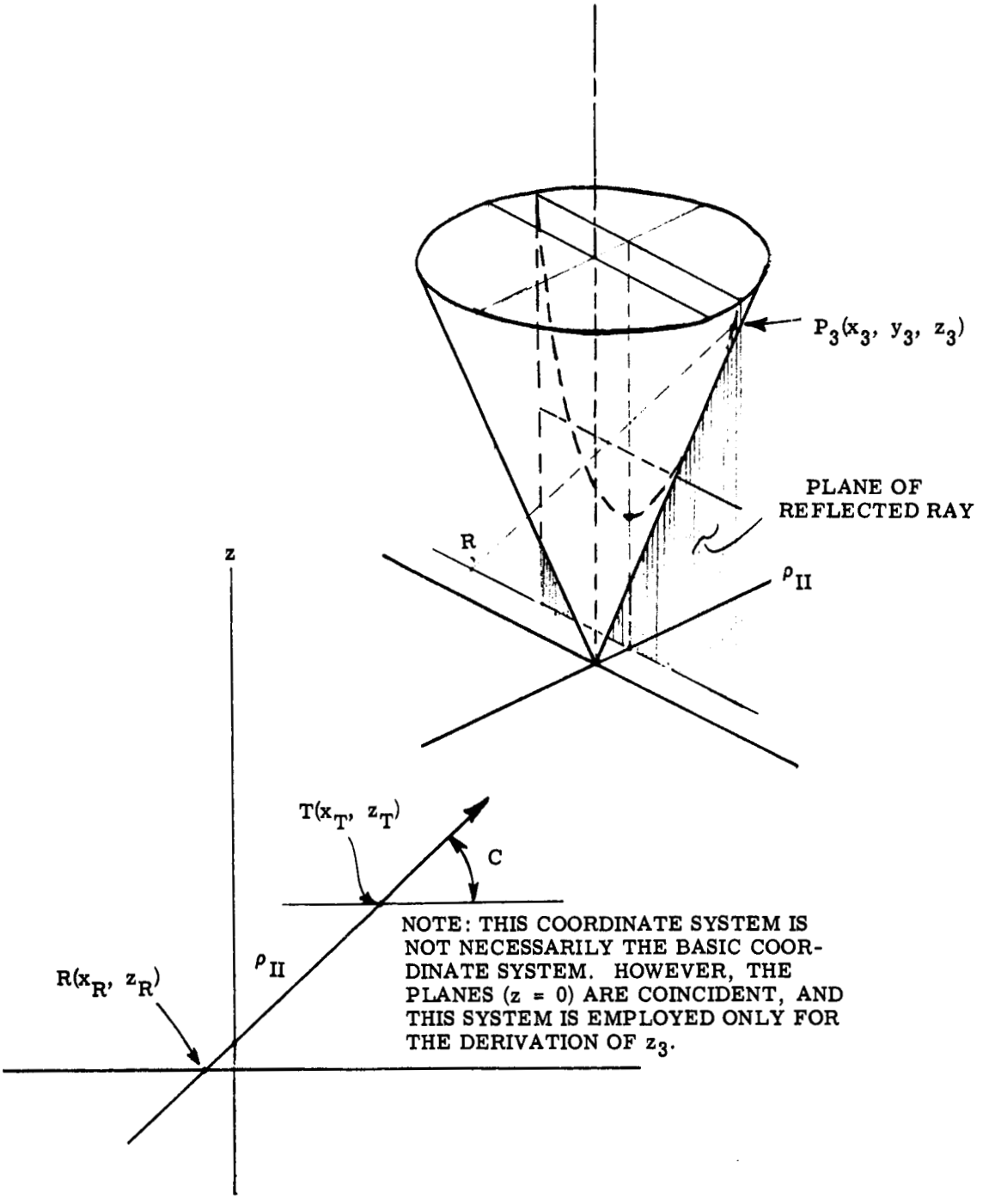

Figure 27. Third Point of Incidence

where

$$K_1 = R_I \cot\theta - \tan A_2 \left[(R_I - p_2 \cos\xi) \sec\Delta \right]. \quad (19)$$

With the above substitution, simultaneous solution of Equations 17 and 18 yields the z coordinate of P_3:

$$z_3 = \Big(K_1 - p_2 \tan C \cos K + \tan C \tan\theta \sqrt{K_1^2 - p_2^2 \sin^2 K \cot^2\theta + p_2^2 \tan^2 C - 2p_2 K_1 \tan C \cos K}\Big) \div (1 - \tan^2 C \tan^2\theta). \quad (20)$$

Referring again to Figure 25, the following relationships are derived:

$$R_{III} = z_3 \tan\theta \quad (21)$$

and

$$\sin M = \frac{p_2}{R_{III}} \sin K. \quad (22)$$

The ray striking the cone at point P_3 is reflected toward the focal plane with angular components, in the horizontal and vertical planes, of N and D respectively. The angles (V) of incidence and reflection are made by the ray and the normal to the cone. This normal deviates from the design normal by surface slope errors $\bar{\bar{\theta}}_r$ and $\bar{\bar{\theta}}_t$. N and D are derived as follows (see Figure 28):

$$\tan W = \frac{\tan(\bar{\theta} + \bar{\bar{\theta}}_r) + \tan C \sec M}{\tan\theta_t \sec\theta + \tan M},$$

$$\cos\Sigma = \Big[\sec^2 M \sec^2 C + \sec^2 W (\tan\bar{\bar{\theta}}_t \sec\theta + \tan M)^2 - \sec^2(\theta + \bar{\bar{\theta}}_r) - \tan^2\bar{\bar{\theta}}_t \sec^2\theta\Big] \div \Big[2 \sec M \sec C \sec W (\tan\bar{\bar{\theta}}_t \sec\theta + \tan M)\Big],$$

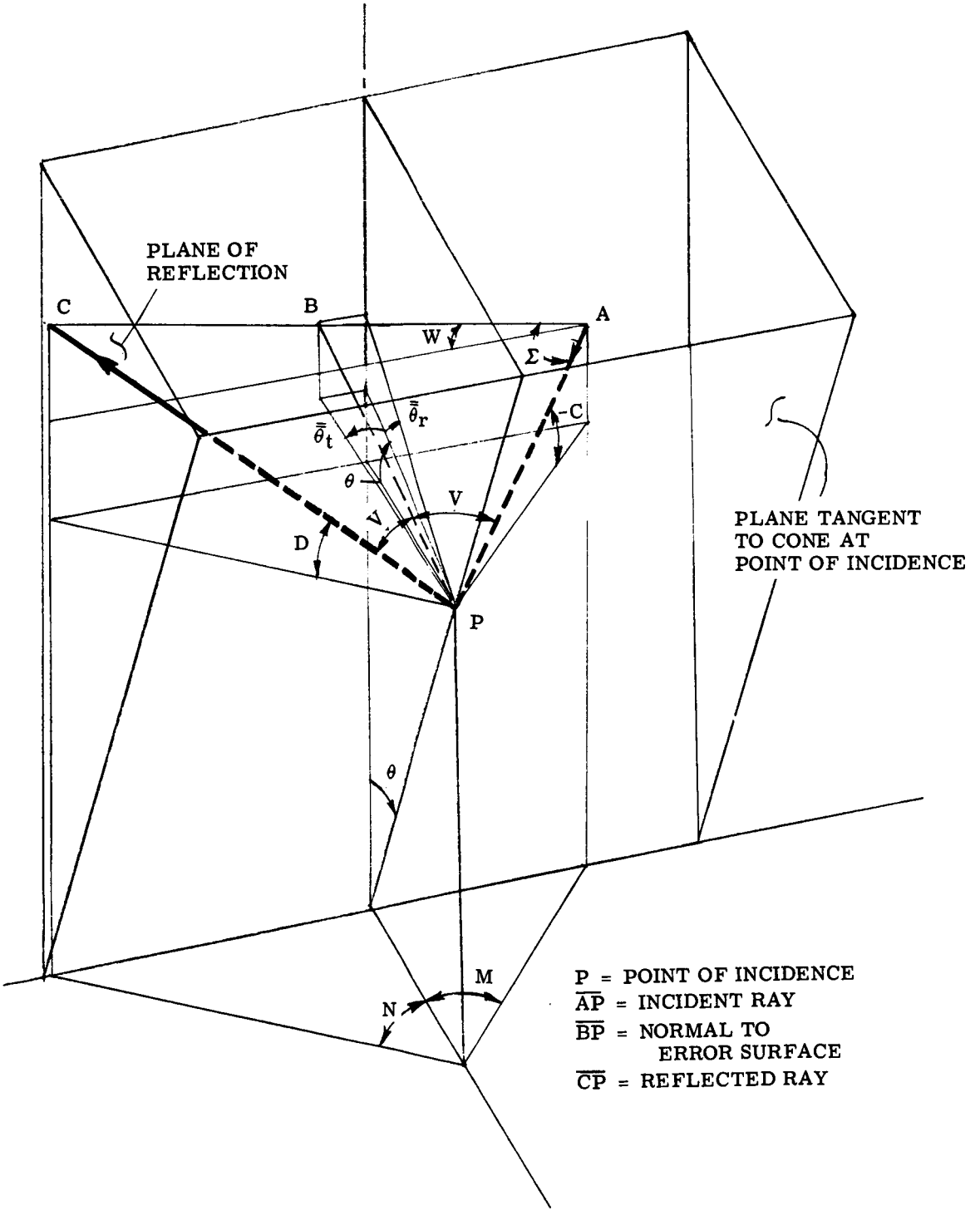

Figure 28. Third Reflection

$$\sin V = \frac{\sin \Sigma \sec W \, (\tan \bar{\bar{\theta}}_t \sec \theta + \tan M)}{\sqrt{\sec^2 (\theta + \bar{\bar{\theta}}_r) + \tan^2 \bar{\bar{\theta}}_t \sec^2 \theta}}$$

$$N = \arctan \left[\frac{\cos W \sin 2V \sec C \sec M}{\sin (2V + \Sigma)} - \tan M \right], \tag{23}$$

and

$$D = \arctan \left\{ \cos N \sec M \left[\sec C \sin W \sin 2V \csc (2V + \Sigma) - \tan C \right] \right\}. \tag{24}$$

Referring once more to Figure 25, the resultant focal plane error d is derived as follows:

$$\rho_{III_h} = (S + \Delta S - z_3) \cot D,$$

$$d = \sqrt{(\rho_{III_h} \sin N)^2 + (R_{III} - \rho_{III_h} \cos N)^2}, \tag{25}$$

$$B = \arctan \left(\frac{\rho_{III_h} \sin N}{R_{III} - \rho_{III_h} \cos N} \right),$$

and

$$\Gamma_4 = \xi + K - M + B + \Gamma_1, \tag{26}$$

where Γ_4 is the azimuth of the image with respect to the orientation axis chosen as a reference.

D. COMPUTER DATA

After the equations and the method of selecting variables had been derived, the computer programming was performed and test runs were made. An initial test run was made with a fixed value for each variable so that the computer program and its output could be compared to a manual solution using the same fixed values. This "check-out" run on the computer served to refine the equations so that all the

angles were handled in the proper quadrants and ensured proper programming of the equations.

Once the program was successfully checked, "production" runs were begun. The first production runs were made primarily to determine optimum sample size. It was desirable to keep the number of runs to a minimum without sacrificing confidence in the data. Samples of 25, 50, and 100 rays were analyzed; it was found that significant differences existed at the 25 and 50 levels, but samples of 100 exhibited no significant differences.

Following the determination of sample size, the column size was optimized for the effects of the sun's diameter. For these runs, all errors were held to zero. With a rim angle of 45 degrees and column slope of 0 degree for rim rays, the focal length for each value of rim radius and column radius was established. The model described at the beginning of this section was examined in four sections, with each section representing one quarter of the column. Several typical section radii were examined, including one large radius to serve as a standard.

Cumulative power (a measure of efficiency) was plotted against normalized aperture area (actually the squared ratio of "spot radius" to cone radius) (see Figures 29 through 32).

At the "break-point" of the curves, or that point where efficiency begins to drop off, power loss was measured for each column section radius, then plotted against the normalized column area (see Figure 33). The intersection of the curves through these plots with the horizontal line representing minimum loss provided the optimum normalized column area and thus the optimum radius for that section. The minimum loss was obtained from the large radius column. The large radius, of course, is not practical because of weight and obscuration.

The optimum section radii were found to be approximately in the ratio 1 : 1.16 : 0.84 : 0.482. However, since a section radius must not exceed that of the

sections above it because of shadow effects, the ratio was adjusted to 1 : 1 : 0.725 : 0.415. These ratios take into account the fact that the four sections contribute, respectively from the top to the bottom, 40 , 30, 20, and 10 percent of the total power. These ratios, then, are valid for all future computer runs involving a four section column.

In addition to the sun's diameter, the other errors that have a significant effect on the column sizing are orientation errors and tangential surface errors on the cone. Computer runs were made for these errors singly. Error values (for maximum orientation error and the standard deviation of tangential cone surface errors) were 0, 8, 16, 32, and 64 minutes of arc. Plots of cumulative power versus area (Figures 34 through 37) were used to determine optimum column radii (Figures 38 and 39) in the same manner as was done previously for the sun's diameter. A cross plot (Figure 40) of this data provides a means of determining the optimum column radii for any value of the errors.

In order to determine the relationship with spot size and the individual errors, several runs were made, encompassing the probable range of error values. Plots of cumulative power versus normalized aperture area are shown in Figures 41 through 45. These plots were then used to derive optimum performance, i.e., maximizing power while minimizing spot size. The resulting linear relationships between area and squared error parameters are plotted in Figures 46 through 50.

The final seven evaluation runs were made with typical values for each error. Three runs were made with what was considered the optimum geometric configuration. Errors for these runs were chosen to represent systems of high, average, and low accuracies. The other four runs were made with varying configurations, each with the same errors that were used for the average system above. Geometric parameters varied were apex half-angle and effective rim angle. These in turn caused changes in focal length, initial column slope, and column radii. The

changes were not severe, since a relatively small change of rim angle will shift the focal plane a considerable distance either down (undesirable because of columnar obscuration) or up (undesirable for structural and packaging considerations). The data from these runs are plotted in Figures 51, 52, and 53.

All runs made on the computer are summarized in Table XII.

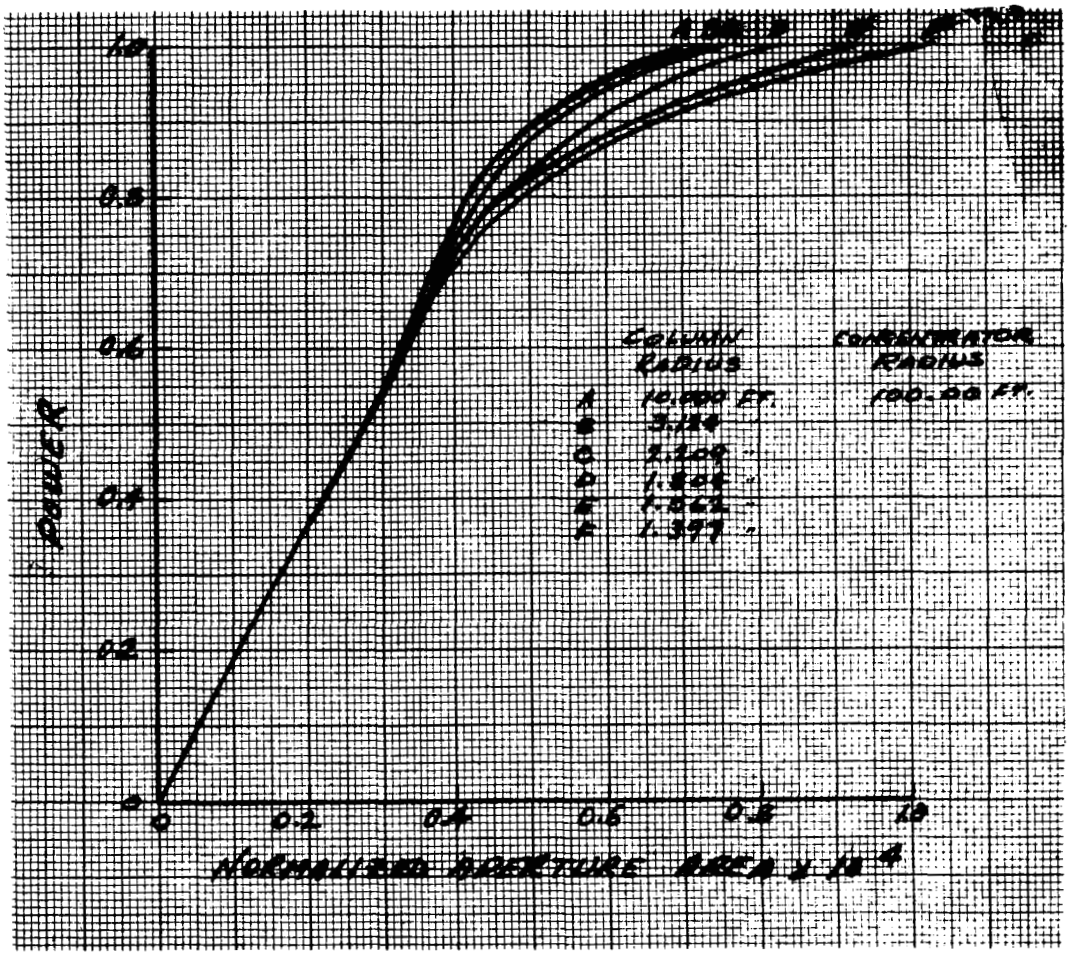

Figure 29. Power versus Area with Concentrator Radius at 100 Ft - Column Section 1

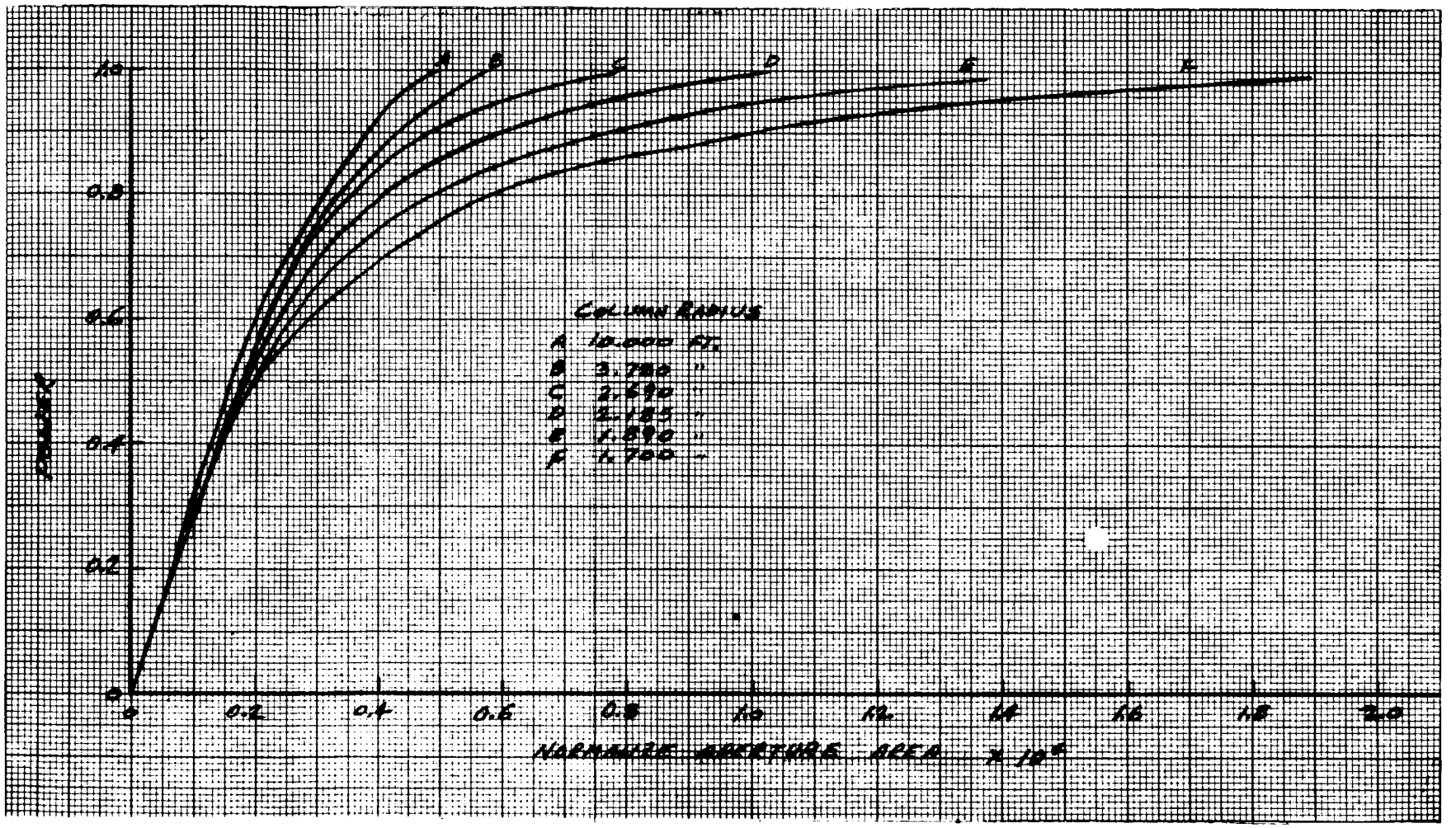

Figure 30. Power versus Area with Concentrator Radius at 100 Ft - Column Section 2

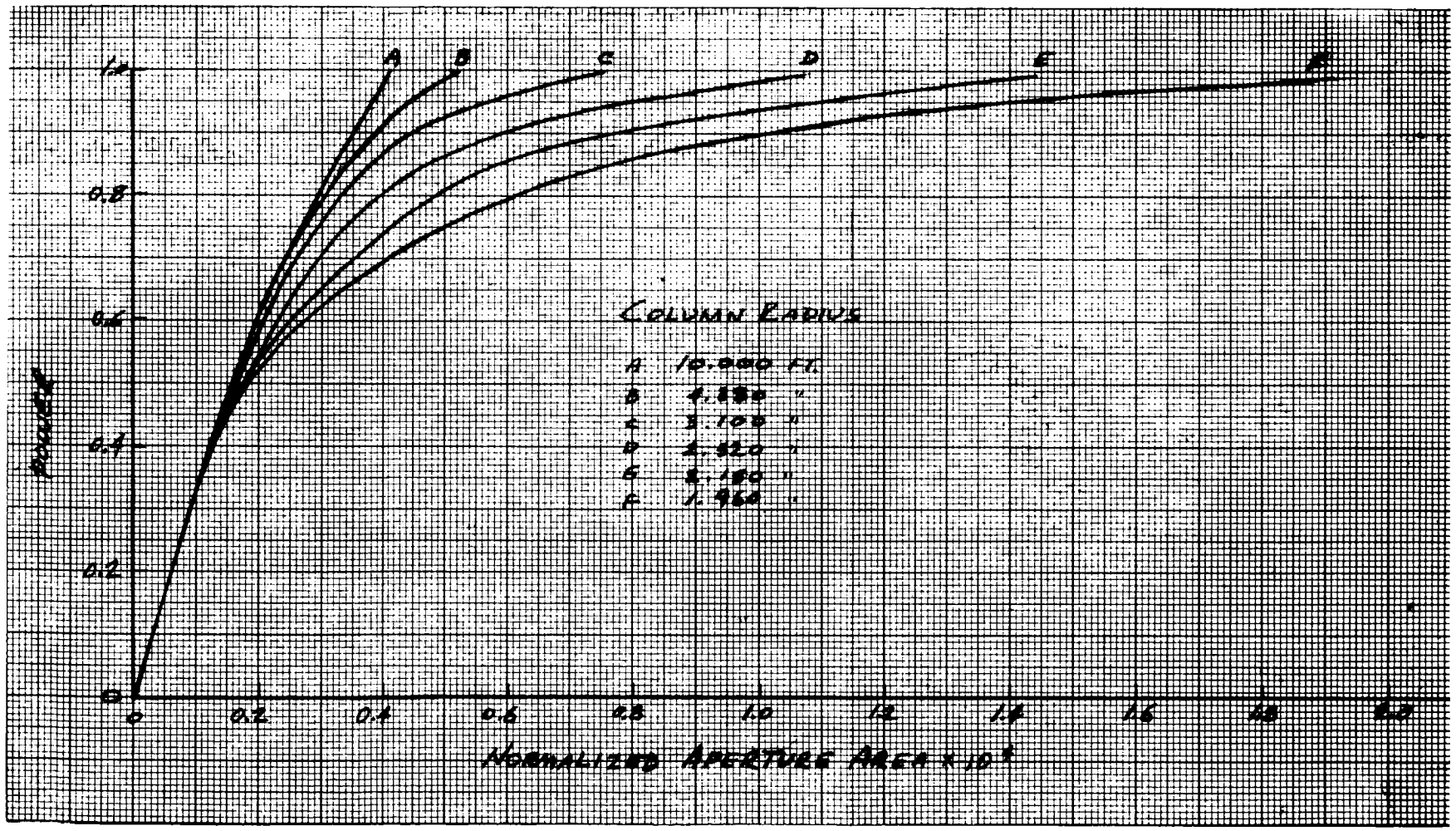

Figure 31. Power versus Area with Concentrator Radius at 100 Ft - Column Section 3

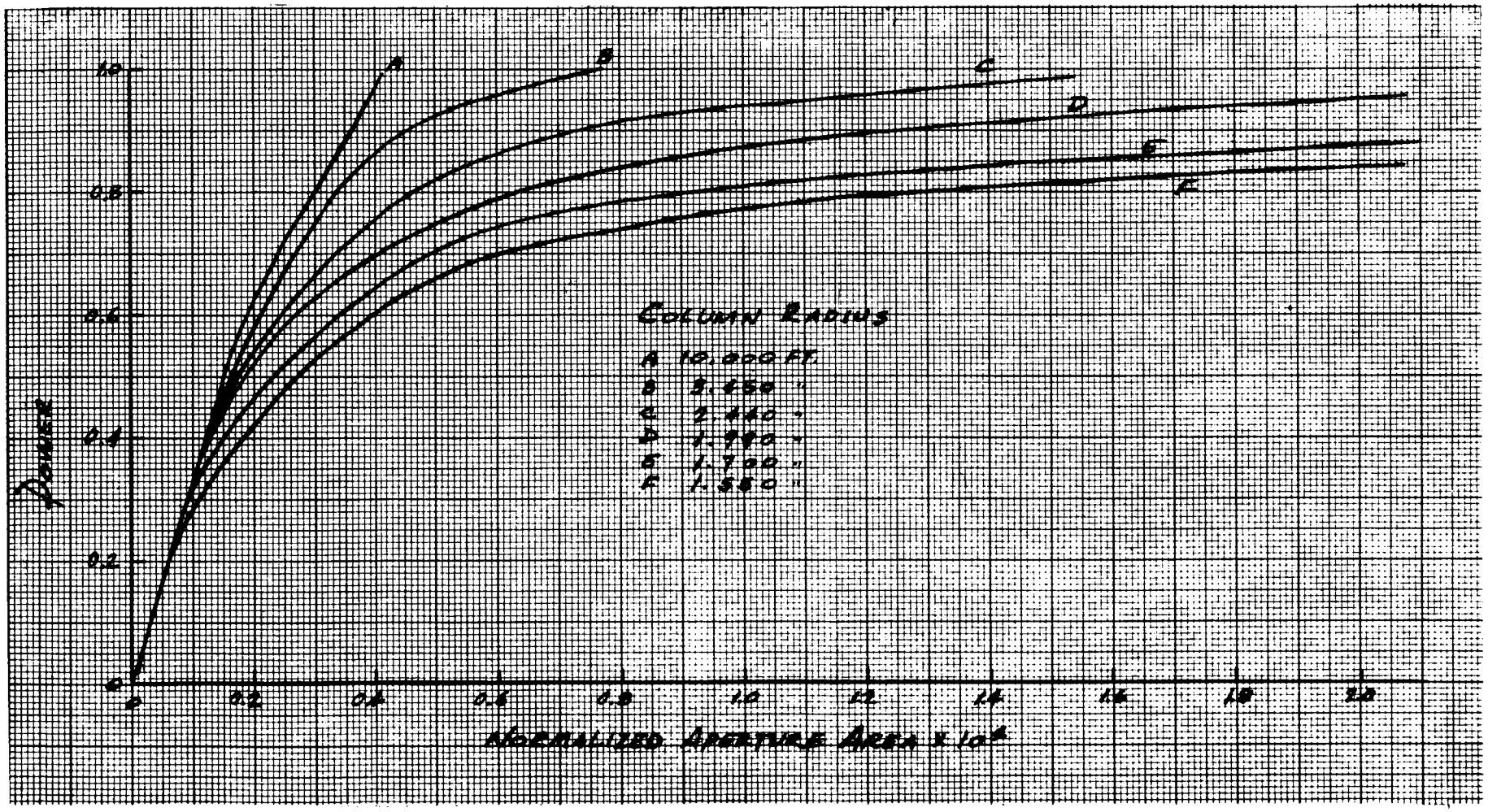

Figure 32. Power versus Area with Concentrator Radius at 100 Ft - Column Section 4

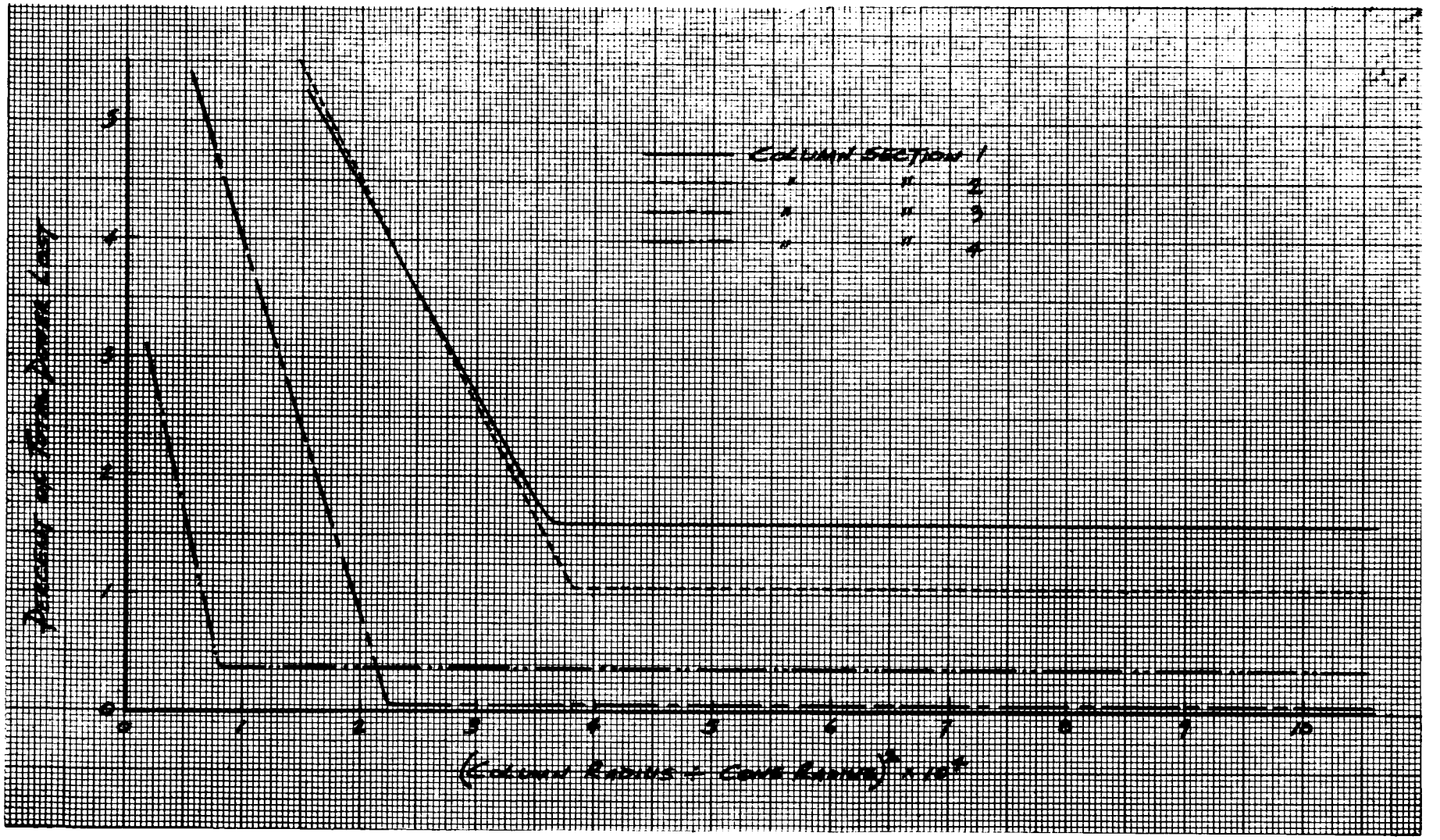

Figure 33. Power Loss versus Ratio of Cross-Sectional Area (Column-to-Cone) at a Normalized Aperture Area of 0.65×10^{-4}

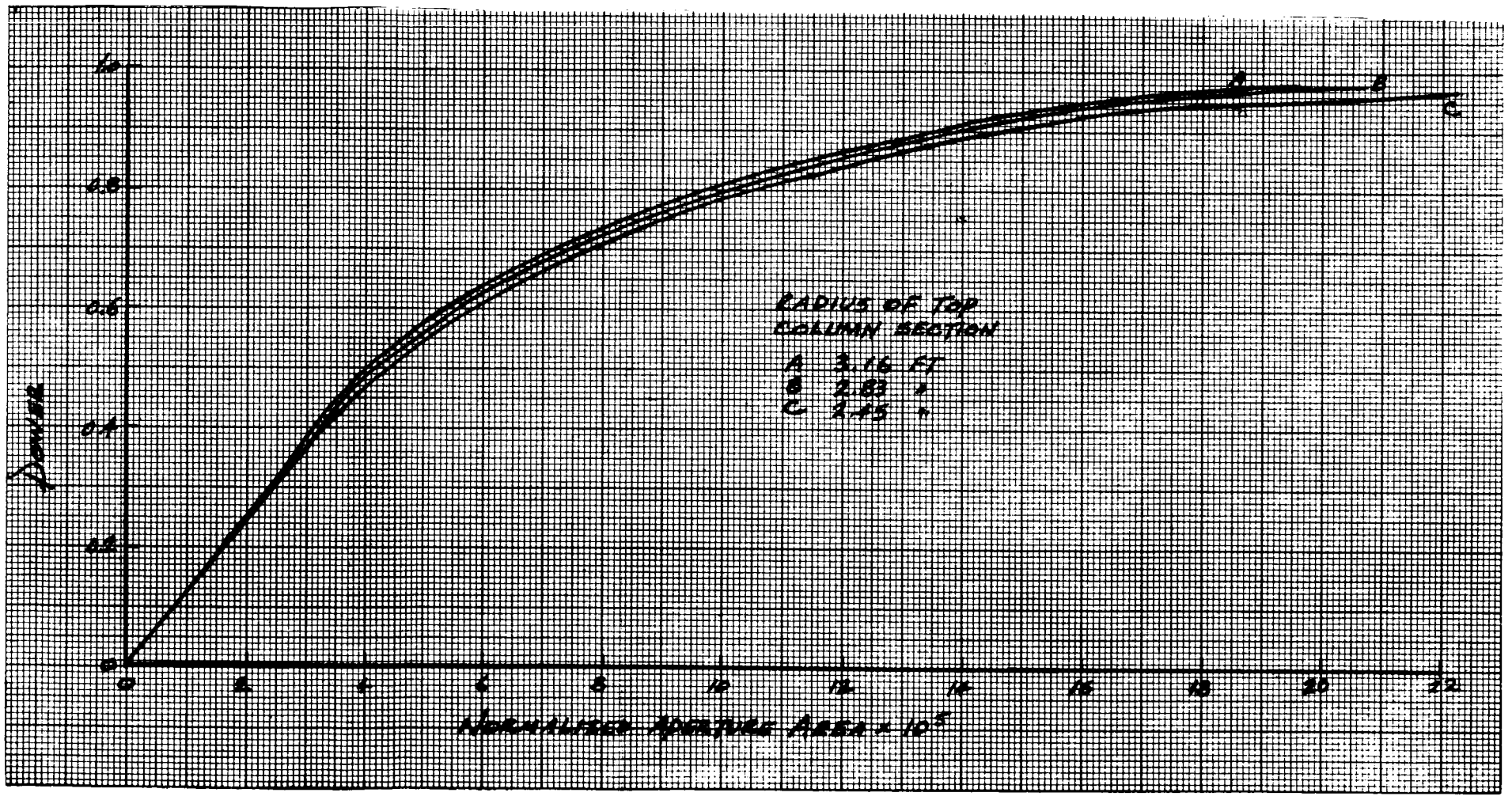

Figure 34. Power versus Area - Maximum Orientation Error, 16 Minutes

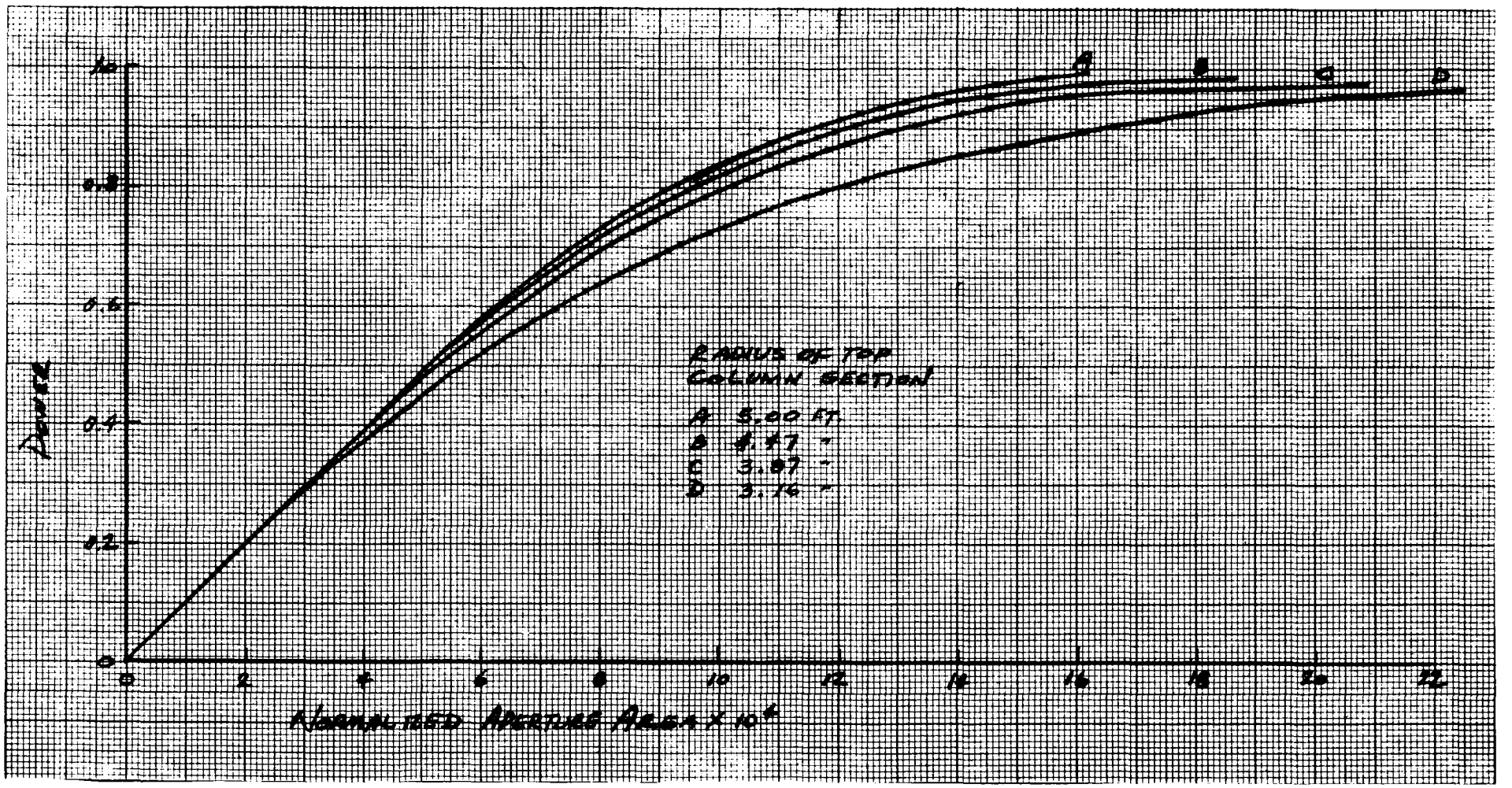

Figure 35. Power versus Area - Maximum Orientation Error, 64 Minutes

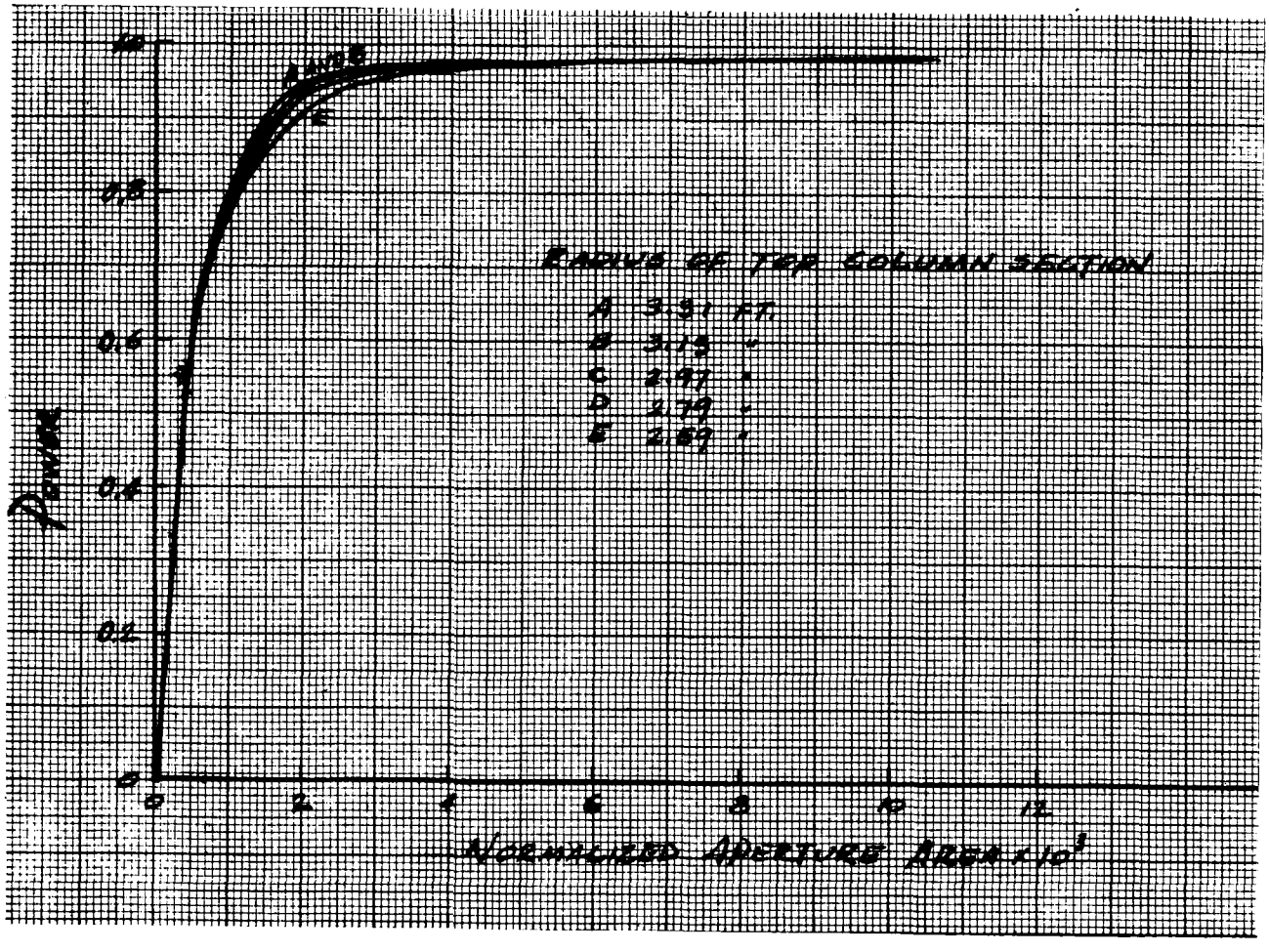

Figure 36. Power versus Area - Standard Deviation of Tangential Cone Surface Errors, 16 Minutes

SECTION VI. COMPUTER ANALYSIS

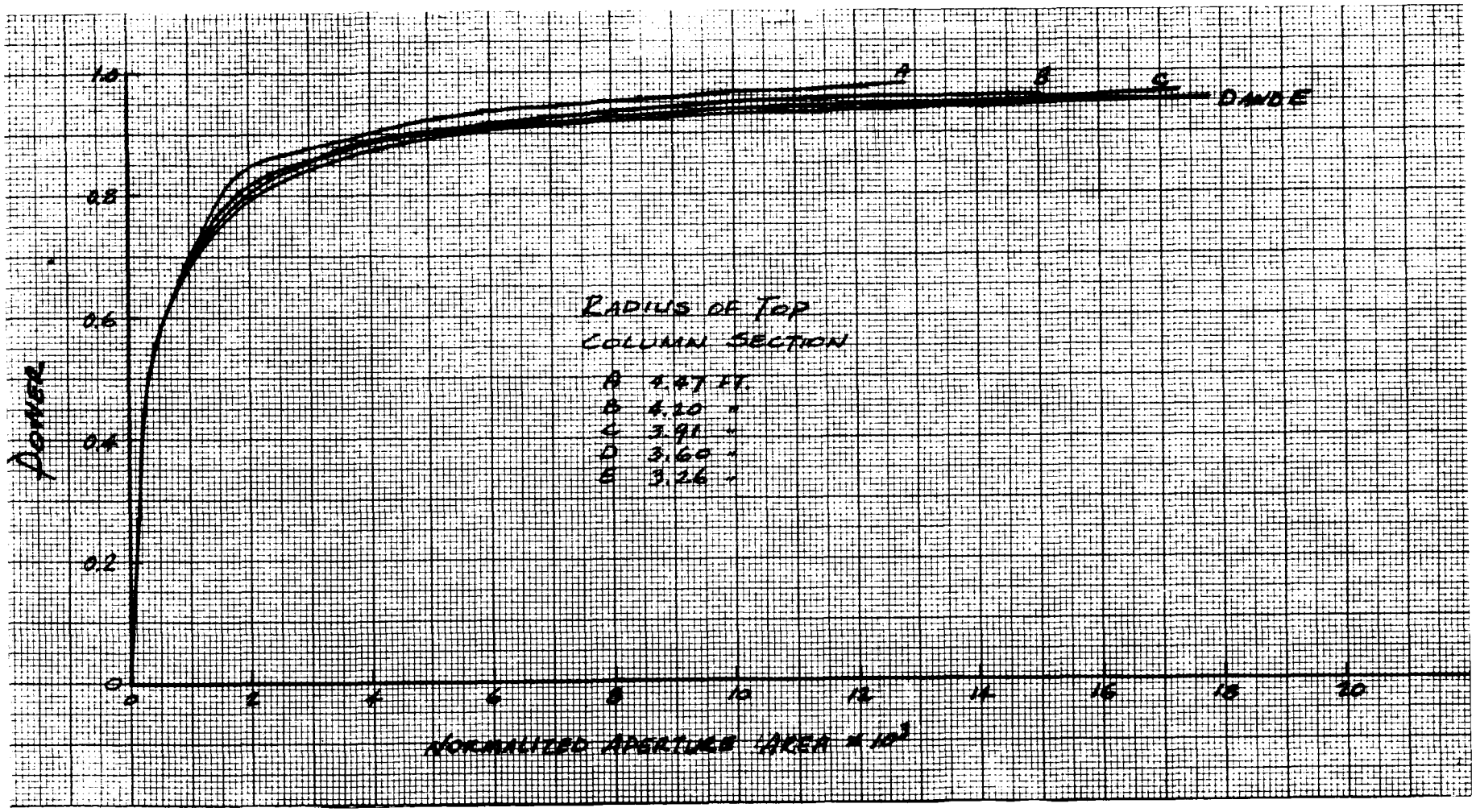

Figure 37. Power versus Area - Standard Deviation of Tangential Cone Surface Errors, 64 Minutes

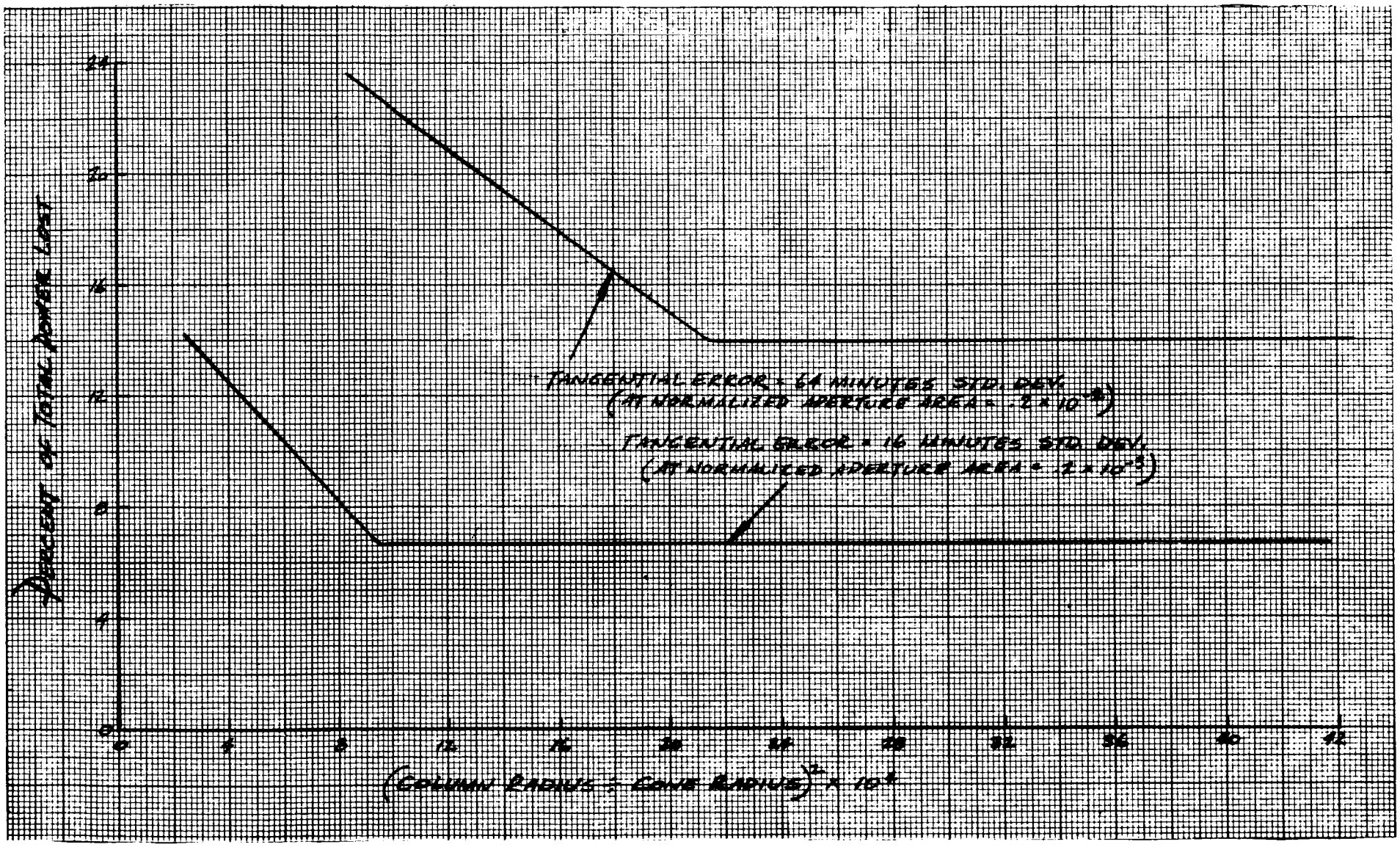

Figure 38. Power Loss versus Ratio of Cross-Sectional Area (Column-to-Cone) - Tangential Error

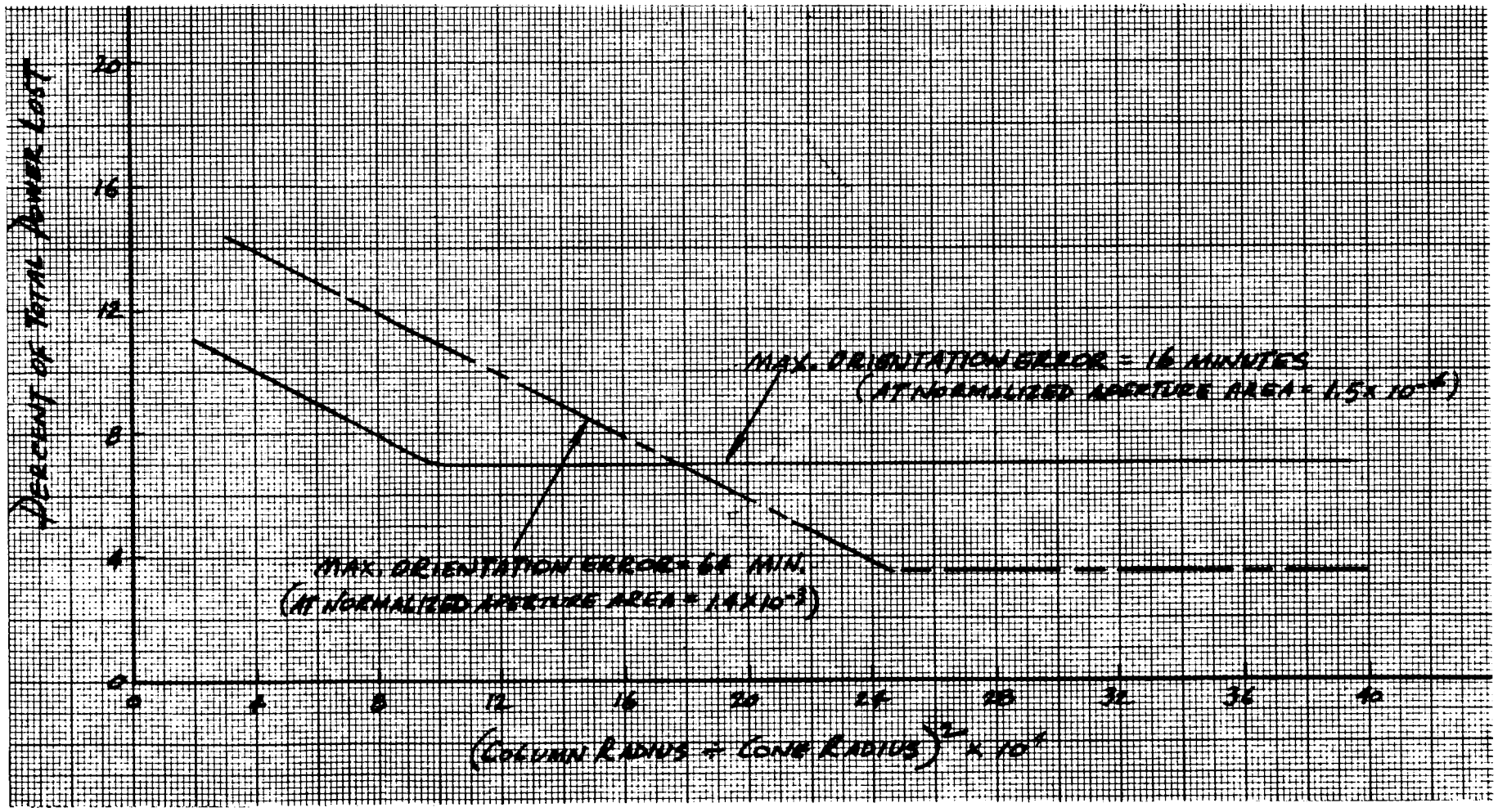

Figure 39. Power Loss versus Ratio of Cross-Sectional Area (Column-to-Cone) - Orientation Error

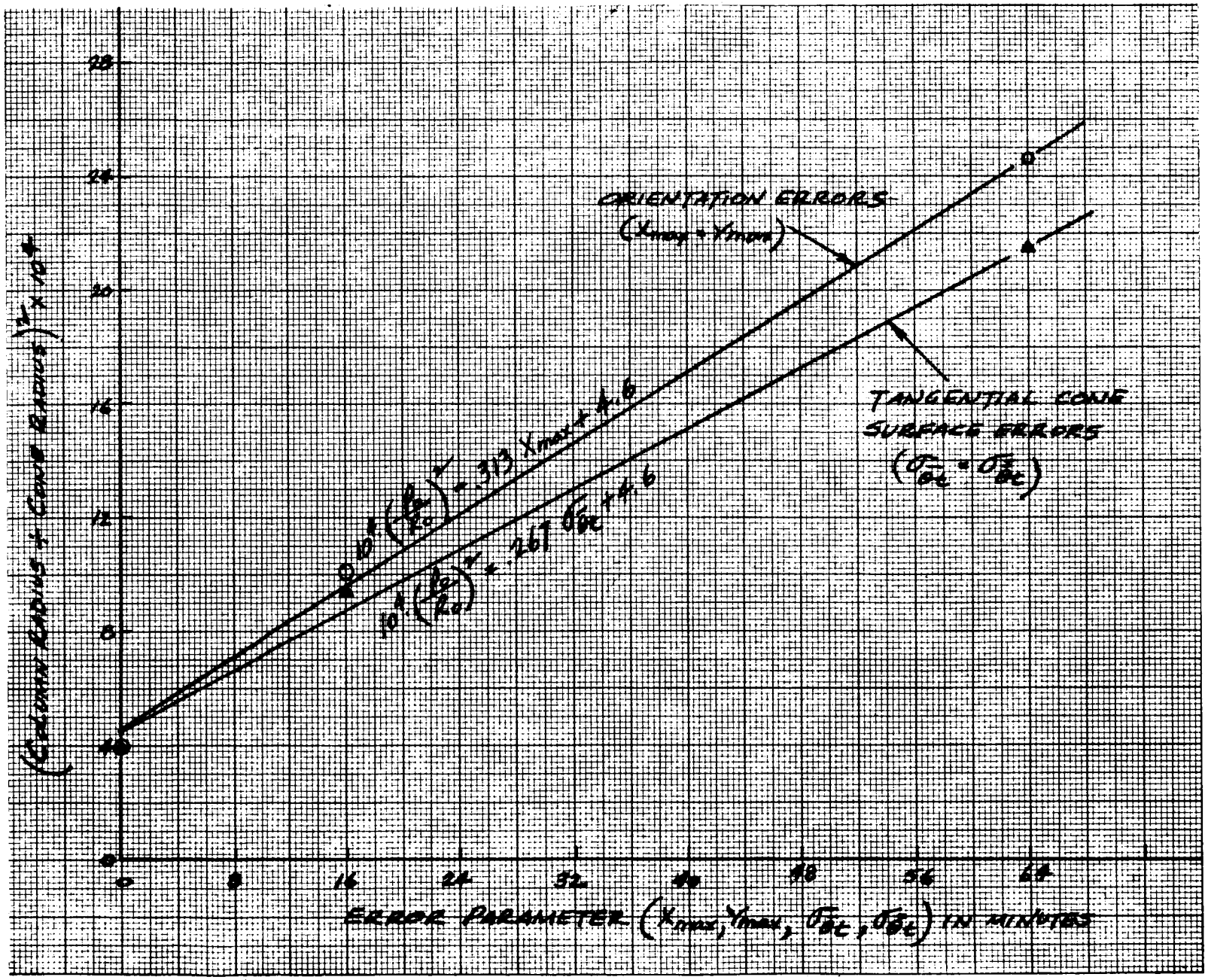

Figure 40. Ratio of Cross-Sectional Error (Column-to-Cone) versus Error Parameter

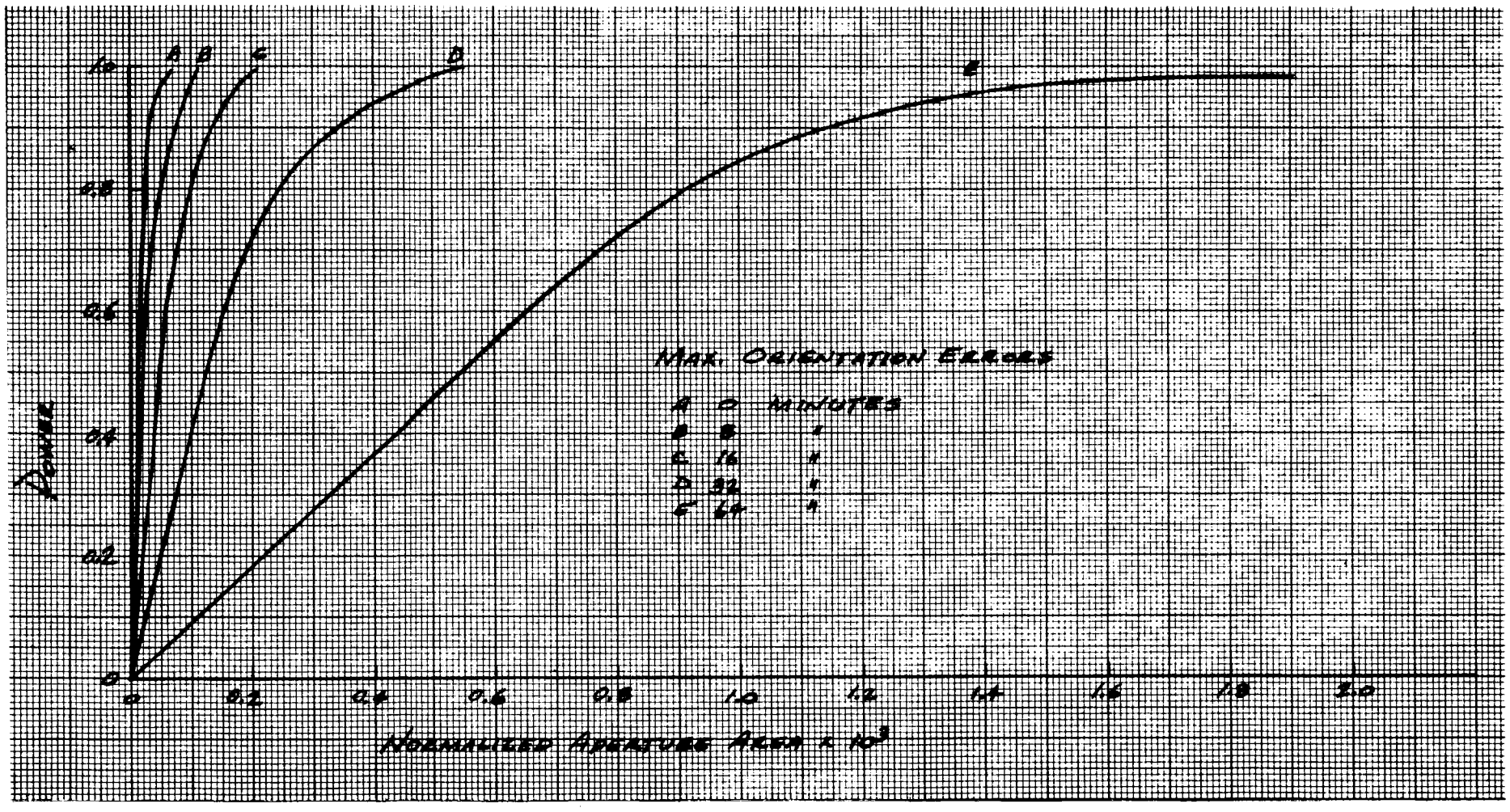

Figure 41. Power versus Area - Orientation Error (X_{max}, Y_{max})

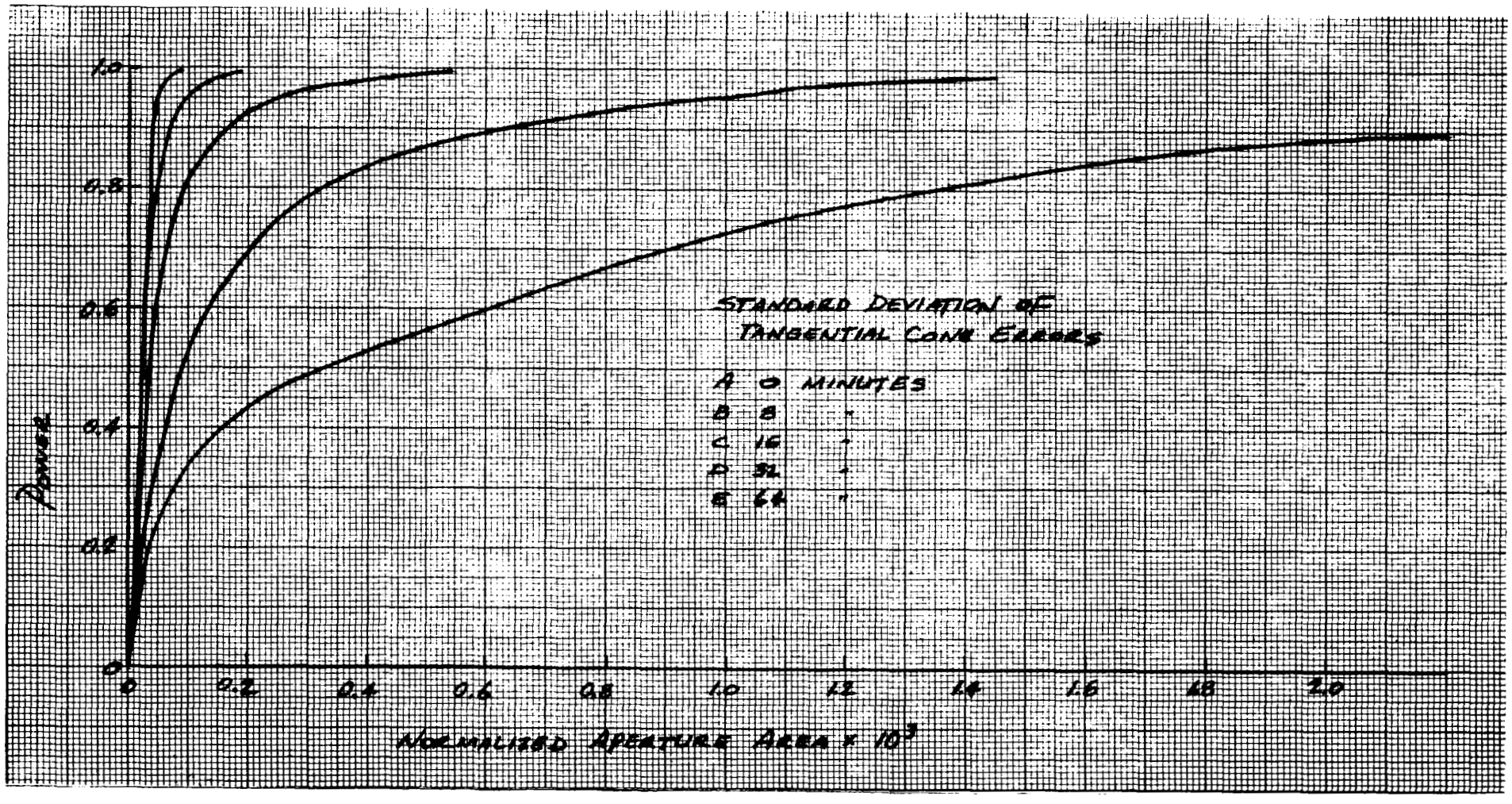

Figure 42. Power versus Area - Tangential Cone Errors ($\bar{\theta}_t$, $\bar{\bar{\theta}}_t$)

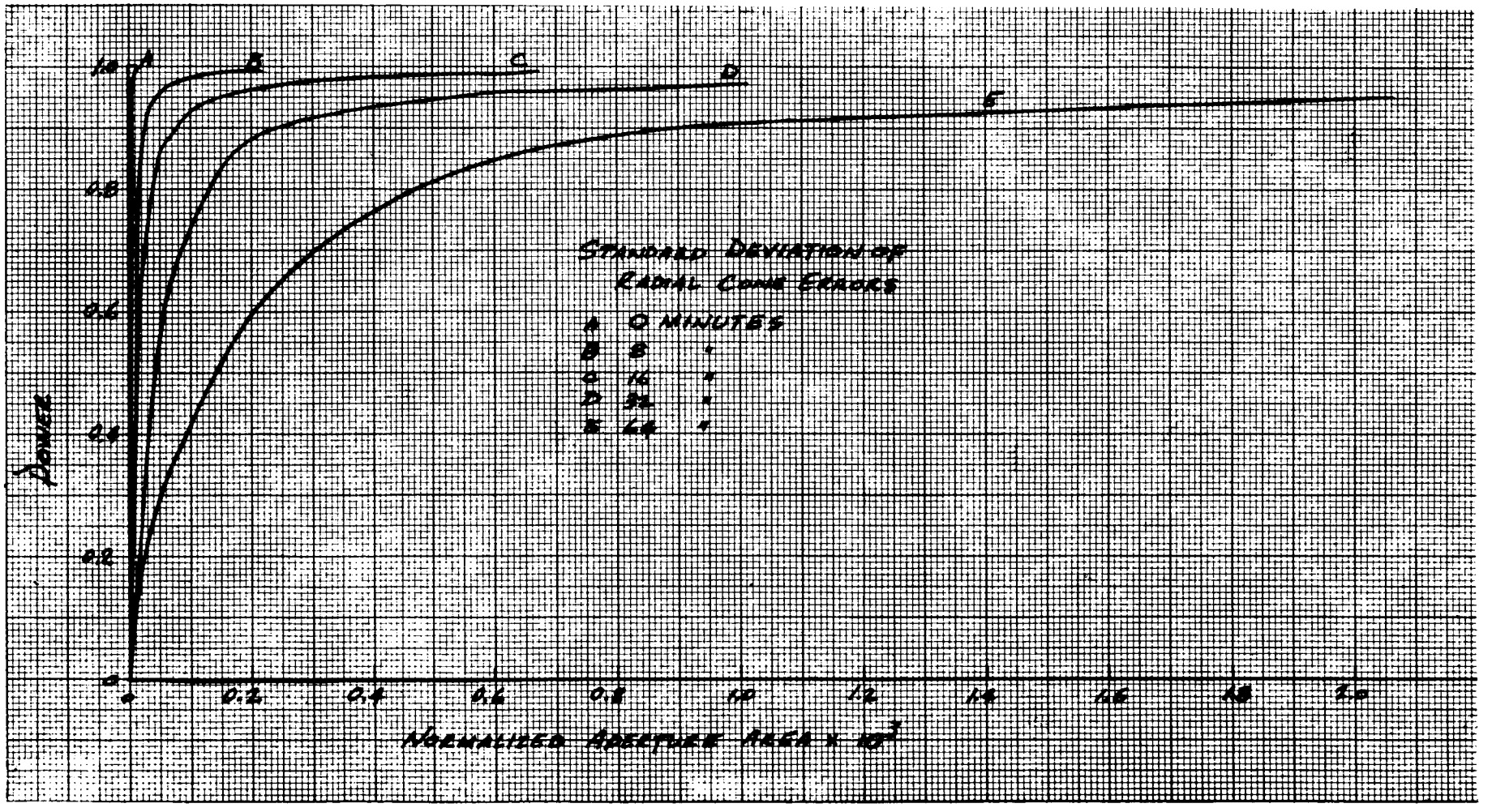

Figure 43. Power versus Area - Radial Cone Errors ($\bar{\theta}_r$, $\bar{\bar{\theta}}_r$)

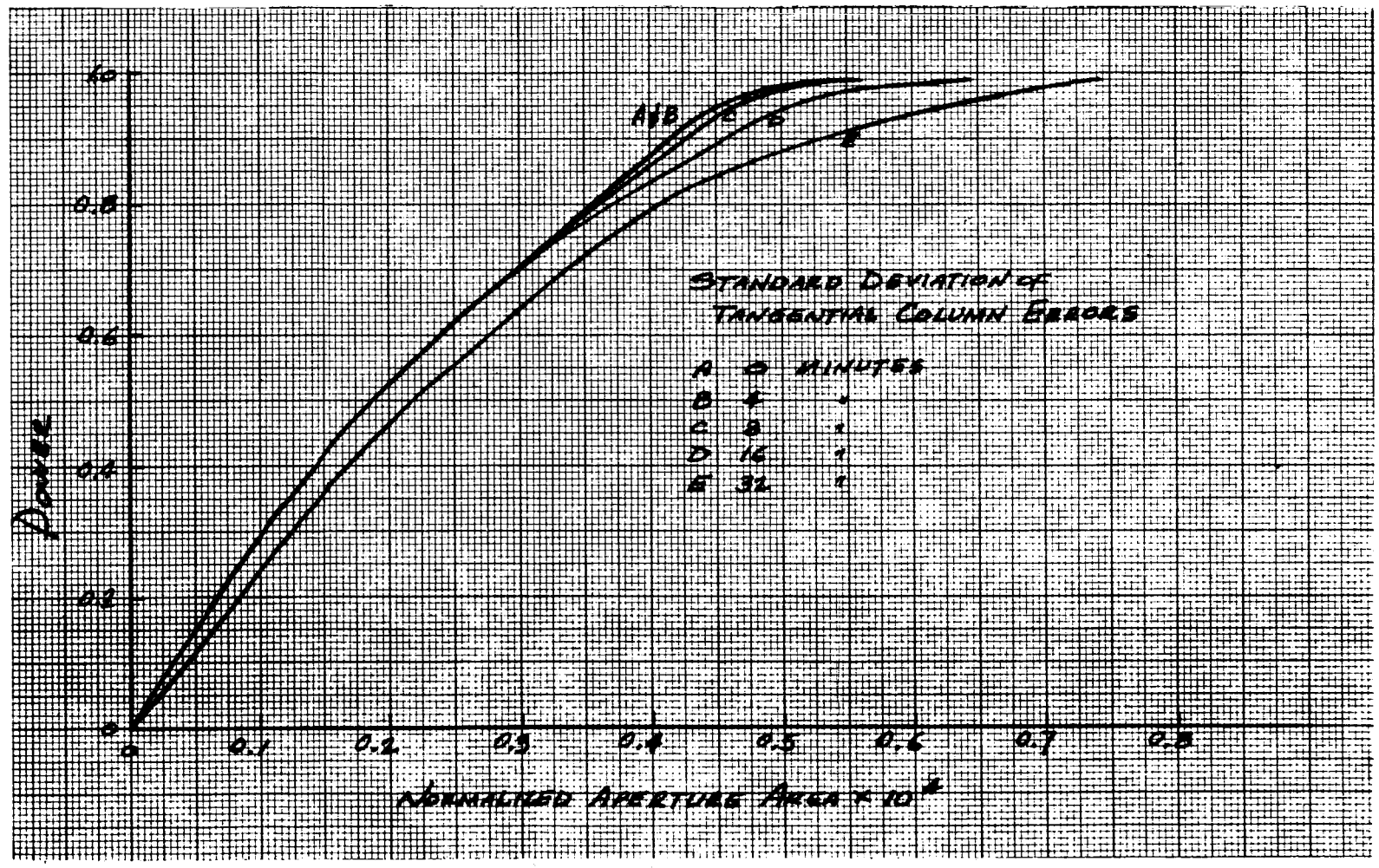

Figure 44. Power versus Area - Tangential Column Errors ($\bar{\alpha}_t$)

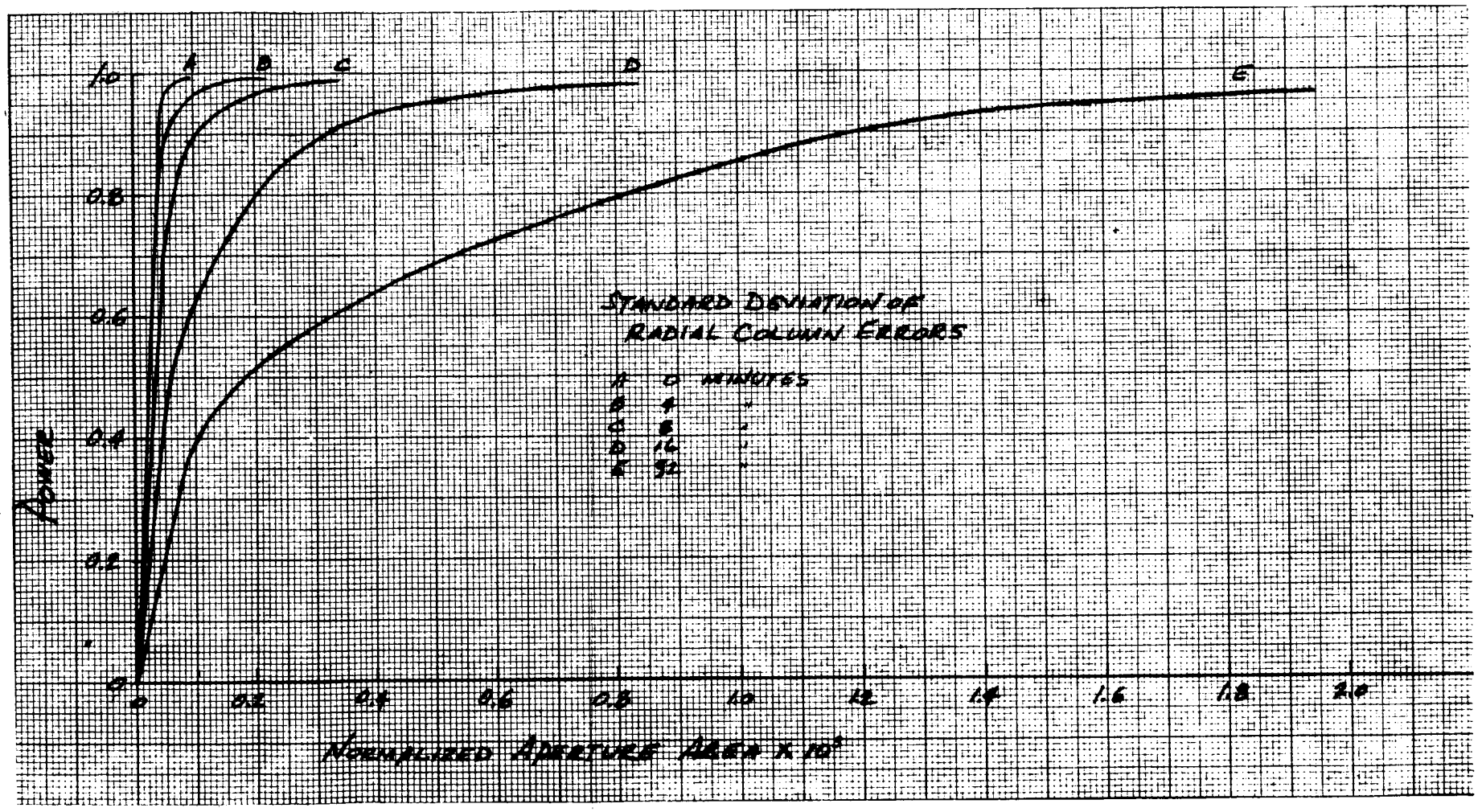

Figure 45. Power versus Area - Radial Column Errors ($\bar{\alpha}_r$)

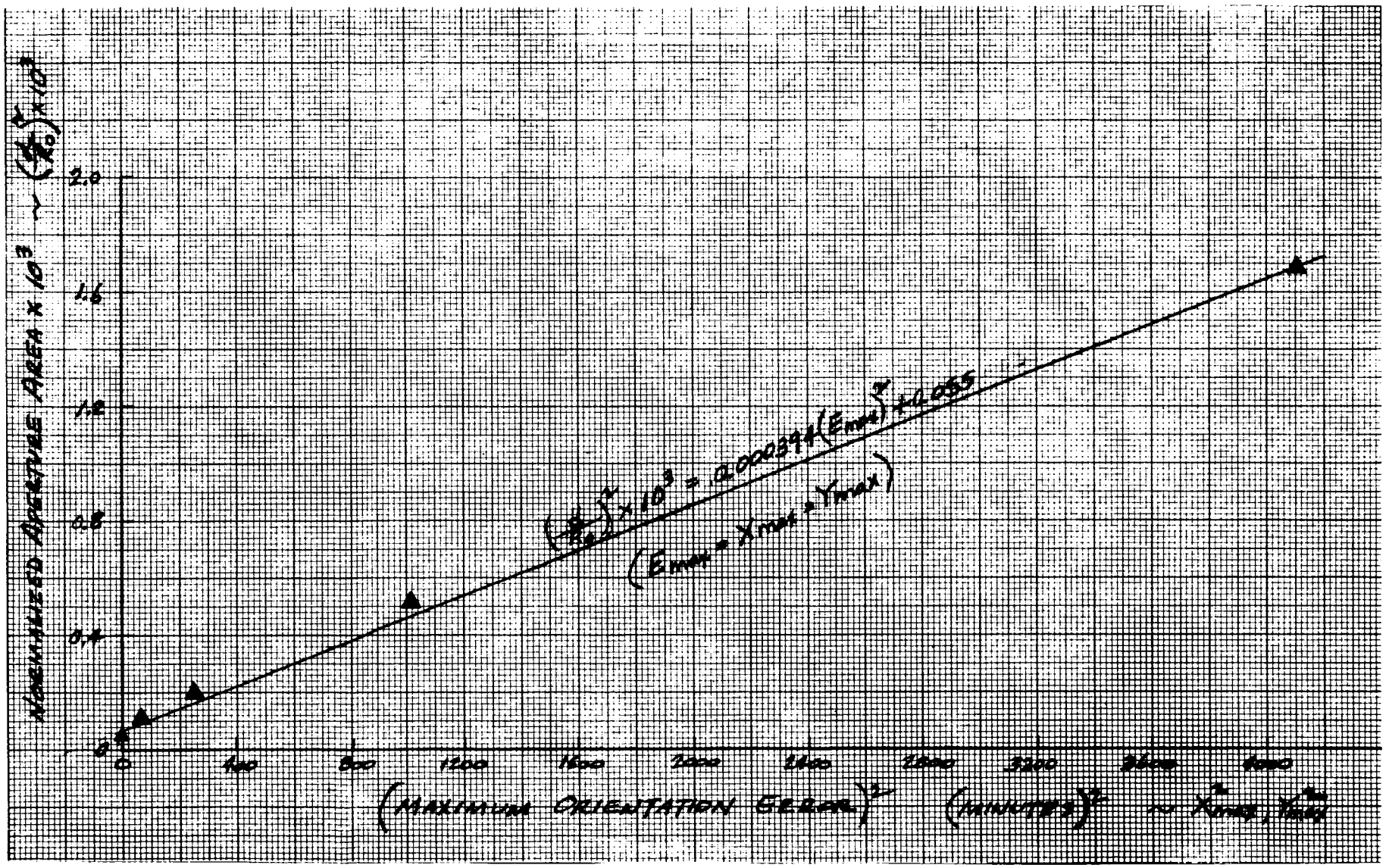

Figure 46. Area versus (Error)^2 - Orientation Errors

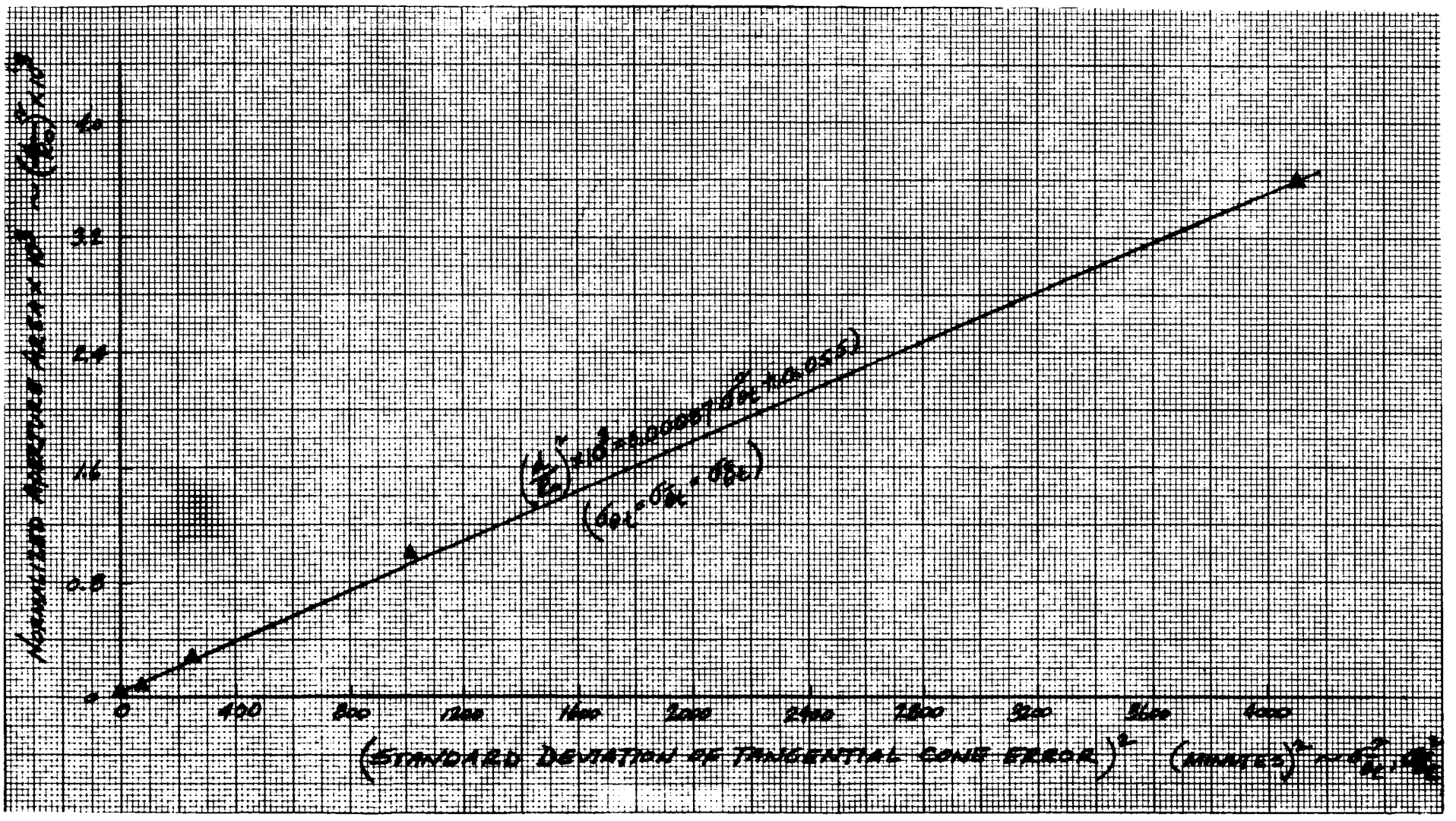

Figure 47. Area versus (Error)^2 - Tangential Cone Errors

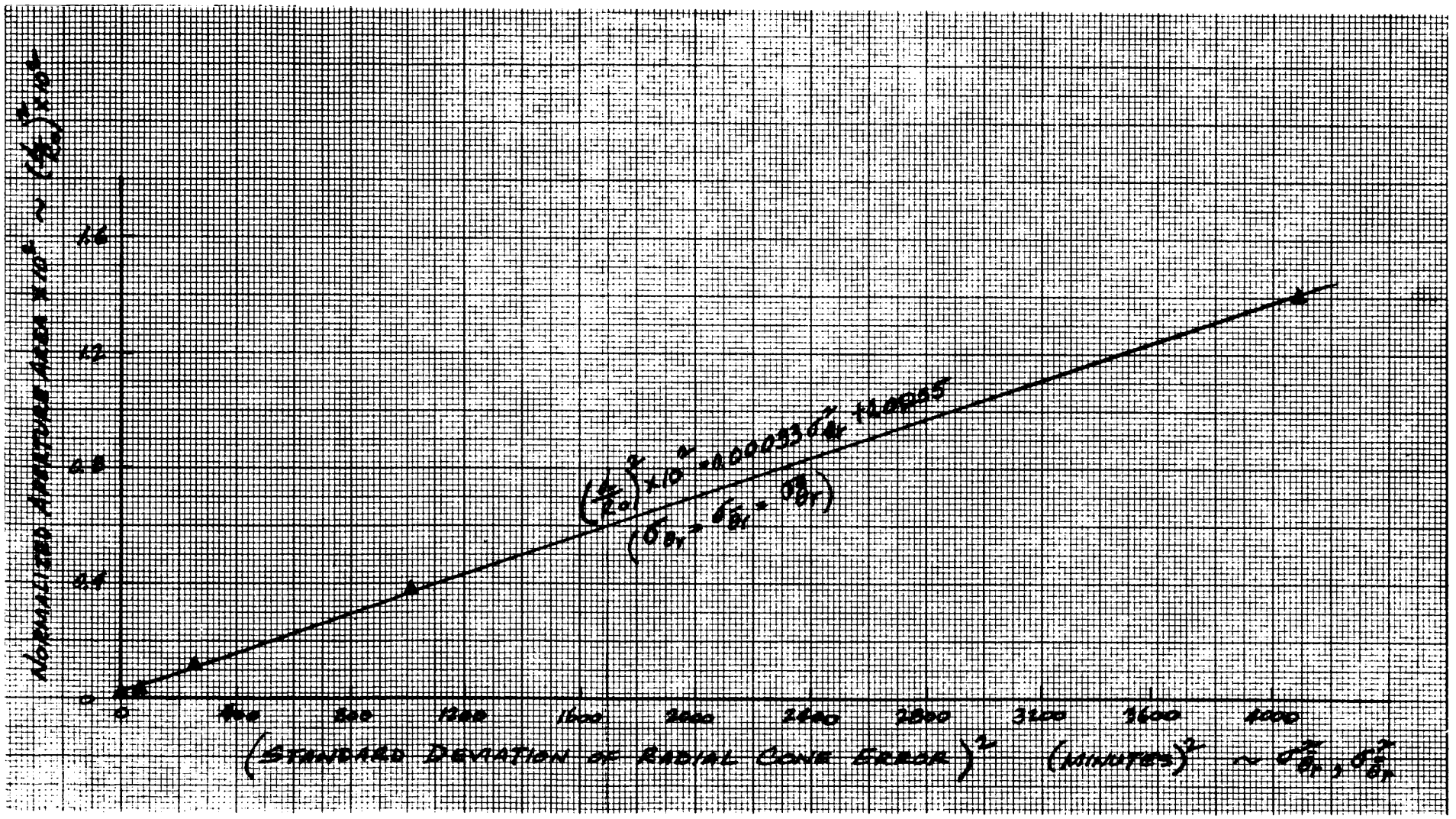

Figure 48. Area versus (Error)^2 - Radial Cone Errors

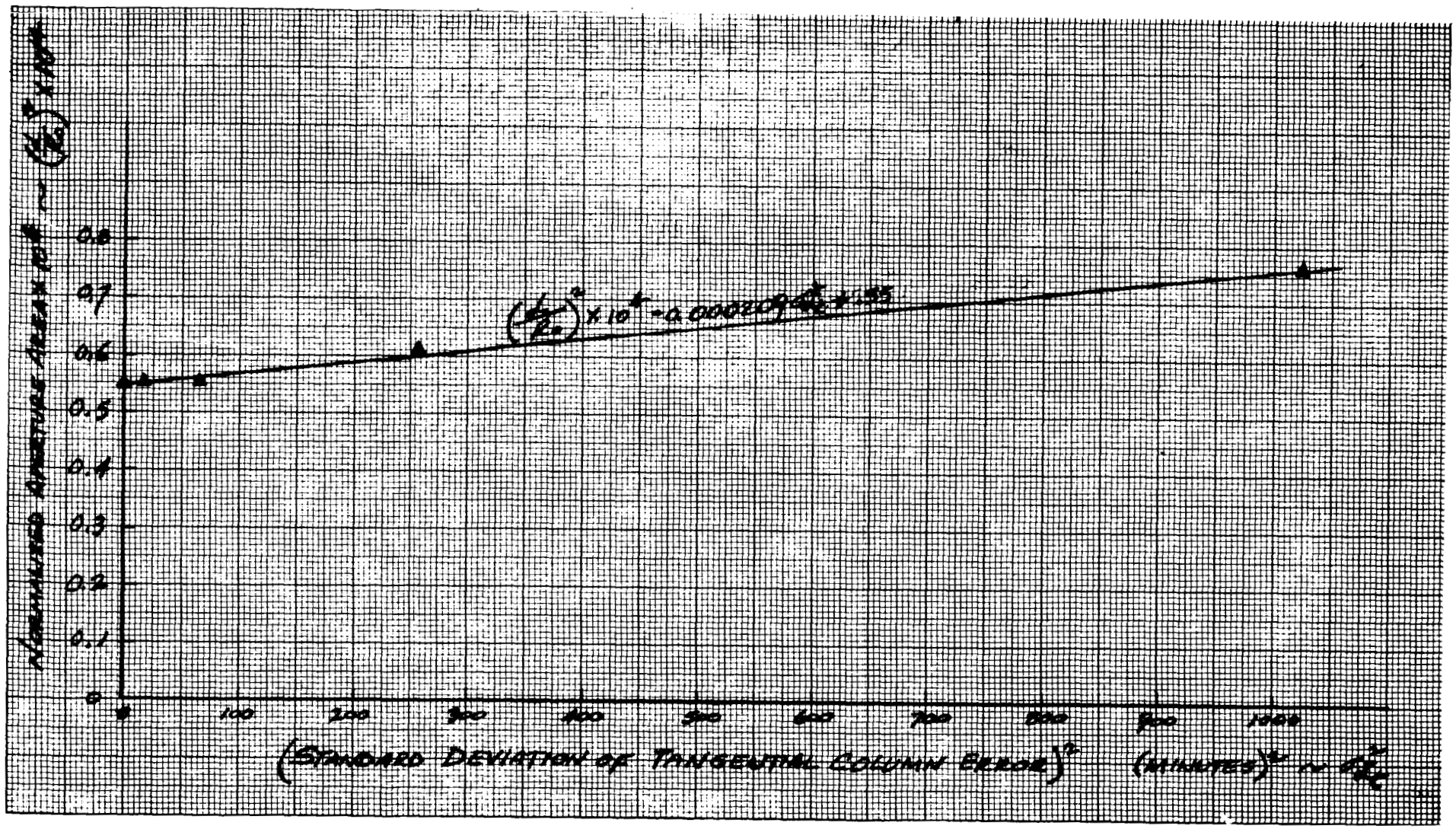

Figure 49. Area versus $(\text{Error})^2$ - Tangential Column Errors

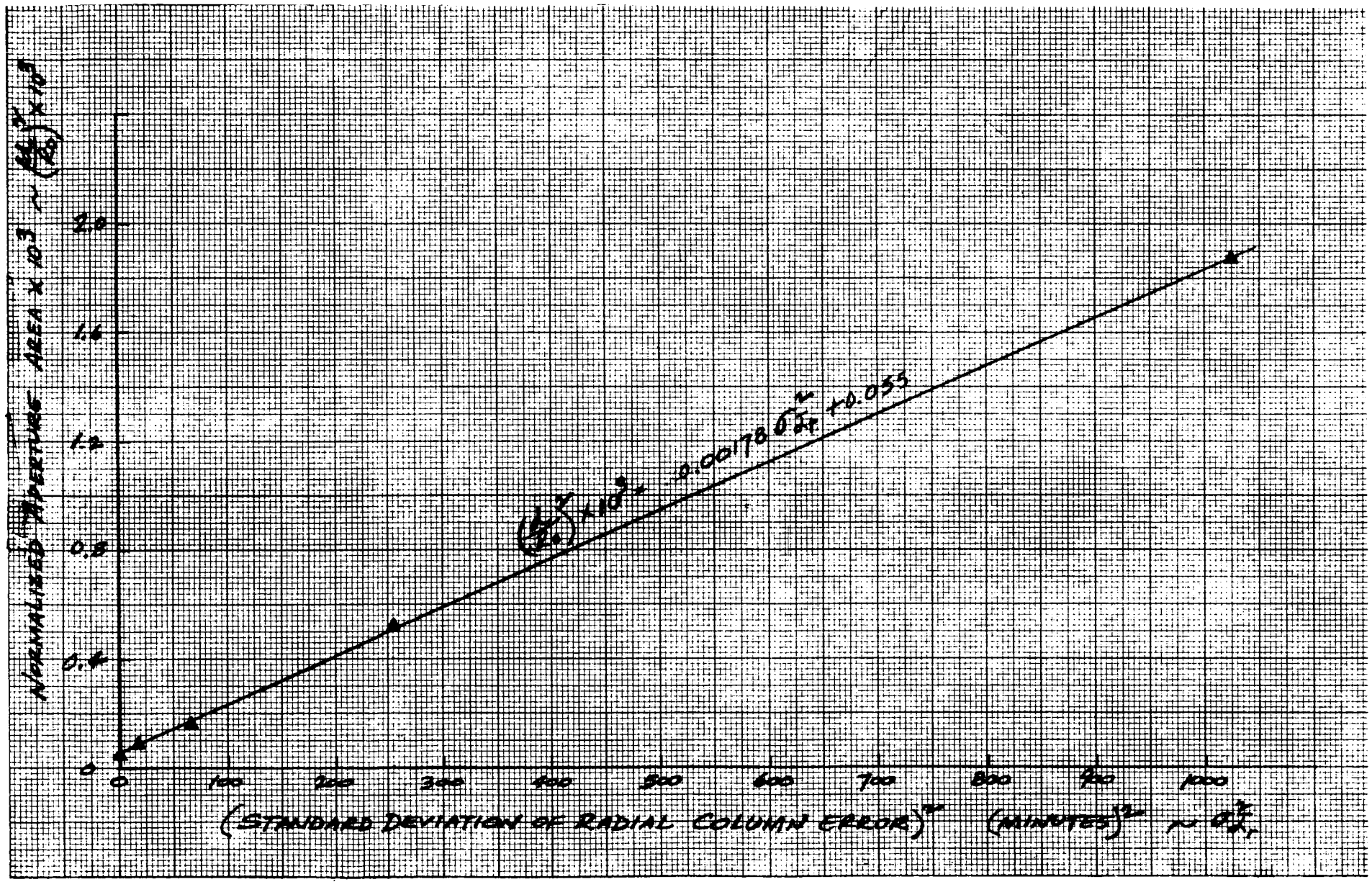

Figure 50. Area versus $(\text{Error})^2$ - Radial Column Errors

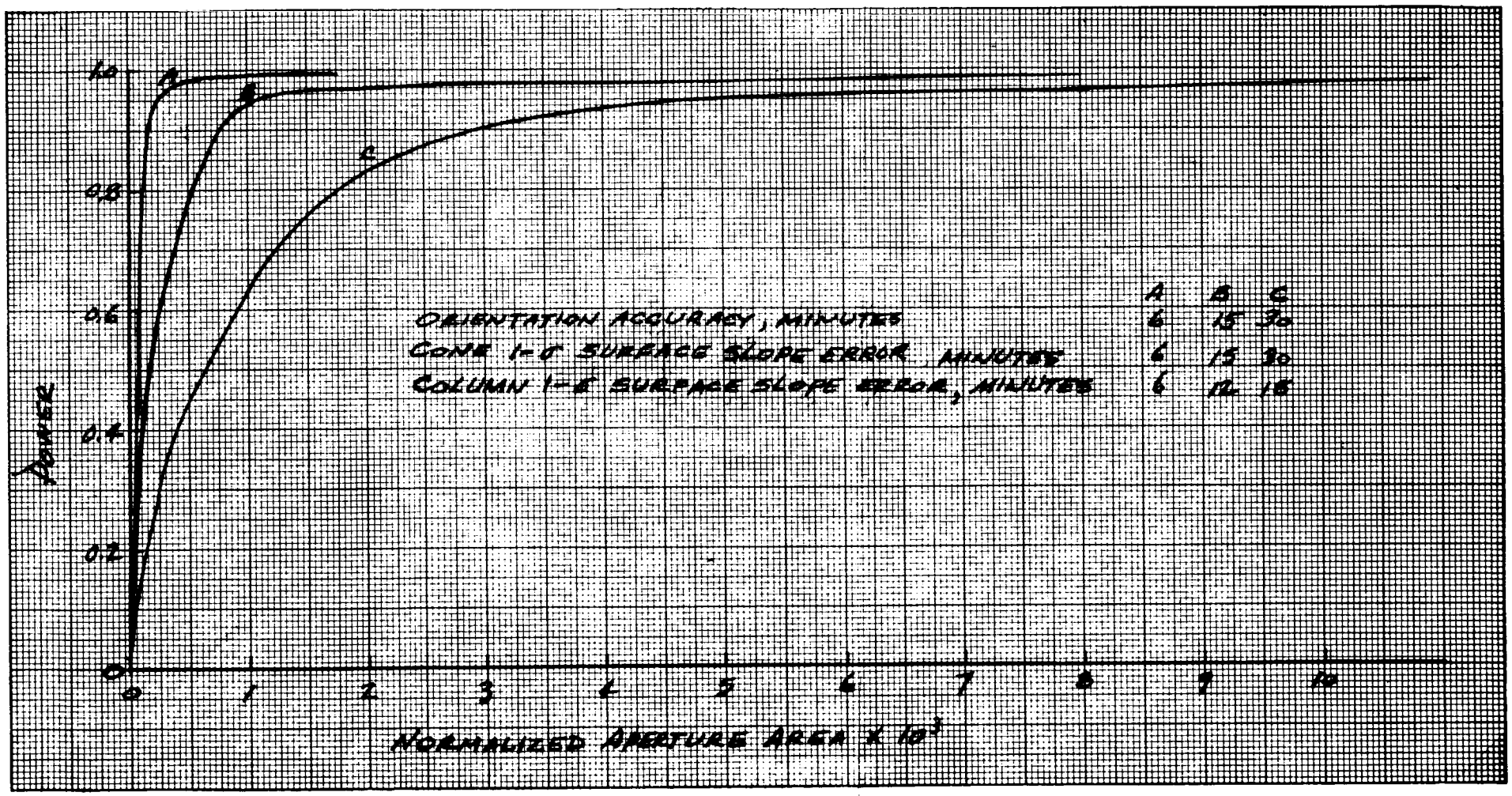

Figure 51. Performance of Cone-and-Column Concentrators with Various Accuracies

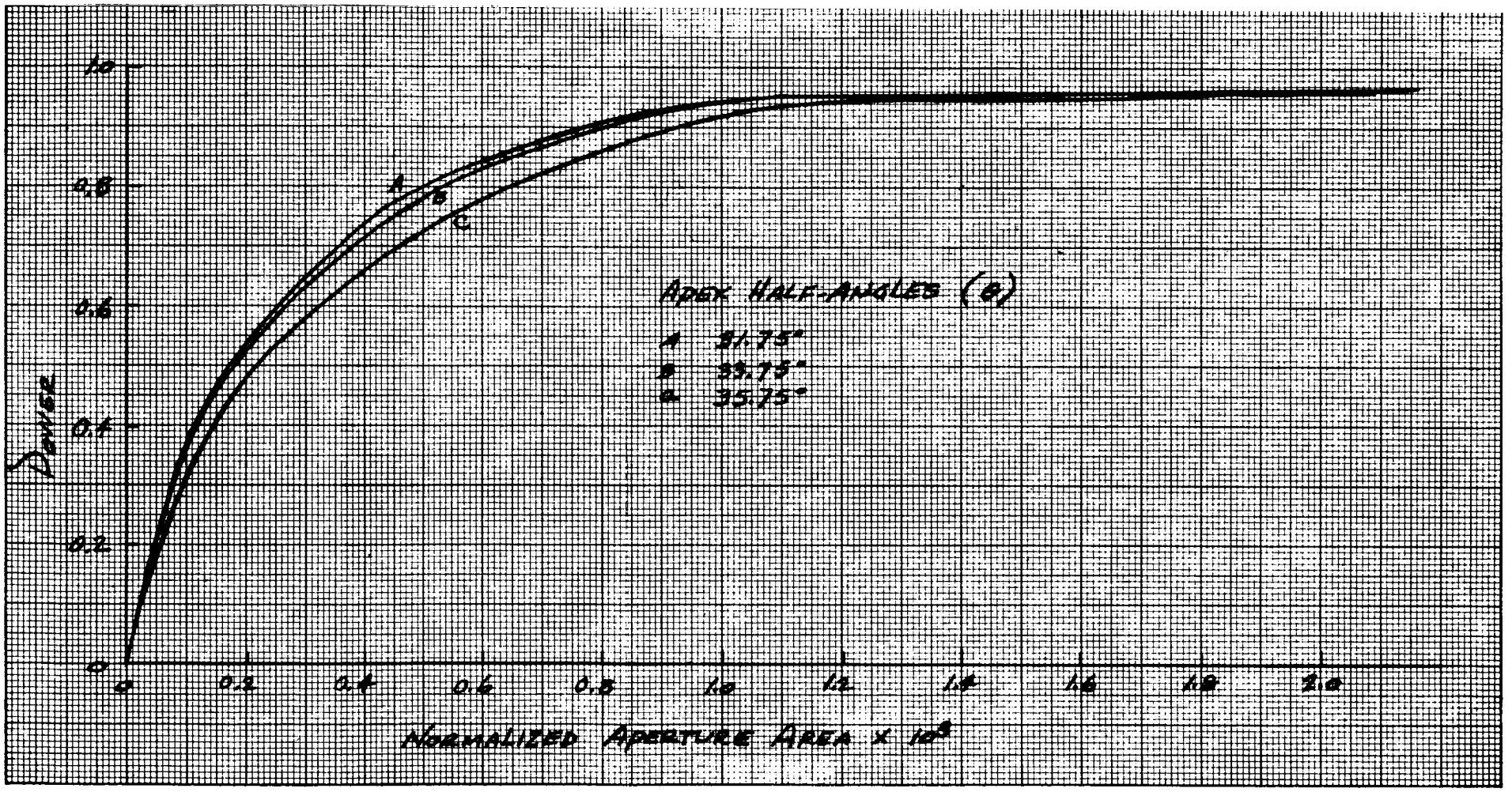

Figure 52. Power versus Area - Effective Rim Angle of 45 Degrees and Various Half-Angles (θ)

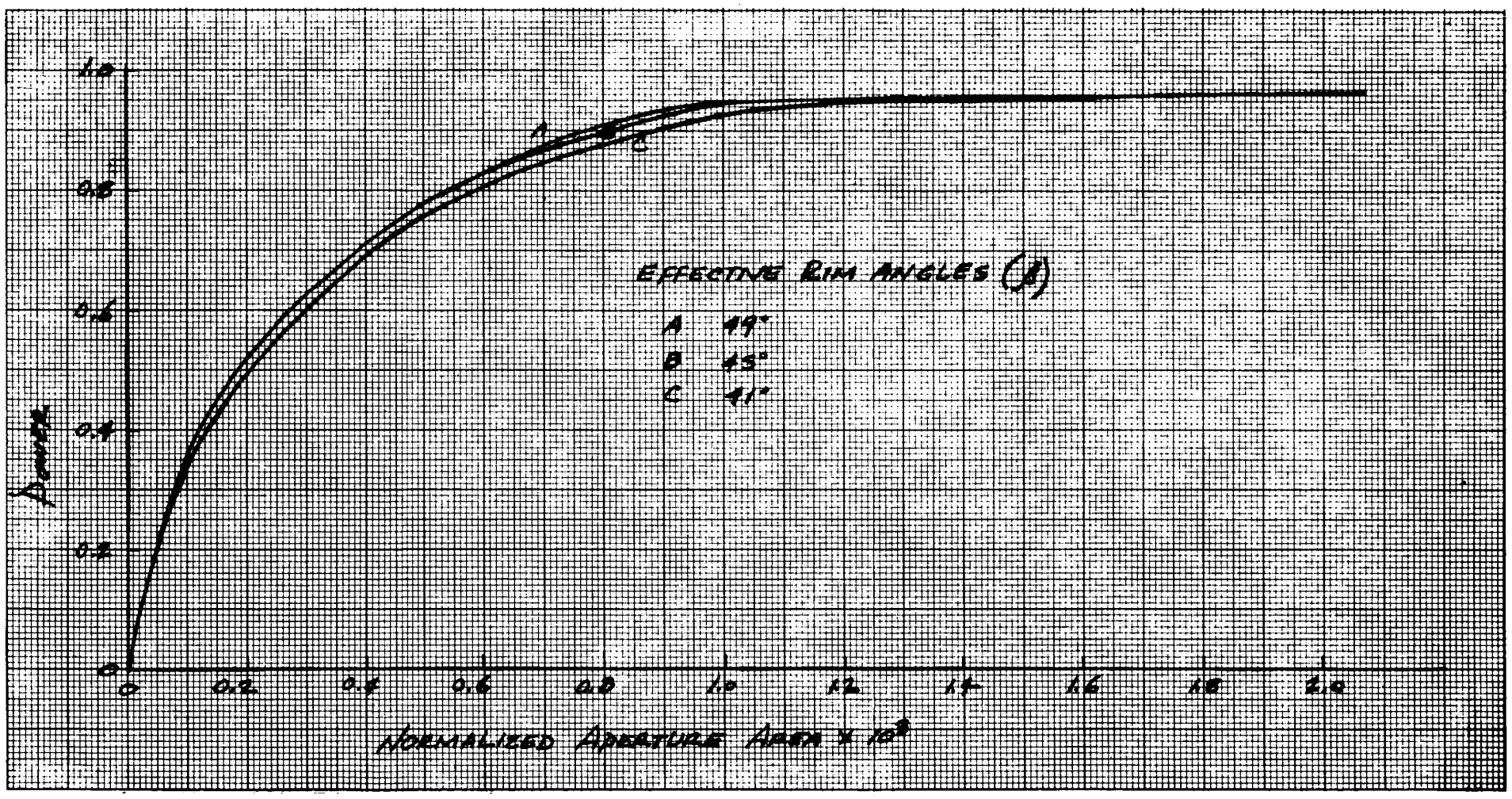

Figure 53. Power versus Area - Apex Half-Angle of 33.75 Degrees and Various Effective Rim Angles (β)

Table XII. Input Data for Computer Runs

Computer Run No.	S (Ft)	θ (Deg)	X_{max} (Min)	Y_{max} (Min)	$\sigma_{\bar{\theta}_r}$ (Min)	$\sigma_{\bar{\theta}_t}$ (Min)	$\sigma_{\bar{\alpha}_r}$ (Min)	$\sigma_{\bar{\alpha}_t}$ (Min)	$\sigma_{\bar{\bar{\theta}}_r}$ (Min)	$\sigma_{\bar{\bar{\theta}}_t}$ (Min)	p_1 (Ft)	p_2 (Ft)	p_3 (Ft)	p_4 (Ft)	Fig. No.
Column Sizing															
10	152.241	33.75	0	0	0	0	0	0	0	0	10.0				29
11	144.803	33.75	0	0	0	0	0	0	0	0	3.12				29
12	143.813	33.75	0	0	0	0	0	0	0	0	2.21				29
13	143.374	33.75	0	0	0	0	0	0	0	0	1.56				29
14	143.112	33.75	0	0	0	0	0	0	0	0	1.80				29
15	142.934	33.75	0	0	0	0	0	0	0	0	1.40				29
20	152.241	33.75	0	0	0	0	0	0	0	0		10.0			30
21	144.803	33.75	0	0	0	0	0	0	0	0		2.94			30
22	143.813	33.75	0	0	0	0	0	0	0	0		2.09			30
23	143.374	33.75	0	0	0	0	0	0	0	0		1.70			30
24	143.112	33.75	0	0	0	0	0	0	0	0		1.47			30
25	142.934	33.75	0	0	0	0	0	0	0	0		1.32			30
30	152.241	33.75	0	0	0	0	0	0	0	0			10.0		31
31	144.803	33.75	0	0	0	0	0	0	0	0			2.43		31
32	143.813	33.75	0	0	0	0	0	0	0	0			1.72		31
33	143.374	33.75	0	0	0	0	0	0	0	0			1.40		31
34	143.112	33.75	0	0	0	0	0	0	0	0			1.21		31
35	142.934	33.75	0	0	0	0	0	0	0	0			1.09		31
40	152.241	33.75	0	0	0	0	0	0	0	0				10.0	32
41	144.803	33.75	0	0	0	0	0	0	0	0				1.15	32
42	143.813	33.75	0	0	0	0	0	0	0	0				0.81	32
43	143.374	33.75	0	0	0	0	0	0	0	0				0.66	32
44	143.112	33.75	0	0	0	0	0	0	0	0				0.57	32
45	142.934	33.75	0	0	0	0	0	0	0	0				0.52	32
Column Sizing - Orientation															
1	144.073	33.75	16	16	0	0	0	0	0	0	2.45	2.45	1.775	1.02	34
2	144.484	33.75	16	16	0	0	0	0	0	0	2.83	2.83	2.05	1.17	34
3	144.841	33.75	16	16	0	0	0	0	0	0	3.16	3.16	2.29	1.31	34
4	143.586	33.75	64	64	0	0	0	0	0	0	2.00	2.00	1.45	0.83	Input Error
11	144.841	33.75	64	64	0	0	0	0	0	0	3.16	3.16	2.29	1.31	35
12	145.610	33.75	64	64	0	0	0	0	0	0	3.87	3.87	2.80	1.60	35
13	146.259	33.75	64	64	0	0	0	0	0	0	4.47	4.47	3.24	1.86	35
14	146.833	33.75	64	64	0	0	0	0	0	0	5.00	5.00	3.62	2.07	35
Column Sizing - Tangential Cone Error															
1	144.224	33.75	0	0	0	16	0	0	0	16	2.59	2.59	1.88	1.07	36
2	144.441	33.75	0	0	0	16	0	0	0	16	2.79	2.79	2.02	1.16	36
3	144.636	33.75	0	0	0	16	0	0	0	16	2.97	2.97	2.15	1.23	36
4	144.831	33.75	0	0	0	16	0	0	0	16	3.15	3.15	2.28	1.31	36
5	145.004	33.75	0	0	0	16	0	0	0	16	3.31	3.31	2.40	1.37	36
11	144.950	33.75	0	0	0	64	0	0	0	64	3.26	3.26	2.36	1.35	37
12	145.318	33.75	0	0	0	64	0	0	0	64	3.60	3.60	2.61	1.49	37
13	145.653	33.75	0	0	0	64	0	0	0	64	3.91	3.91	2.93	1.62	37
14	145.967	33.75	0	0	0	64	0	0	0	64	4.20	4.20	3.04	1.74	37
15	146.259	33.75	0	0	0	64	0	0	0	64	4.47	4.47	3.24	1.86	37

Table XII. Input Data for Computer Runs (Continued)

Computer Run No.	S (Ft)	θ (Deg)	X_{max} (Min)	Y_{max} (Min)	$\sigma_{\bar{\theta}_r}$ (Min)	$\sigma_{\bar{\theta}_t}$ (Min)	$\sigma_{\bar{\alpha}_r}$ (Min)	$\sigma_{\bar{\alpha}_t}$ (Min)	$\sigma_{\bar{\bar{\theta}}_r}$ (Min)	$\sigma_{\bar{\bar{\theta}}_t}$ (Min)	p_1 (Ft)	p_2 (Ft)	p_3 (Ft)	p_4 (Ft)	Fig. No.
Zero Error	152.241	33.75	0	0	0	0	0	0	0	0	10.0	7.78	5.56	3.33	41 - 45
Radial Cone Error															
1	152.241	33.75	0	0	8	0	0	0	8	0	10.0	7.78	5.56	3.33	43
2	152.241	33.75	0	0	16	0	0	0	16	0	10.0	7.78	5.56	3.33	43
3	152.241	33.75	0	0	32	0	0	0	32	0	10.0	7.78	5.56	3.33	43
4	152.241	33.75	0	0	64	0	0	0	64	0	10.0	7.78	5.56	3.33	43
Tangential Cone Error															
1	152.241	33.75	0	0	0	8	0	0	0	8	10.0	7.78	5.56	3.33	42
2	152.241	33.75	0	0	0	16	0	0	0	16	10.0	7.78	5.56	3.33	42
3	152.241	33.75	0	0	0	32	0	0	0	32	10.0	7.78	5.56	3.33	42
4	152.241	33.75	0	0	0	64	0	0	0	64	10.0	7.78	5.56	3.33	42
Radial Column Error															
1	152.241	33.75	0	0	0	0	4	0	0	0	10.0	7.78	5.56	3.33	45
2	152.241	33.75	0	0	0	0	8	0	0	0	10.0	7.78	5.56	3.33	45
3	152.241	33.75	0	0	0	0	16	0	0	0	10.0	7.78	5.56	3.33	45
4	152.241	33.75	0	0	0	0	32	0	0	0	10.0	7.78	5.56	3.33	45
Tangential Column Error															
1	152.241	33.75	0	0	0	0	0	4	0	0	10.0	7.78	5.56	3.33	44
2	152.241	33.75	0	0	0	0	0	8	0	0	10.0	7.78	5.56	3.33	44
3	152.241	33.75	0	0	0	0	0	16	0	0	10.0	7.78	5.56	3.33	44
4	152.241	33.75	0	0	0	0	0	32	0	0	10.0	7.78	5.56	3.33	44
Orientation															
1	152.241	33.75	8	8	0	0	0	0	0	0	10.0	7.78	5.56	3.33	41
2	152.241	33.75	16	16	0	0	0	0	0	0	10.0	7.78	5.56	3.33	41
3	152.241	33.75	32	32	0	0	0	0	0	0	10.0	7.78	5.56	3.33	41
4	152.241	33.75	64	64	0	0	0	0	0	0	10.0	7.78	5.56	3.33	41
Production															
1	144.497	33.75	6	6	6	6	6	6	6	6	2.842	2.842	2.06	1.18	51
2	145.366	33.75	15	15	15	15	12	12	15	15	3.645	3.645	2.64	1.51	51, 52, 53
3	146.139	33.75	30	30	30	30	18	18	30	30	4.359	4.359	3.16	1.81	51
4	142.404	31.75	15	15	15	15	12	12	15	15	3.645	3.645	2.64	1.51	52
5	154.385	35.75	15	15	15	15	12	12	15	15	3.645	3.645	2.64	1.51	52
6	140.262	33.75	15	15	15	15	12	12	15	15	3.645	3.645	2.64	1.51	53
7	154.496	33.75	15	15	15	15	12	12	15	15	3.645	3.645	2.64	1.51	53

SECTION VII. EVALUATION

A. PERFORMANCE CRITERIA

The efficiency of a concentrator-reciever combination may be expressed simply as the ratio of usable input to total input:

$$\eta = \frac{q_S A_C t_i (1 - L) \alpha - A_0 \epsilon \sigma T^4 t_r}{q_S A_C t_i}, \tag{27}$$

where

q_S = solar constant,

A_C = area of concentrator intercepting solar energy,

t_i = time in the sun,

L = fractional reflectance loss of concentrator (reflectance = 1 - L),

α = absorptivity of receiver,

A_0 = aperture area of receiver,

ϵ = emissivity of receiver,

σ = Stephan-Boltzmann constant,

T = absolute temperature of receiver,

and

t_r = time in which receiver radiates.

If, for the purpose of evaluating concentrators, a black body receiver is assumed, then $\alpha = \epsilon = 1$. The efficiency then reduces to

$$\eta = 1 - L - \left(\frac{A_0}{A_C}\right)\left(\frac{\sigma T^4}{q_S}\right)\left(\frac{t_r}{t_i}\right). \tag{28}$$

Thus, concentrator-receiver losses may be divided into two factors: a reflectance loss factor, L, and a radiation loss factor, $(A_0/A_c)\ (\sigma T^4/q_s)\ (t_r/t_i)$. Each of these factors contains a significant property of the concentrator. L is the complement of reflectance, and A_0/A_c is the reciprocal of the area concentration ratio. L and A_0/A_c are then the chief criteria by which concentrator performance should be evaluated. The evaluation is fortunately simplified by the independent effect on these criteria on performance and also by their independence of each other. The evaluation of the cone-and-column concentrator therefore considers these criteria separately.

A problem does arise however, in selecting a proper value of receiver aperture area, A_0, for use in the calculation of the radiation loss factor. The aperture cannot be made large enough to include all of the energy in the focal plane, since the focal plane flux profile approaches zero asymptotically. There does exist, though, an optimum area aperture that will produce maximum receiver efficiency. This optimum is a function of receiver temperature, a fact that complicates the general analysis of concentrators. The optimum aperture for a particular concentrator and a particular receiver temperature is obtained by plotting focused power and radiated power against aperture area. The maximum difference between these two curves is the maximum net power, and the corresponding aperture area is the optimum aperture area. Since reradiation plots as a straight line on these coordinates, the optimization may be accomplished by moving the radiation line up until it is tangent to the focused power curve. The point of tangency then defines the optimum aperture area and the focused power entering the aperture. The y-intercept gives the maximum net power, which is the complement of the radiation loss factor. The point where this radiation line crosses 100 percent power defines an "effective aperture area," which is the value that should be used in Equation 28 to obtain the radiation loss factor. The effective aperture area, like the optimum aperture area, is a function of receiver temperature, but

it is not as sensitive a parameter. For the purpose of the analysis, it was assumed that the accuracy to which the concentrator is constructed will be governed by the receiver temperature and the resulting radiation loss factor will be about 25 percent. Therefore, the effective aperture area is defined by the 100 percent power intercept of a line drawn from the 75 percent point on the ordinate scale and tangent to the power versus area curve. The effective concentration ratio is defined as the ratio of the concentrator frontal area to the effective aperture area.

B. LOSSES IN SYSTEM

1. Reflection Losses

Because of the significant effect of reflectance losses on performance and because the cone-and-column concentrator utilizes three reflections, the subject of reflectance losses should be considered in detail. The evaluation made here will be based mainly on theoretical considerations for reasons that will become apparent.

The reflectance of a reflector may be defined as the ratio of reflected energy to incident energy. The reflectance may be subdivided into specular and diffuse components, of which only the specular component is useful in concentrating systems. Reflectance is also a function of the wave length of the incident energy. Only those wave lengths found in the solar spectrum are of interest here.

Reflectance is sometimes described as a property of a reflecting material and is measured under conditions that eliminate or at least minimize all deleterious effects. This is, of course, the only approach that will yield reproducible results. In a practical reflector for a solar concentrator, this property of some specific reflecting material can serve as a guide to the reflectance that can be obtained; but in the final analysis, reflectance will be found to be a function of many more factors than the reflecting material. The following are among the more important factors:

(1) The specularity of the substrate material to which the reflecting material is applied.

(2) The method of application of the reflecting material to the substrate material.

(3) The properties and thickness of any overcoating material used.

(4) The environment to which the reflector is subjected during use and between manufacture and use.

(5) The angle of incidence of the incident energy.

These factors will be discussed generally in this report, but detailed examination is given in References 2 through 7.

Some loss of specularity is encountered in using a substrate material other than glass. The best plastic films will exhibit a diffuse component that is about 2 percent of the total reflectance. Polished metal substrates will produce a diffuse component that will depend greatly on the ability of the material to be polished and on the care taken in polishing.

The vacuum-vapor deposition method of applying the reflecting material to the substrate produces the best reflectance. To obtain maximum reflectance, the material must be "flash" deposited and the angle of incidence of deposited material must be limited (References 2 and 3).

Often a transparent overcoating is applied to the reflector for one or more of the following purposes:

(1) Protection of the reflecting material.

(2) Increasing the thermal emissivity of the reflecting surface (References 4 and 5).

(3) Enhancing the reflectance of the reflecting material.

Environmental factors that may cause degradation are oxidation, radiation, and meteorite damage (Reference 2).

At angles of incidence greater than approximately 60 degrees, some loss in reflectance will be experienced (Reference 6). The amount of loss is a function of the reflecting material and the wave length of the incident energy and probably the thickness and type of any transparent overcoating that may be used.

Since reflectance is a function of wave length, the spectrum of energy reflected from a surface will differ from the spectrum of the energy incident on the surface. With the cone-and-column concentrator, this change in spectrum at each of the three reflections must be taken into account in determining the over-all reflectance loss. The loss factor, L, is then given by

$$L = 1 - \frac{\int_0^\infty \rho_1(\lambda)\,\rho_2(\lambda)\,\rho_3(\lambda)\,E(\lambda)\,d\lambda}{\int_0^\infty E(\lambda)\,d\lambda}, \tag{29}$$

where

$\rho_1(\lambda)$, $\rho_2(\lambda)$, and $\rho_3(\lambda)$ are the spectral reflectances of the three reflecting surfaces,

$E(\lambda)$ is the energy distribution in the solar spectrum (Reference 7),

and

λ is the wave length.

If each of the three surfaces has the same spectral reflectance, $\rho(\lambda)$, Equation 29 becomes

$$L = 1 - \frac{\int_0^\infty \left[\rho(\lambda)\right]^3 E(\lambda)\,d\lambda}{\int_0^\infty E(\lambda)\,d\lambda}. \tag{30}$$

The value of L has been calculated for carefully prepared samples of aluminum and silver (Reference 3). This was done by plotting $\rho(\lambda)$ against

$$\frac{\int_0^{\lambda} E(\lambda)\, d\lambda}{\int_0^{\infty} E(\lambda)\, d\lambda}.$$

The area under this curve is the solar reflectance for one reflection. $[\rho(\lambda)]^3$ was then plotted, and the area under the curve was measured to obtain the solar reflectance for three reflections (1 - L). The plots are shown in Figure 54. The single reflectances obtained were 92.8 percent for aluminum and 92.0 percent for silver. The triple reflectances are 80.3 percent for aluminum and 86.2 percent for silver.

It can be seen from the plots that the first reflection from a silver surface filters out most of the ultraviolet energy from the solar spectrum. The reflectances at the subsequent reflections are then much higher, and the resulting triple reflectance is quite high. This filtering action has an additional advantage. Since the energy absorbed by the column at the second reflection and by the cone at the third reflection will be decreased, these areas will operate at lower temperatures. The chief disadvantage of silver is its poor durability under certain environments.

The test cone utilized aluminum evaporated onto a polyester film. Measurements with the integrating sphere and the collimator light source indicated a reflectance of about 80 percent. The following factors contributed to reflectance degradation:

(1) The diffuse component of reflectance.

(2) Dimples in the surface caused by dust particles between the mold and the film during fabrication.

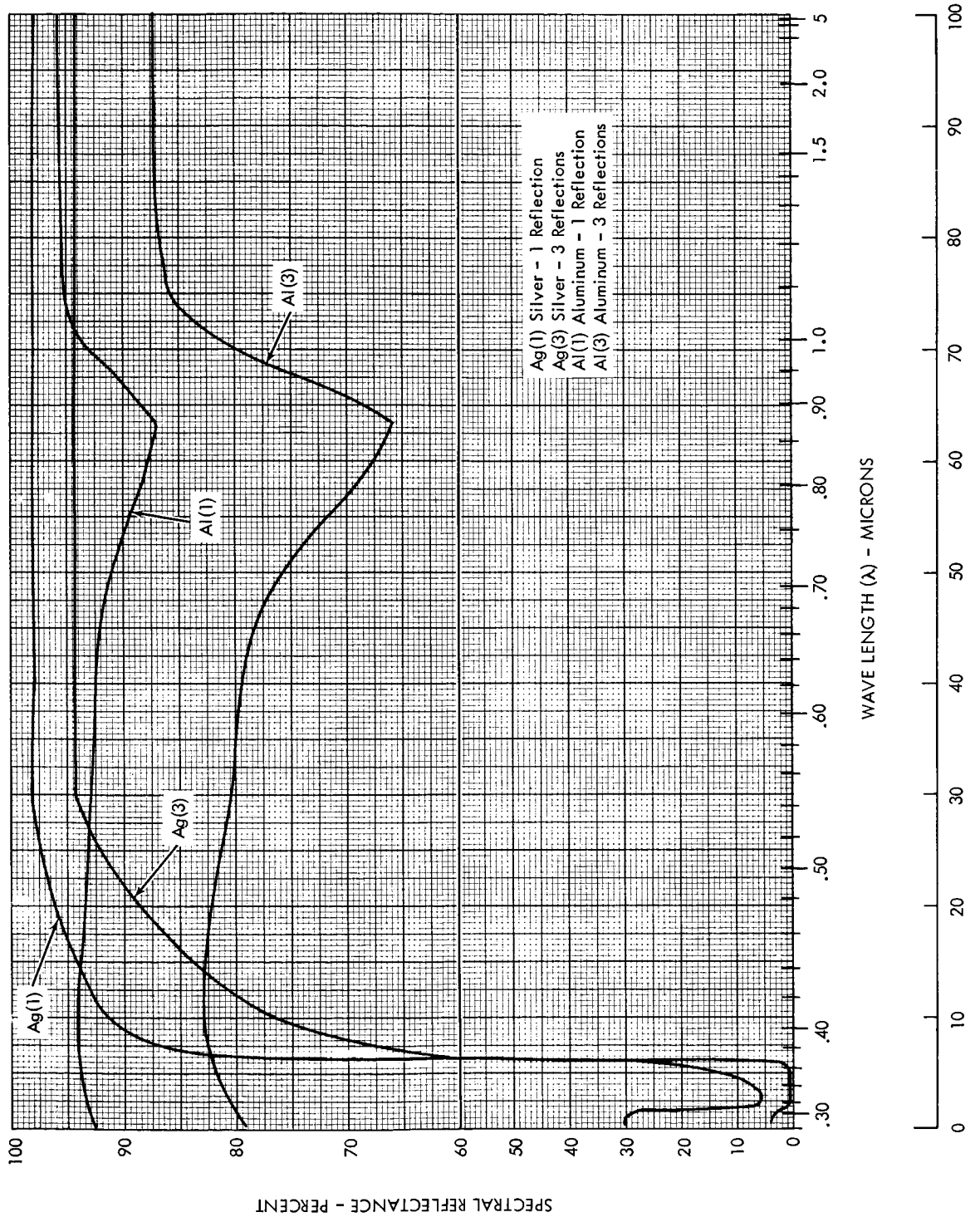

Figure 54. Spectral Reflectances of Silver and Aluminum (Single and Triple Reflectances)

(3) Oxidation of the aluminum as evidenced by a yellow tint of the surface.

The test column utilized aluminum evaporated onto a nickel-plate substrate and a silicon oxide overcoat. Measurements of over-all reflectance and cone reflectance indicate that the column reflectance is about 60 to 70 percent. The following factors contributed to column reflectance loss:

(1) A large diffuse component due to the failure of the plating process to level the deeper machining marks.

(2) Absorption of energy by the silicon oxide coating as evidenced by a cloudy appearance on some areas on the column. Rainbow colors on the column indicated interference effects in the coating, but these are not necessarily deleterious.

In addition to the above reflectance losses, other losses are present due to seams and wrinkles in the cone and due to rounding of the corners of the steps on the column; they probably do not amount to more than one or two percent of the incident energy. These losses do not show up in the data, because these reflecting areas were generally avoided in selecting points for examination.

2. Column Size Effects

The cone-and-column concentrator may be considered to concentrate solar energy in two steps. The cone serves to concentrate the solar energy to an axis, and the column serves to concentrate the energy to a point on the axis, thus achieving a point focus. Since energy leaving the axis after the second reflection will return to the axis after the third reflection regardless of azimuth, it is not essential that the ray leaving the column have the same azimuth it had before striking the column. It follows, then, that it is not essential that the ray strike the column exactly or very near center. This can be seen from the plan view of the ray trace diagram in Figure 25.

As the incident ray moves further off the center of the column, the effectiveness of the parabolic shape in focusing the ray becomes less. It was found in the analysis that there is a critical column radius less than which the concentration of energy falls off sharply and greater than which there is little effect on concentration. The critical column radius is a function of the distance up the column and the tangential angular error of rays approaching the column. In the optical analysis, the column was divided into four uniform radius sections. Proportion of radii was determined, which would require least column area with no significant loss in performance. This proportion is 1 : 1 : 0.725 : 0.415. The required radius of the top column section was found to be

$$p_0 = 0.01\, R_o \sqrt{4.6 + 0.313\, X_{max} + 0.267\, \sigma_{\bar{\theta}_t}}, \qquad (31)$$

where

R_o is the rim radius of the cone,

X_{max} is the orientation accuracy in minutes,

and

$\sigma_{\bar{\theta}_t}$ is the standard deviation tangential component of the cone slope error in minutes.

The square root relationship shows that the column radius does not increase in direct proportion to the errors that must be accommodated. Probably in no design will the radius of the top section exceed five percent of the cone radius.

Since the analysis indicated the independence of image size with respect to column size up to some critical column radius, tests on the optical model should, and did, verify this. Increase in image diameter due to tangential misalignment was found to be very nearly the same as the increase due to radial misalignment. Tangential misalignment causes the beam to strike the column off center; the radial misalignment does not.

3. Orientation Errors

Orientation error may be considered a displacement of the sun from the zenith of the concentrator in the celestial sphere. In the case of a time averaged error such as that used in the analysis, the sun may be considered as having its intensity redistributed over a larger area. This spreading will be the same no matter what type of concentrator is used. The image obtained of this spread sun will then be dependent only on the imaging characteristics of the concentrator used. Since the optics of the cone-and-column concentrator are essentially equivalent to the optics of a paraboloidal concentrator, the effect of misorientation on performance should be the same.

In the analysis it was determined that the effective image radius, d, is related to the concentrator radius, R_O, and the orientation accuracy, X_{max}, by the following relationship:

$$d = 0.01\, R_O \sqrt{0.55 + 0.00394\, X_{max}^2} \qquad (32)$$

where X_{max} is in minutes.

The expression becomes more meaningful if it is written in the following form:

$$d = \frac{R_O}{3440} \sqrt{(1.60 \times 16)^2 + (2.16\, X_{max})^2}\ , \qquad (33)$$

where 16 expresses the radius of the solar disk in minutes and 3440 is the number of minutes in a radian. The coefficient 1.60 accounts for the aberration associated with the concentrator optics. The coefficient of X_{max} would also be the same, except that the distribution function associated with X_{max} is different from the distribution of intensity in the solar disk.

The test of the concentrator with the collimated light source misaligned with the optic axis produced a shift in the power curve proportional to the misalignment

angle. The proportionality factor was the same as would be obtained with a paraboloidal concentrator. Thus, this test helped to verify the similarity to paraboloidal optics.

4. Slope Errors

The effects of slope errors in the reflecting surfaces were investigated in the computer analysis. Tangential and radial components of surface slope errors were investigated separately. The cone and the column surfaces were analyzed separately. The combined effect of errors at the two points of incidence on the cone was determined with the error distributions at the two points equal. It was found that the effective image radius, d, could be expressed as a function of the standard deviation components as follows:

$$d = 0.01\, R_o \sqrt{0.55 + 0.0087\, (\sigma_{\bar{\theta}_t})^2}\,, \tag{34}$$

$$d = 0.01\, R_o \sqrt{0.55 + 0.033\, (\sigma_{\bar{\theta}_r})^2}\,, \tag{35}$$

$$d = 0.01\, R_o \sqrt{0.55 + 0.000209\, (\sigma_{\bar{\alpha}_t})^2}, \tag{36}$$

and

$$d = 0.01\, R_o \sqrt{0.55 + 0.0178\, (\sigma_{\bar{\alpha}_r})^2}\,, \tag{37}$$

where

R_o is the cone radius,

σ is the standard deviation of the slope error distribution in minutes,

and

the subscripts $\bar{\theta}$, $\bar{\alpha}$, t, and r refer to the cone, the column, the tangential

component, and the radial component. Putting the equations in the form of Equation 33, we obtain the following:

$$d = \frac{R_o}{3440} \sqrt{(1.60 \times 16)^2 + (3.21\, \sigma_{\bar{\theta}_t})^2}\ , \tag{38}$$

$$d = \frac{R_o}{3440} \sqrt{(1.60 \times 16)^2 + (6.26\, \sigma_{\bar{\theta}_r})^2}\ , \tag{39}$$

$$d = \frac{R_o}{3440} \sqrt{(1.60 \times 16)^2 + (0.50\, \sigma_{\bar{\alpha}_t})^2}\ , \tag{40}$$

$$d = \frac{R_o}{3440} \sqrt{(1.60 \times 16)^2 + (4.57\, \sigma_{\bar{\alpha}_r})^2}\ . \tag{41}$$

The relative effects of the various errors may be seen at once by inspection of the above equations.

The dependence on $\sigma_{\bar{\alpha}_t}$ should be negligible as implied in the discussion on column sizing. The reason for the small dependence shown here is that relatively large columns were used in the determination of these equations, and this tends to increase the coefficient of $\sigma_{\bar{\alpha}_t}$. More accurate results will be obtained by assuming no dependence on $\sigma_{\bar{\alpha}_t}$ as long as it is less than one or two degrees.

In the test concentrator, the errors could not be separated, so there was no means of verifying these equations.

5. Summation of Losses

In the concentration system, each angular deviation that contributes to the distribution of energy about the focus is itself distributional in nature. The distributional variations are the variation of intensity in the solar disk, the orientation error, the components of slope error in the reflecting surfaces, and the optical aberration associated with the concentrator geometry.

In superimposing one distribution on another, a third distribution is obtained. If the two distributions are one-dimensional Gaussian distributions with standard deviations σ_1 and σ_2, the resulting distribution will be Gaussian with a standard distribution $\sigma_3 = \sqrt{\sigma_1^2 + \sigma_2^2}$. The form of this equation is the basis for the form of Equations 32 through 41. While the various distributions are not necessarily Gaussian, the computer analysis showed that they are apparently sufficiently close to obey the rule of Gaussian superimposition. Further, neither are the distributions one-dimensional, but the analysis showed that the image radius is governed by the wider distribution. The power contained in this image will be only slightly affected by the narrower distribution.

The radius of the image based on the "radial distributions" is determined by superimposing the distribution factors for radial errors. The radius based on "tangential distributions" is determined similarly from the distribution factors for tangential errors. The larger of these two radii is then the image radius. Using Equations 33, 35, and 37, the radius for radial errors is

$$d_r = \frac{R_o}{3440} \sqrt{(1.60 \times 16)^2 + (2.16\, X_{max})^2 + (6.26 \sigma_{\bar{\theta}_r})^2 + (4.57\, \sigma_{\bar{\alpha}_r})^2} \quad . \quad (42)$$

Using Equations 33 and 38, the radius for tangential errors is

$$d_t = \frac{R_o}{3440} \sqrt{(1.60 \times 16)^2 + (2.16\, X_{max})^2 + (3.21 \sigma_{\bar{\theta}_t})^2} \quad . \quad (43)$$

The effective image radius, d, is then the greater of d_r and d_t. The normalized effective image area used in Equation 28 is $A_0/A_c = d^2/R_o^2$. Again, this is the reciprocal of the effective area concentration ratio.

These relationships were verified in part by computing the focal plane distributions for three degrees of accuracy. To obtain these degrees of accuracy, the orientation accuracies were chosen to be 6, 15, and 30 minutes and the standard

deviations of slope error for the cone and the column were chosen to be 6, 15, and 30 minutes and 6, 12, and 18 minutes respectively. The plots of power versus area are shown in Figure 51. The calculated values of A_0/A_c based on d_t as given by Equation 43 are 0.101×10^{-3}, 0.340×10^{-3}, and 1.211×10^{-3}. Based on Equation 42 for d_r, A_0/A_c was determined to be 0.249×10^{-3}, 1.287×10^{-3}, and 4.982×10^{-3}. In each case, $d_r > d_t$ and the latter values of A_0/A_c show good agreement with the effective normalized aperture area as determined from the curves.

C. GEOMETRY

The basic geometry of the cone-and-column concentrator may be defined by the three parameters: the apex half-angle of the cone, θ; the effective rim angle, β; and the rim radius of the cone, R_0. Another factor having a small influence on the geometry is the radius of the top of the column, p_0. Dependent geometric parameters are the angle between the column surface at the top and the concentrator axis, α_0, and the following distances from the cone apex: to the top of the column, H; to the focal point, S; and to the plane containing the rim of the cone, U. The dependence is given by the following equations:

$$\alpha_0 = \frac{\beta}{2} + 2\theta - 90^o, \tag{44}$$

$$H = R_0 \sin 2\theta, \tag{45}$$

$$S = R_0 (\cot \beta + \cot 2\theta), \tag{46}$$

and

$$U = R_0 \cot \theta. \tag{47}$$

In selecting a geometry, the following factors must be considered:

(1) β must be selected to give an image size that is near minimum, generally $40^o < \beta < 65^o$.

(2) θ must be large enough so that no large reflectance losses result from the high angle of incidence at the first reflection.

(3) α_0 must not be negative by more than approximately four degrees if flaring of the top of the column or ray blockage by steps on the column is to be avoided.

(4) S should be sufficiently greater than H to avoid interference of the top of the column with rays coming from the bottom of the cone.

(5) S should not be so much greater than H or U that structural problems arise in the support of the heat receiver or the rim of the cone.

For all the computer calculations, a basic geometry was used, which is characterized by the parameters β = 45 degrees and θ = 33.75 degrees. Investigation shows that only slight changes from these values are allowed by the limitations listed above.

Computer analyses were made for the concentrator with intermediate accuracy varying θ to 31.75° and 35.75° and varying β to 41° and 49°. The performance curves are shown in Figures 52 and 53. Inspection of these curves in the vicinity of the 95 percent power point shows no significant improvement due to the changes and a slight loss when the rim angle was decreased and when the cone angle was increased.

It may be concluded that the basic geometry chosen is near optimum from both a performance standpoint and a structural standpoint.

SECTION VIII. CONCLUSIONS

The experimental and computational investigations made on the cone-and-column concentrator show that the cone-and-column concentrator performs essentially the same as a paraboloidal concentrator. The chief differences are due to the two additional reflections required in the cone-and-column concentrator. The investigation also clarified some of the basic relationships between errors, losses, and performance of concentrators in general.

In the evaluation of concentrators in general, it was found that reflection losses should be subtracted from the ideal receiver efficiency to obtain over-all concentrator receiver efficiency. This produces a lower result than taking the product of reflectance and receiver efficiency and attaches greater significance to concentrator reflectance.

With the cone-and-column concentrator, the reflectance losses tend to become high because of the three reflections required. It was found that the limiting value of reflectance is somewhat higher than the cube of the single reflectance. Limiting values of triple reflectance calculated were 86.2 percent for aluminum and 80.3 percent for silver.

It was observed in the analysis that the distributional deviations and errors are not additive arithmetically but follow the rules of distributional superimposition, i.e., $\sigma_{total} = \sqrt{\sigma_1^2 + \sigma_2^2 + \sigma_3^3 + \ldots}$ Since the cone-and-column optics superimpose up to five distributions (solar, orientation, and three surfaces) to obtain the focal plane flux distribution, the cone-and-column provides much higher concentrations than would be anticipated by simply adding the deviations and errors.

It was determined that the image radius is determined from the larger of the two expressions

$$d_r = \frac{R_o}{3440} \sqrt{(1.60 \times 16)^2 + (2.16\, X_{max})^2 + (6.26\, \sigma_{\bar{\theta}_r})^2 + (4.57\, \sigma_{\bar{\alpha}_r})^2} \quad (48)$$

and

$$d_t = \frac{R_o}{3440} \sqrt{(1.60 \times 16)^2 + (2.16\, X_{max})^2 + (3.21\, \sigma_{\bar{\theta}_t})^2} \,. \quad (49)$$

Area concentration ratio is then $(R_o/d_{max})^2$. Since d_r tends to be greater than d_t, the accuracy requirements on the tangential slope error of the cone can usually be relaxed with no loss of performance, but with a weight penalty associated with an increase in column radius. Examination of these equations also discloses the independence of image radius on tangential slope error of the column, $\sigma_{\bar{\alpha}_t}$.

Figures 51 and 55 show fractional power (or geometric efficiency) plotted against normalized aperture area and its reciprocal, concentration ratio, for three degrees of accuracy. These curves typify the concentrating ability of cone-and-column concentrators.

The analysis showed that there is a critical column diameter less than which the performance falls off sharply and greater than which there is practically no effect on performance. This diameter varies along the length of the column. If four uniform diameter column sections are used, their diameters should be kept in the proportion 1 : 1 : 0.725 : 0.415, starting at the top. The critical radius at the top of the column was found to be expressed by

$$p_0 = 0.01\, R_o \sqrt{4.6 + 0.313\, X_{max} + 0.267 \sigma_{\bar{\theta}_t}} \,, \quad (50)$$

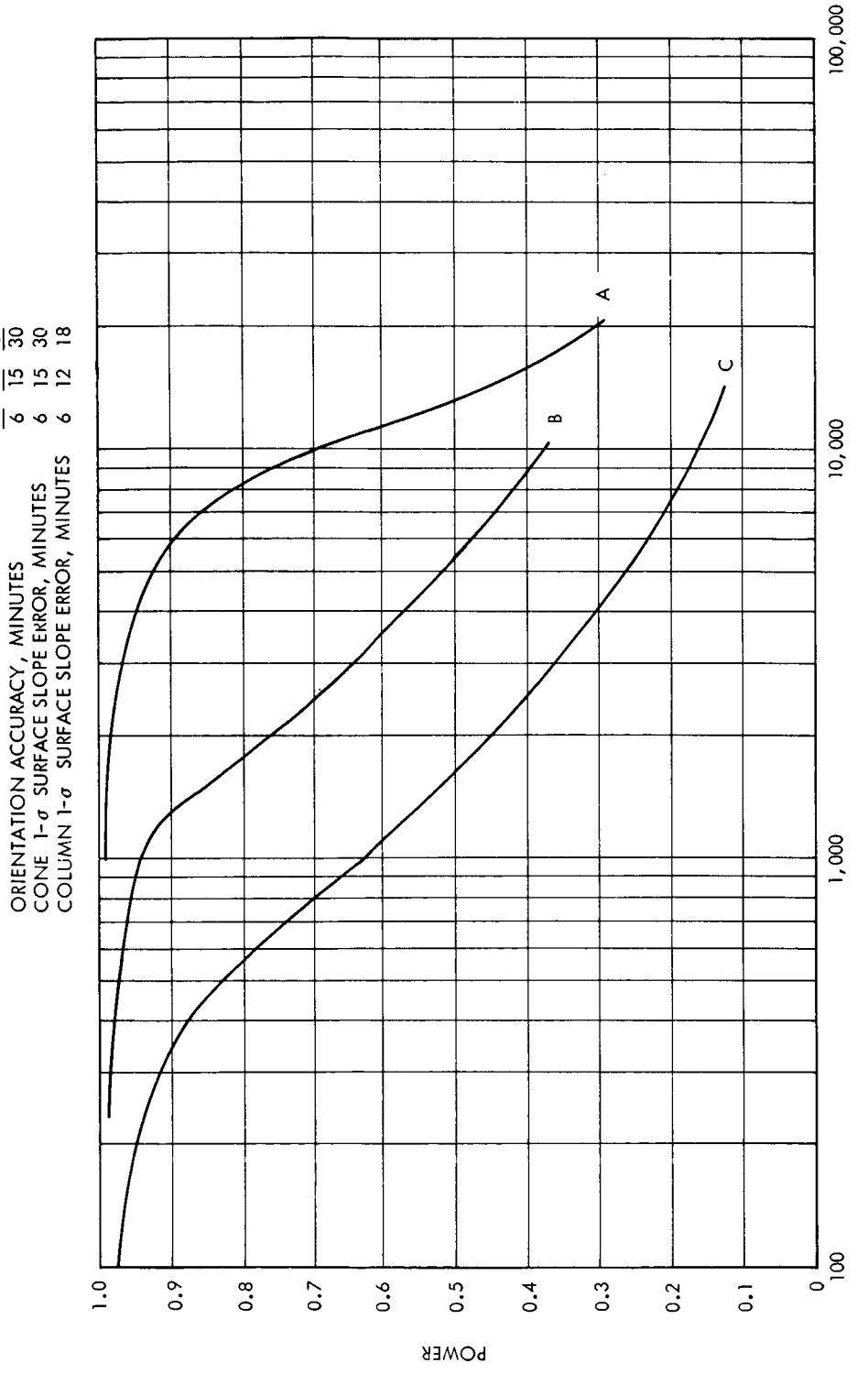

Figure 55. Performance of Various Cone-and-Column Concentrators at Various Concentration Ratios

where R_o is the cone rim radius, X_{max} the orientation accuracy in minutes , and $\sigma_{\bar{\theta}_t}$ the tangential component standard deviation slope error in minutes. The square root relationship tends to keep the critical radius from ever becoming very large. For the three typical concentrators shown in Figures 51 and 55, the values of p_0/R_o used were 0.02842, 0.03645, and 0.04359, starting with the most accurate concentrator.

SECTION IX. RECOMMENDATIONS

The optical analysis contained in this report has been carried as far as possible in a general form. Further analysis will be needed only to meet the requirements of a specific application.

The most significant gap in the analysis is the absence of good information for determining the reflectance loss. To fill this gap, typical materials and fabrication methods should be investigated in order to determine a reasonable value for the reflectance loss.

In order to determine the competitive position of the cone-and-column concentrator, the problems and weights associated with the deployment of this configuration should be investigated. A logical first step would be the construction of a small-scale deployable model.

SECTION X. LIST OF SYMBOLS

NOTE: Angles not identified on illustrations are arbitrarily assigned auxiliary angles.

R	Concentrator radius
R_i	Radius of concentrator at base of cone reflective surface
C_R	Ratio of concentrator radius at cone base to radius of cone rim
S	Distance from apex to focal point
ΔS	Change in S
ℓ	Distance from apex to vertex of parabola which determines shape of column
Γ_S	Declination of sun from concentrator axis
Γ_0	Azimuth of sun with respect to the reference orientation axis
Γ_A	Azimuth of sun with respect to concentrator radius through point of incidence
Γ_1	Aximuth of R_I with respect to the reference orientation axis; selected at random between 0 and 360^o
F	Angle, on solar disk, between concentrator azimuth and origin of ray being traced; selected at random between 0 and 360^o
H	Angle between line-of-sight to sun and ray being traced
X_c	A constant representing a fixed orientation error
θ	Apex half angle of cone
$\bar{\theta}$	Surface slope error of cone at point of first reflection

$\bar{\bar{\theta}}$	Surface slope error of cone at point of third reflection
α	Angle between tangent to a perfect column and concentrator axis
$\bar{\alpha}$	Surface slope error of column at point of second reflection
β	Angle between focused ray and concentrator axis
j	Number of sections comprising the column
p	Column radius
ρ	Ray length
d	Distance, in focal plane, of ray from focal point
τ	Angle of incidence and reflection at first point of reflection
$\sigma_{\bar{\theta}_r}$	Standard deviation of radial slope error at the first point of reflection
$\sigma_{\bar{\theta}_t}$	Standard deviation of tangential slope error at the first point of reflection
$\sigma_{\bar{\alpha}_r}$	Standard deviation of radial slope error at second point of reflection
$\sigma_{\bar{\alpha}_t}$	Standard deviation of tangential slope error at second point of reflection
$\sigma_{\bar{\bar{\theta}}_r}$	Standard deviation of radial slope error at third point of reflection
$\sigma_{\bar{\bar{\theta}}_t}$	Standard deviation of tangential slope error at third point of reflection
χ	Angle of incidence and reflection at second point of reflection
V	Angle of incidence and reflection at third point of reflection
K_s	A number selected at random between 0 and +1
C_x	A number selected at random between -1 and +1

v_1, v_2, v_3 An angle selected at random between 0 and 360°

P_1, P_2, P_3 A number selected at random between 0 and +1

$(R_I)^2$ A number selected at random between $(R_i)^2$ and $(R_o)^2$

$X_{\bar{\theta}}$ The abscissa of the normal curve (as given by Reference 1) for $\bar{\theta}$ corresponding to a cumulative probability of P_1

$X_{\bar{\alpha}}$ The abscissa of the normal curve (as given by Reference 1) for $\bar{\alpha}$ corresponding to a cumulative probability of P_2

$X_{\bar{\bar{\theta}}}$ The abscissa of the normal curve (as given by Reference 1) for $\bar{\bar{\theta}}$ corresponding to a cumulative probability of P_3

Subscripts

o Associated with the outside or rim ray

r In or associated with a radial plane (a plane containing the concentrator axis)

t In or associated with a tangential plane (a plane perpendicular to a radial plane)

1, I At or associated with point of first reflection

2, II At or associated with point of second reflection

3, III At or associated with point of third reflection

4 At or associated with intersection of ray and focal plane

h Horizontal projection

SECTION XI. REFERENCES

1. Hastings, Cecil, Jr., Approximations for Digital Computers.

2. Holland, L., "The Effect of Vapor Incidence on the Structure of Evaporated Aluminum Films," Journal of Optical Society of America, Vol 43, May 1953, pp. 376 - 380.

3. Hass, G., "Filmed Surfaces for Reflecting Optics," Journal of Optical Society of America, Vol 45, No. 11, 1955.

4. Bradford, A.P., and Hass, G., "Increasing the Far-Ultraviolet Reflectance of Silicon Oxide Protected Aluminum Mirrors by Ultraviolet Irradiation," Journal of Optical Society of America, Vol 53, No. 9, September 1963.

5. Surface Effects on Spacecraft Materials, First Symposium, J. Wiley & Sons, 1960, Edited by Francis J. Clauss.

6. Edwards, D.K., et al, Basic Studies on the Use and Control of Solar Energy, No. 60-93, University of California, L.A., October 1960.

7. Handbook of Geophysics, U.S. Air Force, Mac Millan Co, New York, 1960, tables 16-8 and 16-9, pp 16-16 and 16-17.

8. The Sun, Edited by Gerald P. Kuiper, The University of Chicago Press.